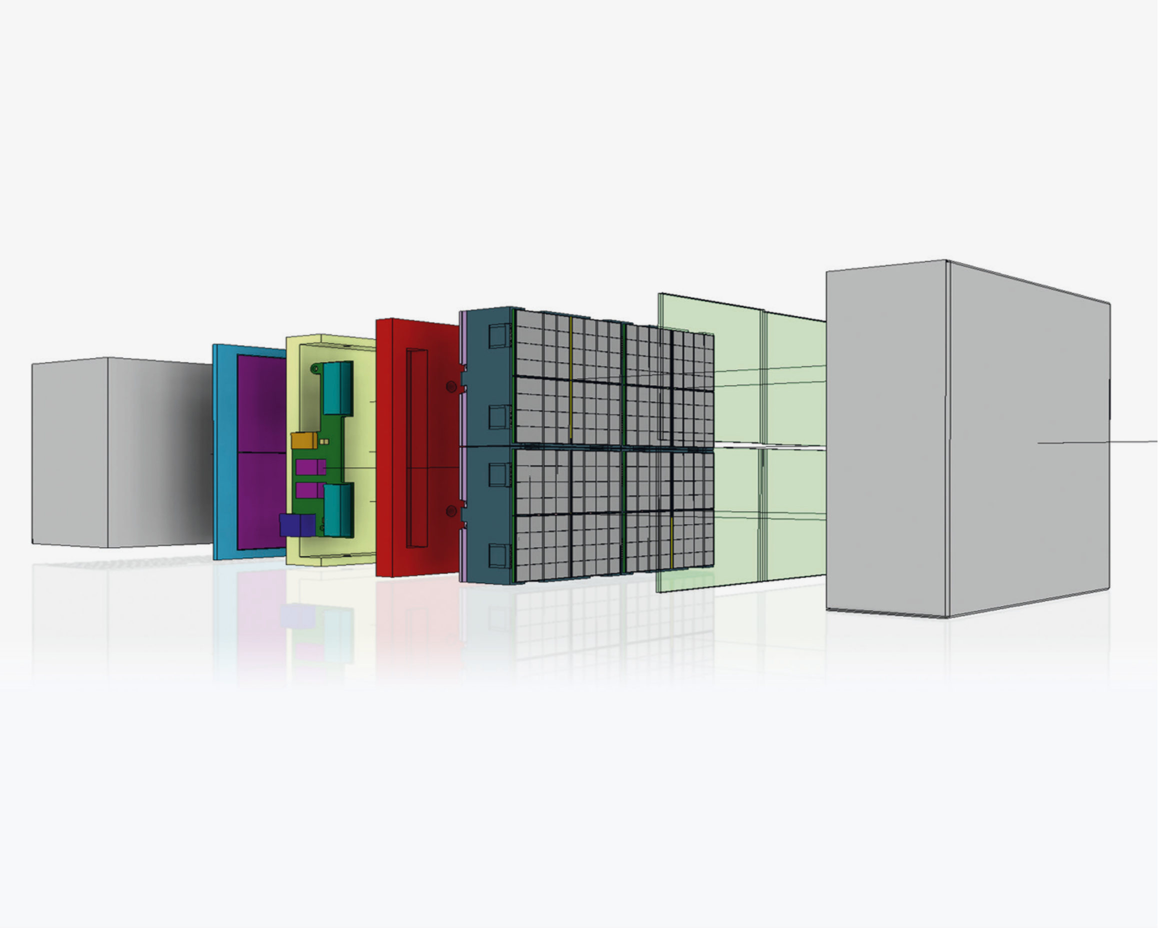

Application of Silicon Photomultipliers in Neutron Detectors

Shashank Kumar

Schlüsseltechnologien / Key Technologies
Band / Volume 233
ISBN 978-3-95806-537-6

Mitglied der Helmholtz-Gemeinschaft

JÜLICH
Forschungszentrum

Schriften des Forschungszentrums Jülich
Reihe Schlüsseltechnologien / Key Technologies Band / Volume 233

Forschungszentrum Jülich GmbH
Zentralinstitut für Engineering, Elektronik und Analytik (ZEA)
Systeme der Elektronik (ZEA-2)

Application of Silicon Photomultipliers in Neutron Detectors

Shashank Kumar

Schriften des Forschungszentrums Jülich
Reihe Schlüsseltechnologien / Key Technologies Band / Volume 233

ISSN 1866-1807 ISBN 978-3-95806-537-6

Bibliografische Information der Deutschen Nationalbibliothek.
Die Deutsche Nationalbibliothek verzeichnet diese Publikation in der
Deutschen Nationalbibliografie; detaillierte Bibliografische Daten
sind im Internet über http://dnb.d-nb.de abrufbar.

Herausgeber und Vertrieb:	Forschungszentrum Jülich GmbH Zentralbibliothek, Verlag 52425 Jülich Tel.: +49 2461 61-5368 Fax: +49 2461 61-6103 zb-publikation@fz-juelich.de www.fz-juelich.de/zb
Umschlaggestaltung:	Grafische Medien, Forschungszentrum Jülich GmbH
Druck:	Grafische Medien, Forschungszentrum Jülich GmbH
Copyright:	Forschungszentrum Jülich 2021

Schriften des Forschungszentrums Jülich
Reihe Schlüsseltechnologien / Key Technologies, Band / Volume 233

D 464 (Diss. Duisburg, Univ., 2021)

ISSN 1866-1807
ISBN 978-3-95806-537-6

Vollständig frei verfügbar über das Publikationsportal des Forschungszentrums Jülich (JuSER)
unter www.fz-juelich.de/zb/openaccess.

"Take risks in your life if you win, you can lead. If you lose, you can guide!"
- Swami Vivekananda

"Live as if you were to die tomorrow. Learn as if you were to live forever"
- Mahatma Gandhi

Contents

Acknowledgement

This thesis was written as part of the development activities at the *Central Institue of Engineering, Electronics and Analytics- Electronic Systems (ZEA-2)* at *Forschungszentrum Jülich GmbH*, Germany. I am immensely grateful to my supervisor Prof. Dr.-Ing. Stefan van Waasen, for not only providing me the opportunity to carry out this research, but also for his guidance, support and advice over the past four years.

I would like to profoundly acknowledge valuable contribution of Prof. Dr.-Ing. Daniel Durini Romero in the early stage of this work and am thankful for not only his readiness for being the co-supervisor of this thesis, but also for continuous encouragement and invaluable discussions.

My gratitude goes to Dr. Matthias Herzkamp, for his assistance with the simulations and who stuck with me through thick and thin. I would like to thank him for helping me to become familiar with algorithms as well as always finding time for me to make this research interesting and fun. Moreover, I deeply appreciate Dr. Carsten Degenhardt for the contributions and close collaboration with this thesis as the team leader.

A big shout out goes to all the PhD students at the ZEA-2 and specially to the PhD trips that we had together for creating a friendly and enjoyable working environment. I would also like to thank all the fellow colleagues of ZEA-2 for their support at various stages of this thesis and help with the experiments performed.

Many thanks to the administration of ZEA-2, including Mrs. Britta Hallmann who was instrumental in taking care of all the paper work and making my stay at ZEA-2 smooth.

I want to thank my parents, family and friends for their never ending love, good wishes and support. I would like to express my great appreciation to all the individuals who contributed to the completion of this thesis, no matter how small.

Last but not least, special thanks goes to my better half Shalini and little angel Saavi for their unconditional love, encouragement and patience during this endeavour. I am forever indebted to their understanding and support throughout the years in all situations, no matter good or bad. This work is dedicated to them.

Abstract

Advancement in the development of semiconductor photodetectors have led to substitution of Photomultiplier Tube (PMT) technology by solid state devices in many applications. Silicon Photomultipliers (SiPM) are solid-state photodetectors with a gain similar to PMT and that have several advantages over the PMTs like low operating voltages and insensitivity to magnetic fields. However, concerns of radiation damage induced in Silicon due to neutron radiation required a deeper understanding in order the SiPMs to become a suitable technology for neutron detector systems.

This work provides an insight into effects of cold neutron irradiation on the important macroscopic characteristics (dark count rate (DCR), photon detection efficiency (PDE) and timing resolution (TR)) of SiPMs and its quantification for two analog samples manufactured respectively by *SensL - ON Semiconductor* and *Hamamatsu Photonics*, and one digital SiPM (Philips Digital Photon Counting, PDPC) from *Koninklijke Philips N. V.* Further, it describes the development of a large cold/thermal neutron scintillation detector prototype, with an active area of 13.6 cm $\times$ 13.6 cm, utilizing the digital SiPM (PDPC) modules and a ^{6}Li glass scintillator. The goal of the development is to have a neutron (5 Å) detection efficiency of $> 75\,\%$, a possible count rate of $> 2\,\mathrm{kcps/cm^2}$, and a spatial resolution of minimum 1 mm $\times$ 1 mm.

In order to achieve the targeted spatial resolution a light guide was introduced between the SiPM array and the scintillator glass. Geant4 simulations were performed in advance for optimization of the setup. The simulation results were verified by comparing simulation data with measurement results obtained at the research reactor BER-II of HZB Berlin and FRM-II of TU Munich in Garching. Additionally, the overall performance of the detector prototype is evaluated, which finds the prototype to exceed (neutron detection efficiency $> 95\,\%$, $100\,\mathrm{kcps/cm^2}$ count rate and 1 mm $\times$ 1 mm spatial resolution) the specified goals.

Furthermore, customized position reconstruction algorithms were developed, based on

comparison of simulation and measurement data, and implemented for the targeted neutron detection resolution with a precision of 1 mm. Subsequently, the efficacy of the algorithms were compared for the given detector prototype.

Kurzfassung

Fortschritte in der Entwicklung von Halbleiter-Fotodetektoren haben zur Substitution von Photomultipleierröhren (PMT) durch Siliziumphotonenvervielfachern (SiPM) in vielen Anwendungsfeldern geführt. SiPMs sind halbleiterbasierte Fotodetektoren mit einer ähnlichen Verstärkung wie PMTs und weisen neben dem Vorteil der Halbleitertechnologie auch Eigenschaften wie eine niedrige Betriebsspannung und Unempfindlichkeit gegenüber Magnetfeldern auf. Allerdings müssen Bedenken hinsichtlich Strahlungsschäden, die durch Neutronen in Silizium induziert werden, auf die Anwendbarkeit in Neutronendetektoren untersucht werden.

Diese Arbeit bietet einen Einblick in die Auswirkungen der Bestrahlung mit kalten Neutronen auf die wichtigen makroskopischen Kennzahlen (Dunkelzählrate (DCR), Photonendetektionseffizienz (PDE) und Zeitauflösung (TR)) von SiPMs und deren Quantifizierung für zwei analoge Sensoren, die von *SensL - ON Semiconductor* und *Hamamatsu Photonics* hergestellt wurden, und einen digitalen Sensor (Philips Digital Photon Counting, PDPC) from *Koninklijke Philips N.V.* Außerdem wird die Entwicklung eines großen Detektor-Prototypen für thermische Neutronendetektion mit einer aktiven Fläche von 13.6 cm × 13.6 cm beschrieben, bei dem der digitale SiPM (PDPC) und ein ^{6}Li-Glasszintillator eingesetzt werden. Das Ziel des Detektors war es, eine Neutronendetektionseffizienz (5 Å) von $> 75\,\%$, eine Zählrate von $> 2\,\mathrm{kcps/cm^2}$ und eine Ortsauflösung von mindestens 1 mm × 1 mm zu erreichen.

Um das Ziel der räumlichen Auflösung zu erreichen, wurde ein Lichtleiter zwischen dem SiPM-Array und dem Szintillatorglas eingesetzt. Um den Aufbau zu optimieren, wurden Geant4-Simulationen im Vorhinein verwendet. Später wurden die Simulationsergebnisse durch den Vergleich von Simulationsdaten mit Messergebnissen, die hauptsächlich aus dem Forschungsreaktor BER-II des HZB Berlin und FRM-II der TU München, Garching stammen, verifiziert. Zusätzlich wurde die Gesamtleistung des Detektorprototypen bewertet, wobei festgestellt wurde, dass der Prototyp die spezifizierten Ziele übertrifft (Neutronendetektion-

seffizienz von $> 95\,\%$, $100\,\mathrm{kcps/cm^2}$ Zählrate und $1\,\mathrm{mm} \times 1\,\mathrm{mm}$ Ortsauflösung).

Darüber hinaus wurden auf der Grundlage der Simulations- und Messdaten angepasste Algorithmen zur Positionsrekonstruktion entwickelt und für die angestrebte Auflösung der Neutronendetektion mit einer Genauigkeit von $1\,\mathrm{mm}$ implementiert. Anschließend wurde die Leistungsfähigkeit der Algorithmen für den gegebenen Detektor-Prototypen verglichen.

List of Figures

List of Tables

Acronyms

PMT Photomultiplier Tube

SiPM Silicon Photomultipliers

DCR dark count rate

PDE photon detection efficiency

TR timing resolution

TOF time-of-flight

SANS small angle neutron scattering

APD avalanche photodiode

PD photodiode

CIS CMOS image sensors

SPAD single photon avalanche diode

PDPC Philips digital SiPM

GMAPD Geiger mode avalanche photodiode

GAPD Geiger avalanche photodiode

EHP electron hole pair

SCR space charge region

CMOS complementary metal oxide semiconductor

NIR near infrared

FDSOI fully depleted Silicon on insulator

BSI	back side illumination
FSI	front side illumination
PET	positron emission tomography
TDC	time-to-digital converter
FSM	finite state machine
FOM	figures of merit
GR	generation recombination
NIEL	non ionization energy loss
IEL	ionization energy loss
DLTS	deep-level transient spectroscopy
TSC	thermally stimulated current
RI	refractive index
COG	center of gravity
LRF	light response function
LUT	look up table

Chapter 1

Introduction

The most prominent scientific use of neutrons is fundamental research associated with the scattering experiments performed at research reactors. The scattering experiments such as time-of-flight (TOF) spectrometry, reflectometry and small angle neutron scattering (SANS) utilize cold/thermal neutrons to investigate the structure and dynamics of matter down to atomic scales (sub nm) [1]. These methods of characterization for thermodynamics and morphology have wide range of applications and over the years emerged as well established techniques for material research [1]. The study involves the detection of neutrons that are scattered from samples under investigation. The efficient and precise detection of neutrons is crucial for the further data analysis to understand the sample characteristics. Therefore, the detector plays an important and crucial role in these experiments.

The technology has evolved gradually since the first detection of neutrons using ^{10}B-lined proportional counters in the 1940s. For the detection generally ^{3}He, ^{6}Li, ^{10}B, ^{157}Gd, or ^{235}U isotopes are used. Among these isotopes, since its applicability in the 1980s, ^{3}He became the gold standard, mainly due to its very high cross sectional area for neutron interaction and non-toxic nature. However, its price increase due to limited availability since 2001, and even more so since 2009 triggered the search for suitable alternatives [2].

1.1 Motivation and Objective

One viable alternative is using ^{6}Li [3]. ^{6}Li scintillator glasses were employed for neutron detection since the 1950s [4] in combination with traditional photodetectors, i.e. PMT [5,6]. The available two-dimensional position sensitive detectors for SANS, employing PMTs, have constraints when exposed to high magnetic field environments, and also in what their performance is concerned, yielding either high count rates or high spatial resolutions, but not both simultaneously. For e.g. the TAIKAN detector at J-PARC, Japan [7] has a spatial resolution of 0.5 mm with a maximum count rate of 0.046 Mcps (counts per second) (0.92 Mcps/m^2), whereas the KWS-1 installed at MLZ, Germany [8] yields 5.3 mm and 0.6 Mcps (1.30 Mcps/m^2) respectively.

With the aim to develop a neutron detector that can provide a spatial resolution of < 1 mm at count rates of above 1 Mcps/m^2, one could use solid-state photodetectors, namely SiPM instead of PMTs. The main advantages of SiPMs over PMTs are their lower operating voltage, lower cost, higher form factor, and their full operability in magnetic fields. But the question arises whether SiPMs are suitable for application in neutron detectors, mainly due to radiation damage induced in SiPM caused by neutron interaction. For addressing this topic a detector prototype is developed and measured performance-wise using digital SiPMs.

The main concern with this idea is radiation hardness, i.e. the extent of damage caused by neutrons in Silicon. In order to address this, a recent study was performed for SiPMs under cold neutron irradiation and it was concluded that this technology can be used in a typical SANS environment for a ten year span, or even beyond, where the increase in their dark current due to neutron damage throughout this time remains acceptable and does not eliminate the possibility of doing measurements over this time [9]. Subsequently, for the same irradiated samples of SiPM a decrease in photon detection efficiency (PDE) is observed [10]. For the assessment of TOF applications of SiPM based neutron detector, this work analyses the impact of neutron irradtiation on the timing resolution (TR) of SiPMs. Based on the investigation for degradation in PDE performance [10] for two analog SiPMs and a digital SiPM, the latter was chosen for the detector development, mainly because of the ease of integration and better results compared to analog SiPMs. This means that no separate readout electronics is needed for the digital SiPM, as compared to analog ones.

The target spatial resolution of the detector prototype is 1 mm $\times$ 1 mm. In order to achieve this goal with the digital SiPM (4 mm pixel pitch) array used in this development, a reconstruction algorithm needs to calculate the neutron position from raw data. Existing algorithms, like the center of gravity (COG) approach (a method introduced by *H. O. Anger* [11]), depend on many pixel counts, usually at least 7 [6, 12], in order to give accurate results. In our case, each neutron event consists of four pixel counts only, which is not sufficient for usual reconstruction algorithms. Therefore, the need to develop reconstruction algorithms only using the four pixels arises for the said two dimensional position sensitive detector prototype. One additional task of this work was also to compare algorithms with respect to accuracy and response-time besides detector system integration and its complete characterization.

1.2 Outline of the Study

Chapter 2 introduces a brief overview of neutron detection with the fundamentals of scintillation detectors along with associated photodetectors: PMT and SiPM. As a promising alternative to the PMTs in scintillation neutron detectors, Chapter 3 is focused on SiPM, its characteristics, advancement and digital SiPM used for this work. Subsequently, in order to probe the applicability of SiPMs for neutron detectors, previous and present investigations on radiation damage are discussed in detail, with the emphasis on TR, in Chapter 4. It also gives a brief understanding of the radiation damage mechanism in Silicon.

Chapter 5 deals with the detector prototype, its development, and simulations performed to achieve the optimal design as well as its experimental validation. It also explores the spatially varying non-linearity in SiPM pixels caused by the saturation of microcells due to inhomogeneous distribution of light impinging the detector. In Chapter 6, the formulation of the position reconstruction algorithms and a comparison between them is presented, in addition to measurement of the detector performance. Finally, the summary of the work is given in Chapter 7, which also gives an outlook that might open a continuing line of investigations based on current evaluations and findings.

Chapter 2

Neutron Detection

Neutrons are one of the basic building blocks of matter that together with protons form the atomic nuclei. As a product of spontaneous decay, free neutron are also found in nature, the use of which proved very useful in many fields of Physics, since their discovery in 1932 by James Chadwick [13]. Neutron detection is required in many fields of physics and technology. One of the most important applications are neutron scattering experiments, that are used for material research science, with numerous applications ranging from energy, pharmaceuticals to nano technology and material engineering [14] [15].

2.1 Neutron Interaction

Neutrons have a mass of 1.0097 a.m.u (atomic mass unit) or $1.6749 \times 10^{-27}\,\mathrm{kg}$, a spin of $\frac{1}{2}$, a magnetic moment of $-9.6623 \times 10^{-27}\,\mathrm{J\,T^{-1}}$ (nuclear magneton) and zero charge [1]. Due to their chargeless nature, their interaction with matter is unique. Electrically neutral, neutron do not interact with electron clouds in atoms, but directly with the atomic nuclei, much smaller than the atoms. The latter makes the interpretation of the scattering events between neutrons and the atomic nuclei somewhat more straight forward, as no electrons are involved. The ability to measure energy and momentum exchange makes them, and the experiments involving neutron scattering from atomic nuclei an attractive method for material characterization. Additionally, possessing magnetic moment also makes it suitable to study the magnetic structure of solids in solid state physics. Also due to lower energy (few meV) associated with cold or thermal neutrons, in case of inelastic interactions, they do not change the properties of the sample under investigation.

Table 2.1: Classification of neutrons [1].

Category	Energy [meV]	Temperature [K]	λ [Å]
Ultra-cold	< 0.1	< 1	< 30
Cold	0.1-10	1-120	3-30
Thermal	10-100	120-1000	1-3
Hot	100-500	1000-6000	0.4-1
Epithermal	> 500	> 6000	< 0.4

Neutrons are broadly classified on the basis of energy associated with them. Fast neutrons have energies above 0.5 eV, whereas energies below this value are categorized as slow neutrons [16]. The Table 2.1 depicts the class of neutrons and their energies.

Neutrons are commonly detected by a neutron capture process, which converts them into a measurable electrical signal. Converters get ionized via nuclear reaction after interacting with neutrons and produce secondary particles. These charged particles act as the reference to trace the neutrons. Some of the converters used for detection of slow neutrons are listed in Table 2.2.

Despite having the highest cross section for the reaction, Gadolinium is rarely used because of gamma rays that are produced as the reaction product, which cannot be distinguished from a gamma-ray background. In contrast, ^{3}He provides a very good gamma discrimination characteristic along with high cross section, making it an attractive converter for neutrons. Boron based gas detector are the oldest and most commonly used converters due to higher disintegration energy (Q value) given to the reaction products if compared to ^{3}He, but they have lower interaction probability with neutrons and are highly toxic. ^{235}U is mainly used in fission chambers to count the neutron flux in reactors due to high amount of energy (Q value) liberated in the reaction, which provides extremely low background and in turn allows counting neutron caused reactions at very low rates and no loss in counting sensitivity. However, it suffers from lower neutron counting efficiency and high radioactivity.

Neutron detectors can be broadly classified into gas proportional counters, semiconductor detectors and scintillation detectors. The last option is the one chosen for the present study.

Table 2.2: Commonly used isotopes for thermal neutron detection [16].

Isotopes	He-3	B-10	Li-6	Gd-157	U-235
Reaction products	^{3}H, ^{1}H	^{7}Li , α	^{3}H, α	e, γ	Ba, Kr, n, γ
Abundance in %	0.00014	19.9	7.5	15.7	0.7
Q$^{\#}$ Value in MeV	0.764	2.3	4.78	7.9	150
Cross section @ 25 meV in barn$^{\clubsuit}$	5333	3836	940	255000	586
Form	He	B, BF_3	Li, LiF, LiI	Gd	U
Toxic	No	Yes	No	Yes	Yes
State	Gas	Gas, Solid	Solid	Solid	Solid

($^{\#}$the energy released or absorbed in a nuclear reaction. $^{\clubsuit}$barn $= 1 \times 10^{-28}\,\mathrm{m}^2$)

2.2 Scintillation Detector

This type of detector relies on the production of light in the material upon passage of a particle. In the scintillation process, the interaction of ionizing radiation produces energy that is absorbed and re-emitted as UV and/or visible light that can be easily detected with a photodetector.

Using Lithium is advantageous due to higher disintegration energy (Q value: 4.8 MeV compared to 2.3 MeV for B) released in the process. This generates a larger amount of visible light within the scintillation material, resulting in a greater probability of neutron detection. However, the cross section of Li is only a quarter of that of B, so with a given thickness and enrichment of scintillator, less neutrons are absorbed.

We employed a fast inorganic scintillator GS20® from *Scintacor* [17]. It is a Ce^{3+} activated ^{6}Li glass. Upon neutron capture in the glass, heavy charged particles are produced as per reaction (2.2.1). The range of these particles in the scintillator is in the order of a few tens of micrometers, so all the energy is absorbed within the scintillator unless the event happened at the border. The particles´ absorption lengths within the Li scintillator glass are 5 µm to 10 µm and 40 µm to 150 µm for alpha and triton, respectively [18]. This means that the position of the impinged neutron can be traced with an uncertainty of ±150 µm by detecting the light with underlying photodetector as depicted in Fig. 2.1.

$$^1\mathrm{n} + {}^6\mathrm{Li} \longrightarrow {}^4\alpha(2.05\,\mathrm{MeV}) + {}^3\mathrm{H}\,(2.73\,\mathrm{MeV}) \tag{2.2.1}$$

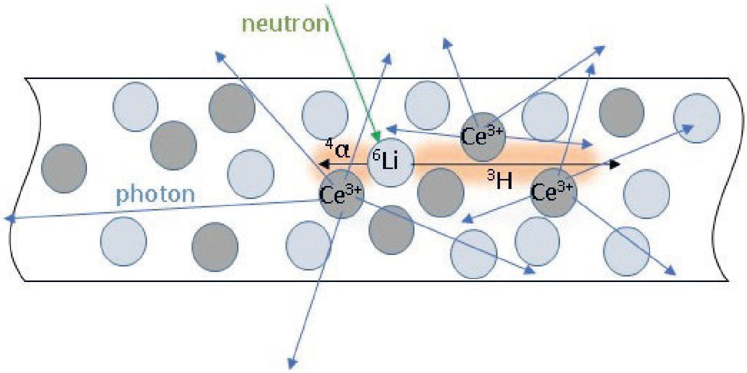

Figure 2.1: Visualization of a neutron capture in the ^{6}Li scintillator glass doped with Cerium, where a neutron reacts with ^{6}Li and produces secondary particles (alpha and triton). The interaction of energy (shown in orange color) from these particles ionizes the Cerium atom, which results in isotropic light emission in the glass.

In order to enhance the probability of visible photon emission, Ce is added as doping material in the Li glass, which act as an activator. It offers fast response due to its dipole 5d - 4f electron transition and posterior de-excitation [16]. Through the transfer of MeV energy associated with the resulting particles, ^{4}He and ^{3}H, the scintillator gets ionized, which results in excitation of Ce^{3+} activator. The excited Ce in the process of de-excitation, isotropically emits light (transparent to the scintillator), in average 6000 photons, with a luminescence decay time between 50 ns to 70 ns per neutron [17].

2.3 Photodetector

There exist numerous light detectors: PMT, P-N photodiode (PD), P-I-N photodiode, avalanche photodiode (APD), Charge Couple Devices (CCD), CMOS image sensors (CIS), single photon avalanche diode (SPAD), or SiPMs, to name just a few. However, none of them is an ideal detector. Therefore, an optimal detector has to be chosen as per application.

It would be impossible to detect the neutrons without the availability of a photodetector that can convert the extremely weak light and almost instantaneous output of a scintillation pulse into a usable electrical signal. Usually PMTs are used for many low level light (few hundred photons) detection applications. It is the most popular detector for all studies requiring quantitative measurement of photon fluxes.

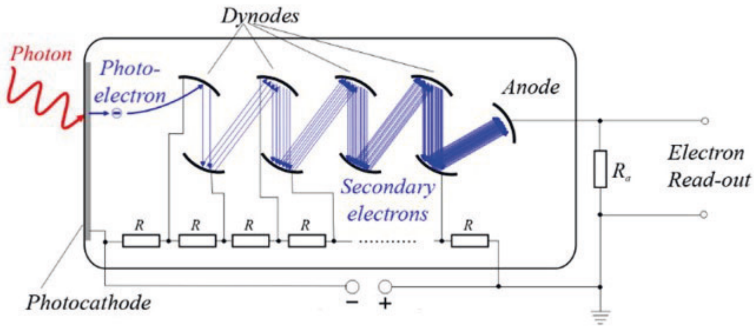

Figure 2.2: Schematic of a photomultiplier tube (PMT). Source: Wikipedia.

PMTs behaves like a light driven current source (see Fig. 2.2). The operating principle of PMTs is the photoelectric effect [19] accompanied by the Compton scattering mechanism for photons with higher energies and electron secondary emission. It consists of a vacuum tube to which a so-called photocathode is attached. The photocathode is made of materials adjusted to the nature of impinging radiation that undergoes the photoelectric effect that creates a cloud of electric charge. The charge is finally injected into the vacuum tube, following the electric field lines caused by the potential drop existing between this photocathode, the different dynodes (5 - 7) and, the electric anode fixed on the other side of the vaccuum tube.

When light enters the PMT via the entrance window and impinges the photocathode, primary electrons are generated as a result of the photoelectric effect. Then the electrons are accelerated by a high voltage towards the first dynode to generate secondary electrons. The secondary electrons are then accelerated towards the second dynode producing more electrons and so on (see Fig. 2.2). The electron multiplication process stops at the last dynode, which acts as the anode and is connected to an external electronics circuit to process the signals. This was first realized commercially in 1940s at *RCA* group in New Jersey, USA with a single amplification stage [20].

Over the decades, the photodetector of choice for scintillator detectors are PMTs with near single-photon detection ability, mainly due to their high internal gain (10^5 - 10^7). In recent years, their detection efficiency has exceeded 35 %, but drawbacks such as fragility and sensitivity to magnetic field, i.e. deflection of electrons within the vacuum tube and deviation of motion towards the dynodes hindering their performance, limits their applicability. The most suitable replacement to circumvent these drawbacks would be SiPMs, that

Table 2.3: Qualitative comparison between SiPM and PMT.

Photodetector	Silicon Photomultipliers	Photomultiplier Tube
Compactness	👍	👎
Operating voltage	👍 (25-70 V)	👎 ($\sim$1000 V)
Magnetic field insensitivity	👍 (several T)	👎 (mT)
Time resolution	👍 (ps)	👎 (ns)
Operational cost	👍	👎
Scalability	👍	👎
Radiation hardness	👎	👍

have comparable gain and advantages of a better technology: semiconductor over vacuum tube. The SiPMs are more rugged and compact than PMTs. Moreover, their operating voltages (tens of volts compared to kilovolts) and timing resolutions (tens of ps to hundreds of ps) are significantly lower if compared to those present in PMTs. Implementation in Silicon technology also provides significant advantages in terms of cost and scalability, crucial when large number of channels have to be operated. Furthermore, in-susceptibility towards magnetic field is also better (up to several Tesla vs. few mili Tesla) in SiPMs. The features listed in Table 2.3 summarize the comparison between these two photosensors emphasizing the advantages in performance and operating conditions of SiPM.

For the present study the photodetector employed is a digital SiPM, referred to as Philips Digital Photon Counter (PDPC) (discussed in detail in sec. 3.4) in this work, developed by *Philips*. Additionally, two analog SiPM arrays have been employed for the characterization of SiPMs' PDE and TR under the exposure of cold neutrons to asses the feasibility of technology for these application. The details of the analog arrays are shown in the Table 2.4.

The PDE of the Philips digital SiPM (PDPC) sensor at 390 nm, the peak wavelength of the GS20® (Ce-activated lithium aluminosilicate with 95 % ^{6}Li enrichment) scintillator glass emission, is approximately 30 %. As it can be observed in Fig. 2.3, the peak PDE of 45 % is reached by the PDPC at 420 nm wavelength, which is an acceptable match.

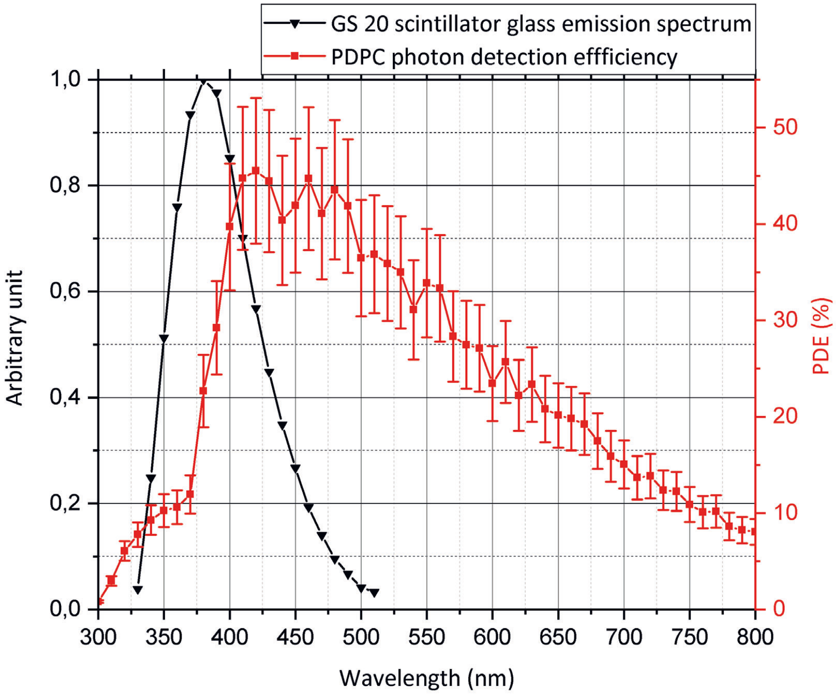

Figure 2.3: Graph showing the comparison of GS20® scintillator glass emission spectrum for thermal neutrons and photon detection efficiency (PDE) of the PDPC sensor. The sensor has ∽30 % PDE at 395 nm, the peak light emission of the scintillator, and 31 % PDE averaged across the whole emission spectrum.

Table 2.4: Characteristics of analog SiPM arrays fabricated by *SensL* and *Hamamatsu*, taken from the data sheet.

Physical Characteristics	SensL	Hamamatsu
Model	C Series 30035-144P	S12642-0808PB-50
Outer dimensions	50.2 mm × 50.2 mm	22.4 mm × 25.8 mm
Active area	3 mm × 3 mm	3 mm × 3 mm
Number of SiPMs	12 × 12	8 × 8
SiPM pitch	4.2 mm	3.2 mm
Number of microcells per SiPM	4774	3464
Microcells size	35 µm × 35 µm	50 µm × 50 µm
Breakdown voltage$^\bigstar$	∽25 V	∽65 V
Microcell fill factor	64 %	62 %
Detector fill factor	51 %	87.9 %

($^\bigstar$at room temperature)

Chapter 3

Silicon Photomultipliers

SiPMs are state-of-the-art sensors for light detection, sensitive to single photons together with good counting capability. The invention of modern SiPM dates back to 1990s in Russia first proposed by V. Golovin [21] and Z. Sadygov [22]. Since then, several research groups and commercial manufacturers developed their own versions of SiPMs [23–25]. They are also known as solid state photomultiplier (SSPM), metal-resistor semiconductor (MRS) APD, multi pixel photon counter (MPPC), micro-pixel avalanche photodiodes (MAPDs), avalanche micropixel photodiode (AMPD), or Geiger mode avalanche photodiode (GMAPD). For a recent overview of SiPM technology and parameters, refer to [26].

Its evolution is based on several generations of silicon photodiode developments [27]. The first predecessor was the PIN (p-intrinsic-n) photodiode, which is a diode with an intrinsic region sandwiched between highly doped p- and n-type semiconductor regions. The intrinsic layer is fully depleted and typically 5 µm to 50 µm long. The technology was invented in 1950s and boosted the first large scale application of Silicon sensors for low light detection in research. It operates with an applied reverse bias voltage without any internal gain. The noise range of several hundred electrons and no gain, limits the detectable light flux to 10^8 - 10^9 photons/mm^2. The next development aimed at decreasing the noise at high bandwidth in order to increase the sensitivity. In this regard APDs were proposed, which are p-n devices operated slightly below the reverse breakdown voltage, but with a high electric field at the junction of positively and negatively doped silicon [28]. This leads to internal multiplication (50 - 200) of the charges and consequently, an increase in light detection of two orders of magnitude, but affected by strong excess noise factor (F $\backsim$ 5) (refer to sec. 3.5.2) [29]. It can detect single photons only in the most favourable cases under severe limitations. Another effort to develop single photon sensitive semiconductor sensor was visible light photon counters (VLPC) [30]. The major drawback of this detector was maintaining operating temperature at cryogenic level (4K). It turned out to be impractical for widespread applications.

The path finding work that laid the foundation for low photon flux detection above the breakdown, the so called Geiger mode avalanche photodiode (GMAPD) was done by R. H Haitz and R. J McIntyre. Latter postulated the theory of microplasma[1] instability in avalanche regime in Silicon [31], and Haitz contributed for more appropriate model explaining the cause for the avalanche breakdown behaviour and the study of multiplication processes in Geiger mode photodiode operation (i.e. using reverse bias voltages well above the breakdown limit) [32]. Based on these findings, APDs operating well above the breakdown voltage, were developed, which have a diverging multiplication process resulting in gain comparable that achieved by the PMTs, but with a limited sensitive area. Those were called GMAPD or Geiger avalanche photodiode (GAPD) due to the similarities with a Geiger Mueller counter: avalanche multiplication process and amplification of ionization [33]. Owing to single photon detection ability, they are also named as single photon avalanche diode (SPAD) [34]. With the advancement in technology, the next step was the development of an array of SPADs (100 to 10 000 per mm^2), commonly known as SiPM. The latter is fabricated on a single wafer with each SPAD having its individual quenching element to overcome the large area amplification instability. All SPAD-quenching element combinations (microcells) are connected in parallel and have a common analog output signal.

The development material for these photodiodes are Si, InGaAs as well as widegap technologies. The different materials are chosen depending on their light detecting capabilities; Si is commercially available for wide spectral range from 350 nm to 900 nm; for telecommunication wavelengths (1.3 µm to 1.5 µm) InGaAs/InP as well as Ge are successfully tested; and SiC and GaN are utilized for ultraviolet range. As stated earlier, the wavelength range of interest for this work is in visible region, so unless stated otherwise this literature deals with Silicon SPAD only.

Thanks to rapid development and capability to detect faint light events at few photon level, SiPMs are becoming valid and economical alternatives to PMTs in basic research and industries. Innumerable applications are in progress or development which make use of SiPM, as for instance in experimental physics, homeland security, biochemistry, cryptography, 3-D

[1]factors producing the local electric field strength

imaging and many others. In autonomous driving for LIDAR (light detection and ranging) receiver, SiPMs are considered promising photodetectors mainly due to superior TOF resolutions and high sensitivity [35]. Germanium based single-photon detectors are employed in quantum cryptography, increasing quantum key distribution distance without eavesdropping between transmitter and receiver [36].

The immunity to magnetic fields make the SiPMs an attractive alternative in nuclear medicine applications for positron emission tomography (PET) scanners [37], in combination with magnetic resonance imaging (MRI), which lead to interesting investigations in biomedical imaging [38]. SiPMs are also suitable for gamma-ray astronomy, and for imaging atmospheric Cherenkov telescopes, exploiting the intrinsic photon counting capabilities of SPADs [39]. They have also applications in biophotonics for fluorescence lifetime imaging (FLIM), time-resolved Raman spectroscopy, and near-infra-red optical tomography (NIROT) [40].

3.1 Functionality of SiPM

A single SPAD does not give information about incident light intensity. This is due to the so-called "Geiger-mode limitation", caused by the quenching time the single SPAD microcell requires to eliminate all the charges generated within the avalanche process and restore the electric field required to create the conditions necessary for the next avalanche process to be started by a new incoming photon. For overcoming this issue, large number of SPADs are arranged in a matrix to form the SiPM that gives output proportional to the light flux. The output of an SiPM is the sum of all signals from the individual SPADs in the array connected in parallel (see Fig. 3.1). Its operation is based on detection of space and time distributed photons by photoelectric conversion. Essentially, its a p-n junction diode operating in photoconductive mode that tranduce light into electrical signal through the internal photoelectric effect: transition of electrons from the valence into the conduction band by interaction with an impinging photon, or an indirect transition for photon energies in the visible range using an additional interaction of a *phonon* (quantized unit of lattice vibration within the Si crystal) to change the electron crystal momentum. In contrast to zero biasing in solar cells that operates in photovoltaic mode, it is reversed biased and optimized for operating above breakdown voltage (V_{BD}) (see Fig. 3.2).

Once the photon is absorbed within the active volume of the diode, charge carriers are

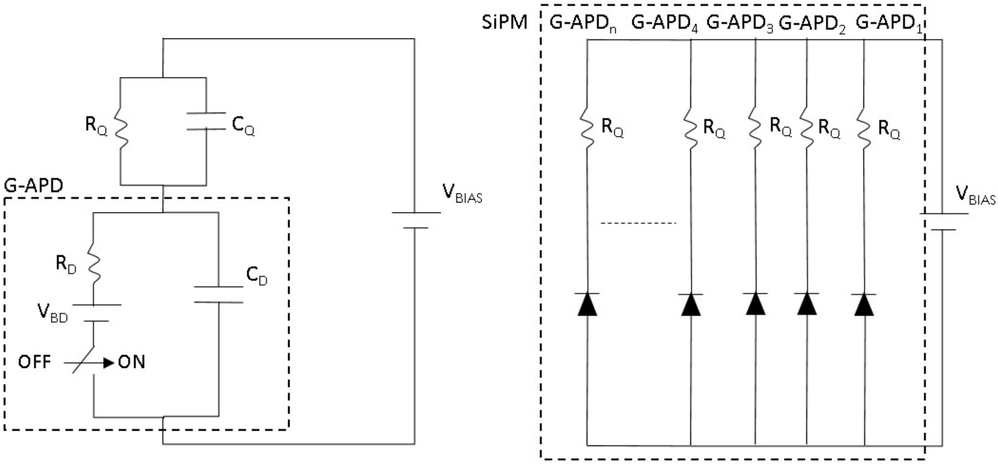

Figure 3.1: Circuit representation of a GAPD/ SPAD based on Haitz physical model [32](on the left). In the circuit shown here the resistance (R_D and R_Q) and capacitance (C_D and C_Q) stands for junction and quenching parameters. The circuit on the right shows the parallel combination of n × GAPDs, forming an SiPM.

generated and amplified due to *impact ionization* by high electric field, resulting in an output current up to milliampere range. This constant current flowing through the junction is disrupted by lowering the bias voltage due to the voltage drop at the quenching resistor R_Q (in case of passive quench). Afterwards, in few nano seconds (depending on the quenching circuitry) device becomes ready to detect the next photon by increasing the voltage. Contrary to APD proportional mode, where electrical conductivity (material´s ability to allow the transport of an electric charge) is limited due to only one type of carrier (electron) contribution (due to lower ionization rate of holes below breakdown, refer to sec. 3.5.3), leading to a linear gain, SPADs operate in "Geiger-mode" with theoretically infinite gain (see Fig. 3.2) and have avalanche triggering due to both carriers (refer to sec. 3.5.3).

By applying the reverse bias to the SPAD structure a depleted area, i.e. free from charge carriers, with low concentration of minority carriers is formed along with the built-in electric field between the p and n regions. If a photon hits in the multiplication region, also called avalanche region, where the avalanche multiplication takes place, it can create electron hole pair (EHP) [41]. EHPs are created due to the photoelectric effect and can initiate an electron avalanche process due to *impact ionization* that can be interpreted as internal amplification.

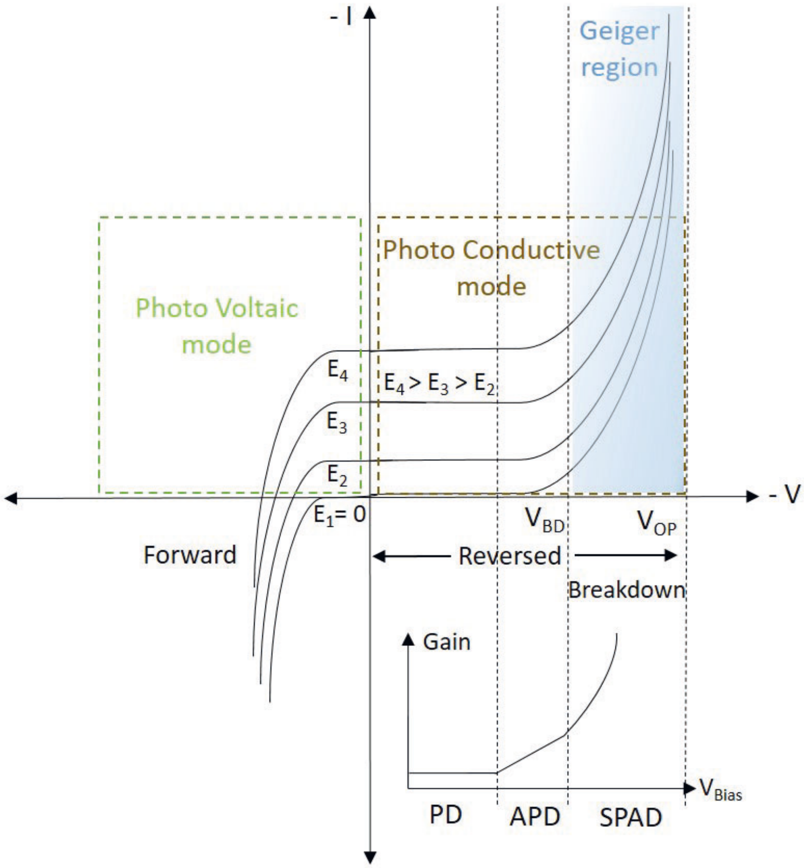

Figure 3.2: Depiction of an ideal Si p-n junction diode current-voltage characteristics curve for linearly increasing light ($E_4 > E_3 > E_2 > E_1$) for forward and reversed bias zone. The solar cells are operated in photovoltaic mode, whereas the photodiode in the conductive mode operates if reverse-biased. A curve of the approximate gain against the bias voltage for the single photon avalanche diode (SPAD), avalanche photodiode (APD) and photodiode (PD) is also shown in the graph along with their operating region.

The production of these free charge carriers is energy dependent and is established that photons above 3.6 eV generate direct band-to-band electron transitions, whilst photons with energies between 1.12 eV to 3.6 eV generate indirect electron transitions, a process in which a third particle - a *phonon* - is involved [42]. For incident energies of photon below the bandgap ($E_g = E_c - E_v$) i.e. 1.12 eV (>1100 nm) its transparent to SPADs, meaning does not absorb these photons. On the other hand, for energy higher than 4 eV (<310 nm) the absorption length is too thin (in the order of 100 nm) to produce an avalanche EHP. For a detailed discussion refer to sec. 3.5.3.

Due to the built-in field and applied field EHPs are separated. Electrons drift to the positively enhanced n-region and holes to the negatively enhanced p-region. When the applied field is strong enough, these free carriers reaches an energy higher than the ionization energy of electrons and holes to create more carriers by colliding with the crystal lattice. The field expedites the drifting of carriers and reduces the recombination chances. This phenomenon of charge multiplication chain is referred to as *impact ionization* [41], which results in an avalanche breakdown in the diode.

Two phenomena are at play during the avalanche process: carrier generation and recombination. In case of APD, which is operating slightly below the breakdown voltage, *impact ionization* (i.e. carrier generation) can still be controlled by carrier recombination, and the multiplication factor can be kept under control. This gives a self terminated avalanche and a finite gain, leading to a photocurrent generation. If biased above the breakdown voltage both, electrons and holes undergo *impact ionization*, the avalanche process is no longer controlled by recombination and additional measures are required to quench it. In this case the amount of charge produced during an avalanche process becomes irrelevant, and it is not used to calculate the amount of initially generated charge through a well established gain factor, but the idea is just to start counting the avalanche events, or more accurately the rising edge of the current pulses caused by these avalanche events, then the notion of gain becomes also irrelevant, and the concept of "infinite" gain can be found in literature to explain this readout principle.

The field required in the space charge region (SCR) or depletion region, created at the junction, to onset this avalanche is typically 10^5 V/cm or higher. Additionally, the thickness of the SCR has to be lower than the mean free path of the carriers, to facilitate this mechanism, else the carriers will recombine. The exponential growth of the number of carriers produces a self-sustaining current flowing through the junction that swiftly (sub ns range) grows until the space charge effect limits its value [41]. Thus, single photon driven carriers are detected due to a huge internal amplification process. This mode of operating above the breakdown voltage, i.e. at V_{OP} to initiate a diverging avalanche multiplication process, is known as “Geiger mode” (see Fig. 3.2) and the biasing difference between the operating voltage and the breakdown voltage is called excess voltage (ΔV). It is worth noting that in the absence of photon induced EHPs, thermally generated EHPs can also trigger an avalanche resulting in an indistinguishable, spurious signal called a “dark count” (see sec. 3.5.2). This sets some limitation on minimum detectable number of photons over a given period of time and is a major shortcoming of SiPMs.

Once an avalanche is triggered, the SiPM stays in Geiger regime, i.e. additional EHP-creation and secondary avalanche initiation. Thus, in order to detect the next photon it has to be brought back to the initial state by ceasing the current flow through avalanche termination.

There are two types of quenching process used for this purpose [34]. The simplest and most widely employed approach is passive quenching, where a high ohmic resistor (R_Q) is added in series to the SPAD. The current flowing through this resistor (Polysilicon or metal) causes a voltage drop across the junction due to which the bias voltage starts to subside. The circuit drives the voltage below the breakdown voltage to a quiescent level. After the quenching, SPAD transits back to the initial state within a recovery time dominated by the quenching resistor, R_Q and junction capacitance, C_D (see Fig. 3.1). Then the circuit concludes the cycle by resetting or recharging the SPAD, i.e. driving the voltage back above the breakdown (see Fig. 3.3), for next photon detection. Fig. 3.4 show an example of a passive quenching circuit.

A delicate way of quenching is using a transistor based circuit, that enhances the slow recovery of SiPM as concequence of passive quenching. In active quenching see (Fig. 3.5), first introduced by Antognetti et al. in 1975 [43], an external circuit is used to sense the voltage at the diode terminal and quickly reduce the bias voltage when an output pulse from SiPM is detected. The circuit consists of a combination of electronic switches and a power supply, which acts as pulse picker working in a feedback loop. It is capable of sensing the leading edge of the pulse (commonly by a comparator), generating an output pulse synchronous with triggering, and quenches the avalanche by lowering the voltage. After the quenching is completed, the same or a different circuit is used to restore the SPAD back to the operating voltage, thus preparing it for the next detection.

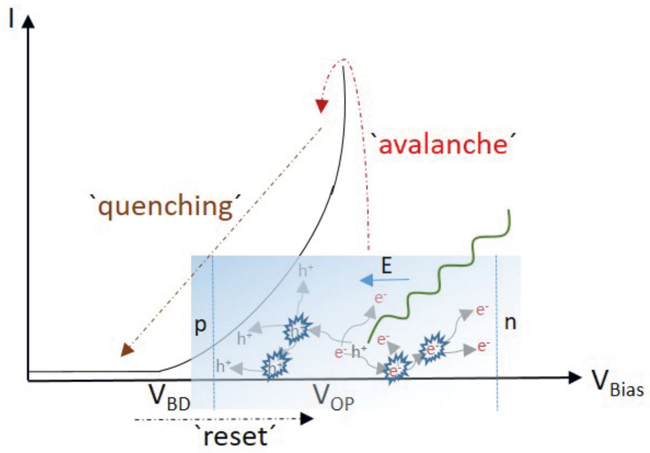

Figure 3.3: Representation of a quenching cycle in SiPM along with impact ionization mechanism initiated by a photon absorbed in the SiPM that generates an EHP and gets multiplied due to high voltage of operation (V_{OP}), corresponding to the avalanche phase. Then its quenched back below to breakdown voltage (V_{BD}) to allow the reset process for subsequent photon sensing.

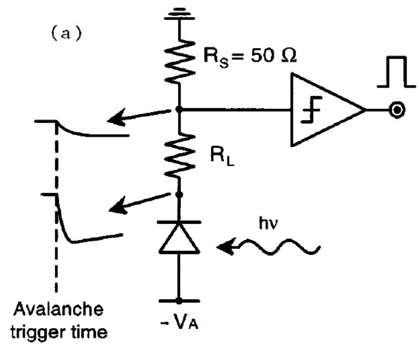

Figure 3.4: Example of a circuit diagram for passive quenching. R_L and R_S are load and series resistance. Picture taken with permission from [44].

The quick quenching approach provides the possibility to detect more avalanche events occurring during the reset phase, in addition to a reduction in after-pulsing (detailed in sec. 3.5) probability due to less charge crossing through the junction and reduced probability of trap occupation. Moreover, optical crosstalk (refer to sec. 3.5) is also reduced because fewer carriers generate fewer secondary photons. The active mode also enables SPADs to be a trigger counter for every avalanche event detection. However, radiation tolerance of the electronics used in active mode is a matter of concern for its applicability in environments with radiation. A detailed review of active and passive quenching mechanisms can be found in Cova et al. [44].

During the detection/recharge cycle, the sensor remains insensitive and the time between avalanche onset and voltage reset is known as dead time (see Fig. 3.6). Once it is quenching, no impact ionization takes place and this process lasts several 100 ns in case of passive quench and about 10 ns for active quenching.

3.2 Topology of SiPM

Out of various structures proposed and investigated for SPAD along with ongoing recent developments, its a tedious task to choose some common structure. However, based on the thickness of the junction it can be broadly classified into two groups: thick, reach-through (see Fig. 3.7a) [45] and thin, planar (see Fig. 3.7b) [46]. The main difference arises from the drift region (refer to sec. 3.5) thickness, as in both structures multiplication region size is similar.

In reach-through structure SCR spans tens of micrometers. This results in a trade-off between PDE and TR of the SPAD (refer to sec. 3.5). Due to the wide region the diffusion tails contribution caused by photon-assisted propagation results in poor TR, on the other hand higher PDE for red and near infrared (NIR) region is achieved. Also the breakdown voltage is higher (one order of magnitude) than thin SPADs, in turn requiring a cooling system. However, as the illumination takes place in p- region (p-epitaxial) and p-type layer, the minority carrier (electrons) injected into SCR reduces noise and enhances the gain.

The first planar device was proposed in the 60s by Haitz et al. [32]. They are also termed as thin SPAD due to SCR of up to few microns only. The junction generally consists of a doped diffusion implant over an opposite doping type substrate. Different structure has to be fabricated to adapt according to the sensing range: p over n for blue light and n over p for red light (see Fig. 3.8). Generally for red light in a n+/p/p-epi/p+ structure, the junction is built by a n+ region on a lightly doped p-epi layer which was grown on a highly doped p type silicon substrate (p+). In order to control the breakdown voltage to a desired value a second p-type region is created underneath the n+ region. For achieving a good PDE n+ layer needs to be shallow and the high field region should be as thin as possible [47]. Corresponding to the doping profile the drift region is formed by the p-epi division, so called the active thickness of the device and a high field avalanche region is formed around n+/p region (see Fig. 3.9). In contrast, in p+/n/n-epi/n+ structure (see Fig. 3.10) optimized for

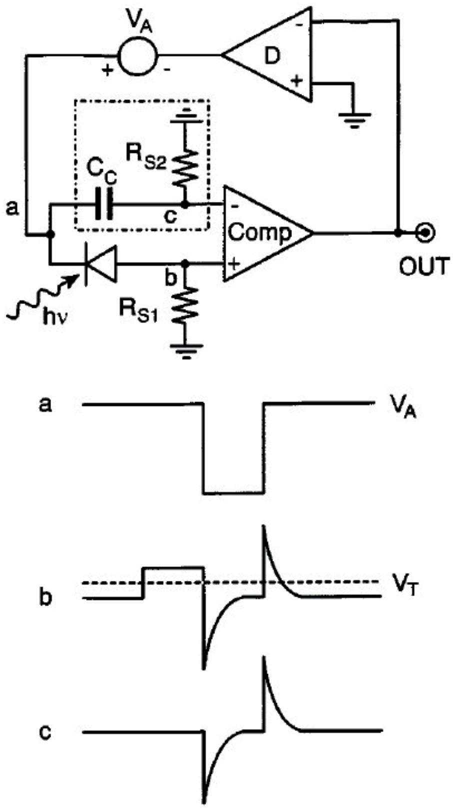

Figure 3.5: Simplified diagram of a basic active quenching circuit used in [44], reprinted with permission. The network in the dotted box compensates the current pulses injected by the quenching pulse through the SPAD capacitance, thus avoiding circuit oscillation. The voltage waveforms drawn correspond to the circuit nodes marked with the same letter.

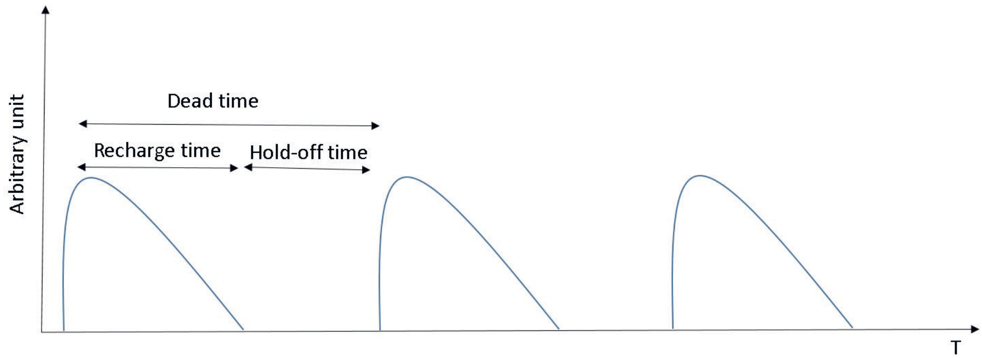

Figure 3.6: A simplistic curve for an SiPM signal over time. During the dead time the sensor remains "blind" for any impinging light.

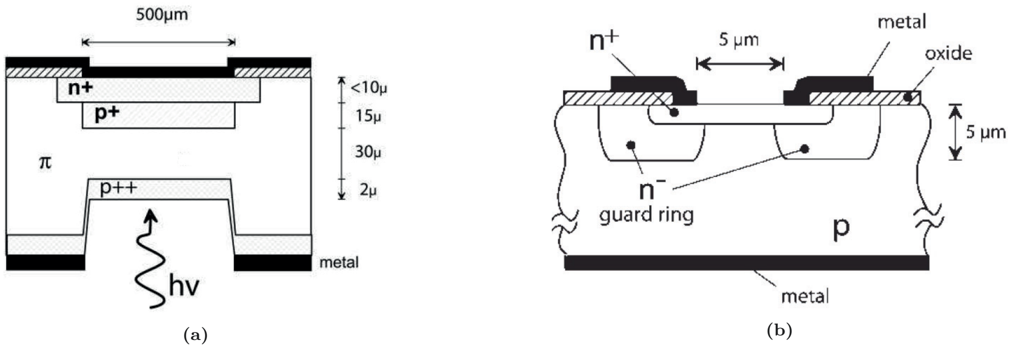

Figure 3.7: Sketch of a SPAD for (a) reach-through (thick) structure proposed by McIntyre and Webb [45] (b) planar (thin) structure investigated by Haitz [46].

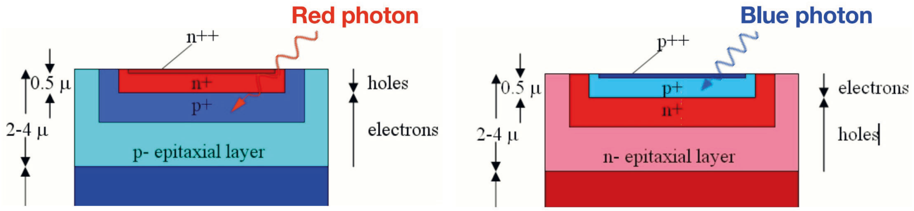

Figure 3.8: Example structures of SiPM optimized for red light sensitivity (n on p substrate) and for blue light sensitivity (p on n substrate). Picture taken from [49].

blue light avalanche area is formed around p+/n junction built in a lightly doped n-type epitaxial layer grown on a n+ substrate [48]. It is worth mentioning that the electric field is correlated to the structure and shaped by the doping profile.

The shallow junction offers breakdown voltage in the order of few tens of volts only. It can be fabricated on a standard Si substrate using a planar fabrication process making it compatible with complementary metal oxide semiconductor (CMOS) technology combining the benefits of mass production CMOS microelectronics devices. Monolithic integration of the photodetector on the same chip with the pixel electronics exploits the technology features, such as reduced after pulse and trapping due to close proximity and prompt quenching by avoiding additional capacitive contributions due to interconnects [49].

3.3 Developments in SiPM

SPAD arrays are getting commercial attention for fabrication using customized CMOS processes, with extra implantation using additional fabrication masks [50–52]. The reason behind is that standard CMOS process does not yield a good phototransduction performance. The main challenges in implying standard CMOS technology for SPAD or SiPM fabrication are: higher DCR due to increased band to band tunneling (detailed in sec. 3.5.1) [53] and limited PDE in near infrared region caused by narrow SCR as a result of higher doping concentration used as compared to dedicated fabrication process with CMOS compatibility [54]. Moreover, field oxide structure used for device isolation in older planar CMOS processes, as well as shallow-trench isolation (STI) used in more advanced CMOS processes, both yield wavelength dependent variable radiation transmittance and add other optical effects, e.g. reflection losses. Additionally, intermetal Silicon oxide based isolation, as well as Silicon

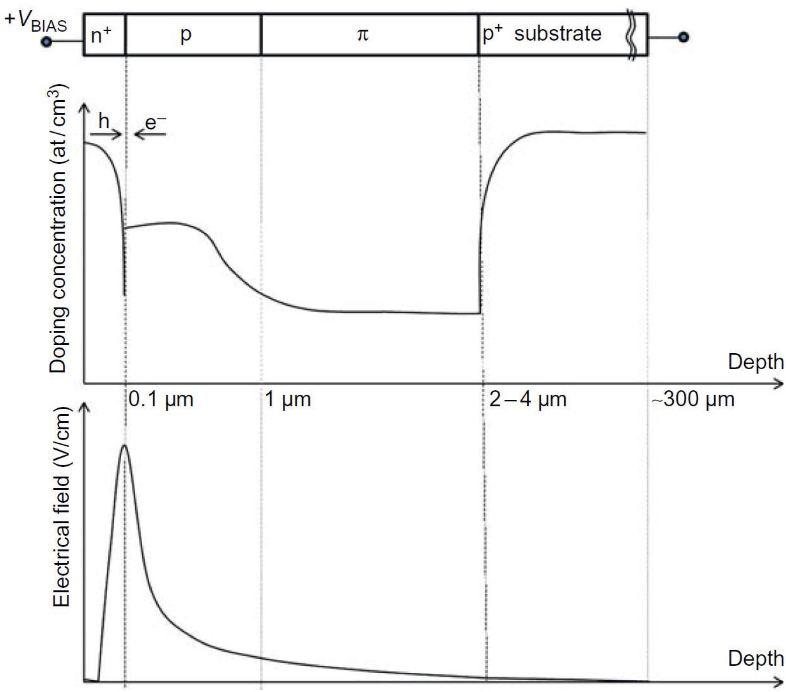

Figure 3.9: A graph of electric field and doping profile against the depth of the SPAD for n+/p/pie/p+ structure (optimized for red light). Reprinted with permission from [48].

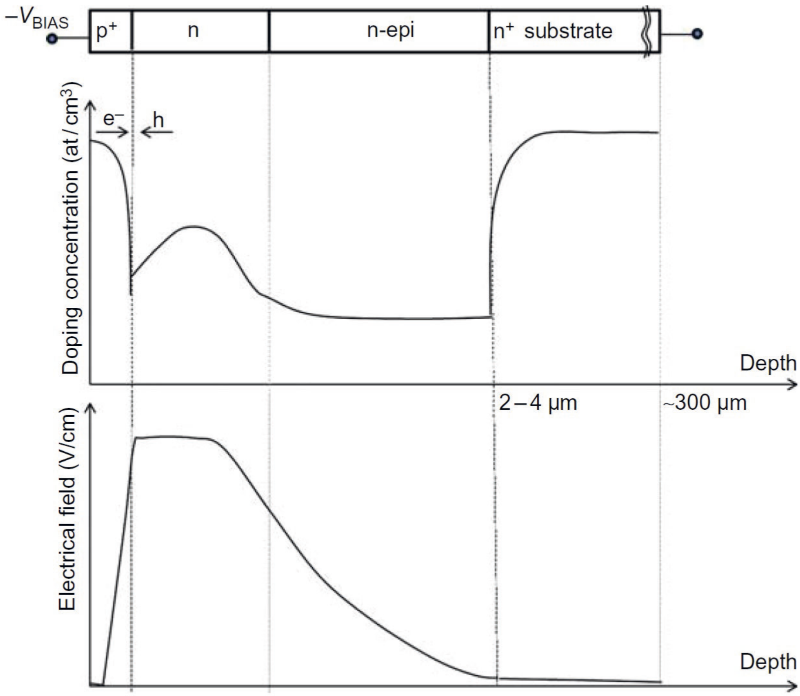

Figure 3.10: A graph of electric field and doping profile against the depth of the SPAD for p+/n/n-epi/n+ structure (optimized for blue light). Reprinted with permission from [48].

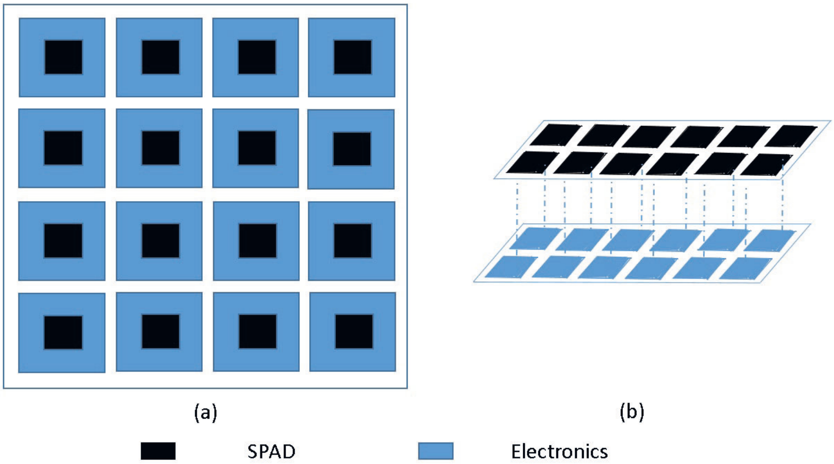

Figure 3.11: A generic sketch of the layout of a (a) 2D SiPM (b) 3D SiPM.

nitride based passivation layer absorb heavily in the UV-blue part of the spectra causing reduced quantum efficiency of the photodetector for that kind of radiation [54]. Nonetheless, the features such as mass production, cost effectiveness, good yield and ease of integration is fuelling the interest in both scientific and industrial communities to implement SPAD in standard CMOS technology without any process modification or special substrate.

Significant efforts are underway in this direction that are continuing the first attempts to improve the photodetection performance of these devices that started around 2002 [55, 56]. Since then as the fabrication technology matured a number of investigators have demonstrated 2D monolithic integration (see Fig. 3.11) of SPAD to explore the the different structure in CMOS [57]. Features of node size in 350 nm [58, 59], 180 nm [60], and 130 nm [61, 62] were also investigated. They are also integrated into smaller size of 90 nm [63] and 65 nm [53]. However, lower breakdown voltage (∼10V) leading to high DCR is a concern for CMOS processes with smaller technology node. A well reviewed article for some of the CMOS structures can be found in [57] and [60].

In order to increase the performance, studies on numerous structures of SPADs for electric field uniformity have also been carried out. As SPAD suffer from premature breakdown, arising from locally concentrated electric field at the junction edges due to curvature at device edges, guard ring structures also have been examined to overcome this effect [64, 65].

Another approach towards improving the performance consisted in increasing the photoactive area. Integration of the electronic circuitry (quenching and recharge circuits etc.) next to the individual microcells, limits the active area resulting in lower PDE. To avoid the latter, back side illumination (BSI) was proposed for SPAD arrays. As a next step, a flipped back-side illuminated SPAD array was integrated with the readout and quenching circuitry using the 3D integration approach. In this two chip coupled SiPM design approach, SPAD wafer were either flipped for BSI and bonded to CMOS electronics wafer [66] or electronic circuity were placed on another chip in the backside, coupled to SPAD illuminated from the front [67]. This provides the opportunity to integrate the application specific integrated circuits (ASIC) to be coupled with the signal from individual microcells. In addition, current-assisted SPAD is also an option to increase the active area. In this approach, a large and deep absorption volume guides the minority carriers to a small pn-junction in the center due to the drift field [68]. However it has very low PDE and high TR.

In recent years advancement in the conception of SiPM is 3D stacked technology, inspired from the two wafer coupling approach and progresses in 3D integration processes [69, 70] to increase the performance by dramatically improving the active area [71]. In a 3D-stack approach, top tier is occupied by the SPAD chip placed on top of a chip for all circuitry, placed on the bottom tier. This also provides the opportunity for development and coupling of tiers: custom optimized technology (for SPAD) and state-of-the-art technology (for electronics). The main advantages of this emerging technology are low power consumption, better timing resolution and strong potential of more advanced functionality. The SPAD array can either be front side illuminated (FSI) or back side illuminated (BSI) (see Fig. 3.12). The difference between the fabrication processes used in each of these two approaches is in coupling, i.e. through silicon via technology (TSV) is used to vertically connect each SPAD to the pixel circuit in front illuminated, whereas its directly connected face to face in the BSI approach. However, thinning of the SPAD wafer down to a suitable thickness (few µm) is an issue in BSI stacking [72], which is better for red and NIR region due to thicker junction [73]. Moreover, the integration of the SPAD array is generally done on wafer level, but a recent investigation on chip-to-chip in BSI shows a faster and further cost reduction approach per development cycle [74]. On the other hand, the front side illumination (FSI) approach is more useful with near ultraviolet (NUV) and blue spectra, because of shallow junction [75, 76]. In a recent development, a BSI 3D stacked SiPM in 45 nm CIS technology reports a PDE of 32 %, DCR of 55.4 cps/µm^2 along with timing jitter of 107.7 ps [72].

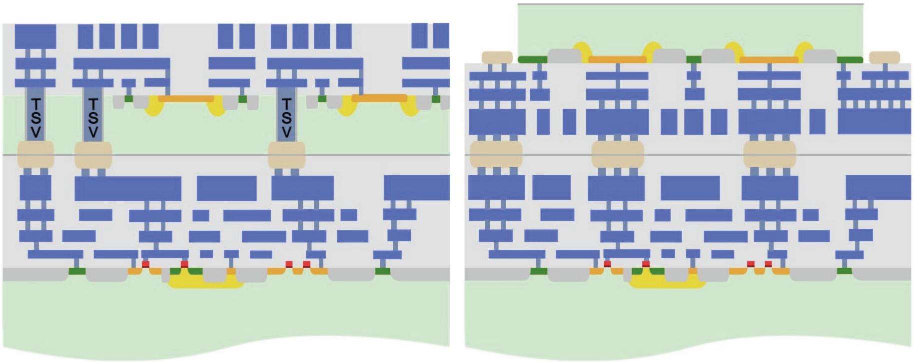

Figure 3.12: A simple diagram of front side and back side illumination in a 3D stacked CMOS SPADs. Picture reprinted with permission from [71].

Apart from these a line of development is ongoing for fabrication of SPAD arrays on 28 nm fully depleted Silicon on insulator (FDSOI) technology without any design rule violation nor process customization. The research group at INL, France under F. Calmon are focused on 3D monolithic (without tier stacking) integration of SPAD pixel with BSI [77, 78]. Within this approach an intrinsic 3D stacking is achieved by integration of the SPAD below the buried oxide with associated electronics on-top in the thin silicon layer.

For summarizing it can be stated that for a better SiPM the challenge lies in design and technology of semiconductors and its associated electronics. Within the last 15 years popularity of SiPM is increased gradually for different applications and users are favouring it due to its performance and features. This leads to a great deal of future development with the prospect of further improvements and advancement.

3.4 Philips Digital SiPM

SiPMs have an intrinsic digital behaviour due to the binary nature of the microcell, that provides same signal shape and amplitude that can be represented by two levels of electronics signal. For each microcell, detected photon is “1” and not detected is “0”, that sums up the information in a microcell as 1 bit. It actively draws current only when it is switching, like a CMOS logic element. The implementation of the SPADs in a CMOS process makes it acceptable for digital signal processing that quickly switches from one logic state to the other

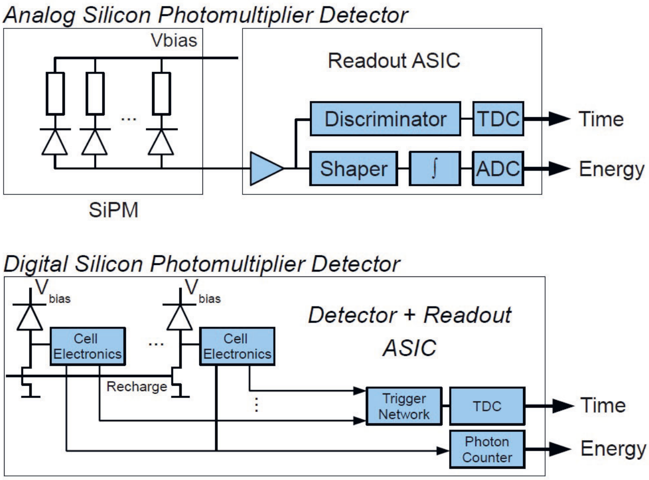

Figure 3.13: Schematic of the SiPM for the uses where time and energy is expected as the output for a generic analog SiPM and for the digital SiPM from *Philips*. Reprinted with permission from [82].

upon the detection of a photon. More details on digital SiPMs can be found in [79–81] with the focus on biomedical engineering applications.

The first effort for a commercial development of digital SiPM (dSiPM) was taken by *Philips Digital Photon Counting GmbH* group in 2009 [82], with PET applications in mind [83]. The output of the digital SiPM is the total number of photons detected over the SiPM area, against a signal that needs to be processed by a front-end electronics in the case of an analog SiPM (see Fig. 3.13). The output also contains the well-defined timing information with respect to the first detected photon. This is achieved by early digitization (cell electronics) of microcell output due to avalanche breakdown and integrated electronics that contains active quenching and recharge circuitry, on-chip time-to-digital converter (TDC) and a digital counter. The electronics blocks are placed next to each microcell with 2D monolithic integration approach using a commercial 180 nm CMOS process. However, not every single SPAD is connected to a TDC resulting in trigger network skew influences and leading to an impact on single photon time resolution achieved in case of individual connections (see Fig. 3.14). Nevertheless, early conversion of photon into digital signal exploits the intrinsic nature of SPADs, which is affected in analog SiPMs due to parasitic capacitances and inductances of the interconnects, the influence of electronic noise and the sensitivity to temperature drifts

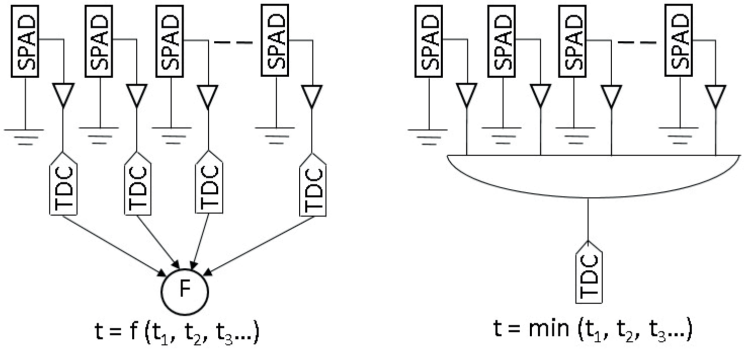

Figure 3.14: Architecture of a digital SiPM for (a) an individual TDC for each SPADs (b) a TDC for few SPADs from *Philips*.

(see Fig. 3.13).

3.4.1 Architecture of Philips Digital SiPM

For this work 4 SiPM *modules* from *Philips* are used. In contrast to the integral output current of an analog SiPM, the breakdown of each individual SPAD is sensed by local voltage change that leads to a faster response and less susceptibility towards temperature variations, interference, unstable baseline, and noise. The thin device structure provides a timestamp with low time jitter. Additionally, it is easy to use without requiring any front-end electronics, and gives in principle accessibility to every individual SPAD.

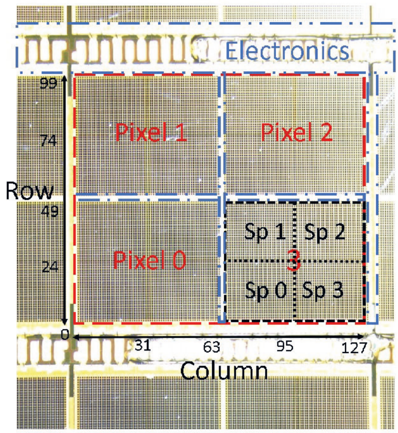

Figure 3.15: Micrograph of a *subpixel (sp)* and *pixel* (64 × 50 = 3200 microcells) of a digital SiPM (PDPC) module along with on-chip electronics.

The PDPC *modules* (see Fig. 3.16) have a dimension of 65.4 mm × 65.4 mm and comprise an array of 2 × 2 DPC3200-22-44 *tiles* and each tile is composed of 8 × 8 SiPMs (referred to as *pixels* here) with a 4 mm × 4 mm pitch. Every 2 × 2 pixels form a *die*, which is an independent read-

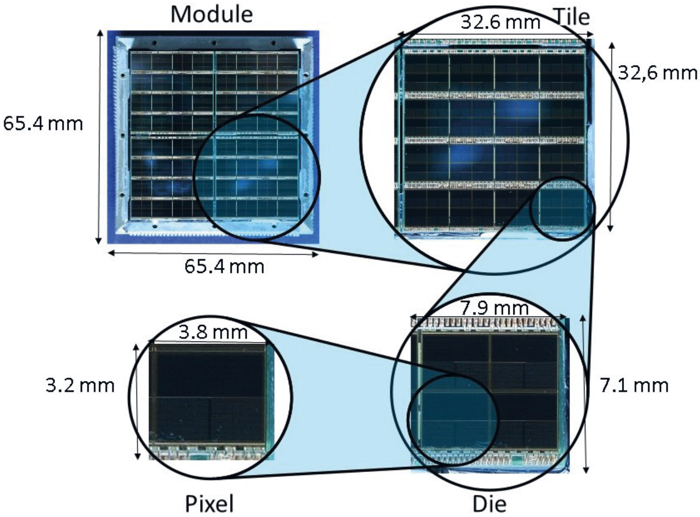

Figure 3.16: Dimensions of a digital SiPM (PDPC) *module* employed in this work. In total 16 × 16 SiPM are assembled together in a module or 8 × 8 independent readout units (*die*) and each is subdivided into 2 × 2 *pixels*. A dSiPM constituting 3200 microcells is referred to as pixel here, reproduced with permission from [139].

out unit with fully digital interface. Each pixel is constituted by an array of 3200 individual SPADs (referred to as microcells here) of dimension 59.4 µm × 64 µm, operating in the Geiger-mode (∼3V above the breakdown voltage). For the detailed specification of the sensor refer to Table 3.1.

With the purpose of avoiding the spatially distributed false counting within a pixel due to the dark count, *subpixels* are designated and are connected logically. The *subpixels* are build by an array of 32 × 25 microcells (see Fig. 3.15) and a row trigger line (RTL) is connected to a line of 16 microcells. The implementation of an addressable memory cell to enable and disable the corresponding microcells, gives the possibility to "disconnect" or simply not consider the signals coming from certain microcells or entire subpixels. This feature is called "masking". Masking is used to inhibit the contribution of the so-called hot-cells (microcells with an abnormally increased DCR), at the expense of PDE.

Table 3.1: Characteristics of digital SiPM (PDPC) taken from the manufacturer datasheet.

Pysical characteristics	DPC3200-22-44
Outer dimensions	32.6 mm $\times$ 32.6 mm
No. of dies	16
Pixel pitch	4 mm $\times$ 4 mm
Pixel active area	3.8 mm $\times$ 3.2 mm
Number of cells per pixel	3200
Number of cells per subpixel	800
Cells size	59.4 µm $\times$ 64 µm
Surface protection	100 µm glass plate + 75 µm glue
Max. event processing rate of tile FPGA	122 kcps per die
Spectral response range	380 nm - 700 nm
Peak sensitivity wavelength (λ_p)	420 nm
Photon detection efficiency @ λ_p	40 %
Pixel fill factor (already included in PDE)	74 %
Tile fill factor (already included in PDE)	55 %
Dark count rate (95 % cells active)	$<$ 140 kHz/ mm^2 @20°C
Operational bias voltage	27±0.5 V
Temperature dependence of dark count rate	double every 7.5 K
Intrinsic timing resolution$^{\#}$	44 ps
Operating temperature	0°C to 40°C

($^{\#}$for approximately 1000 photons)

3.4.2 Operation of Philips Digital SiPM

The PDPC comes with a full integration of digital acquisition, processing, and readout of optical signals that allows to detect the photons digitally. After detection of a photon, its actively quenched by a dedicated transistor circuitry and recharged back to the initial state, ready for the next photon detection. Each microcell is equipped with a digital inverter, to give a digital output for a detected photon, which is noted by an on-chip counter along with all other triggered microcells to provide photon counts. Fig. 3.17 shows the flow of the signal and the data in the sensor.

In this approach, the amount of generated charge is no longer important. One rising signal edge means there is an avalanche event occuring within the cell triggered by an incoming electron. Depending on the quantum efficiency of the SPAD device, that electron can be a photogenerated one. To be able to statisically separate the thermally generated electrons (DCR, refer to sec. 3.5.2) from the photogenerated ones, a proper temperature-dependent characterization of the SPAD array in absolute darkness must be performed, and the average amount of dark counts occuring in a certain light integration time must be substracted from the overall sum of avalanche events counted by the digital counter when in full operation (if the temperature remains same).

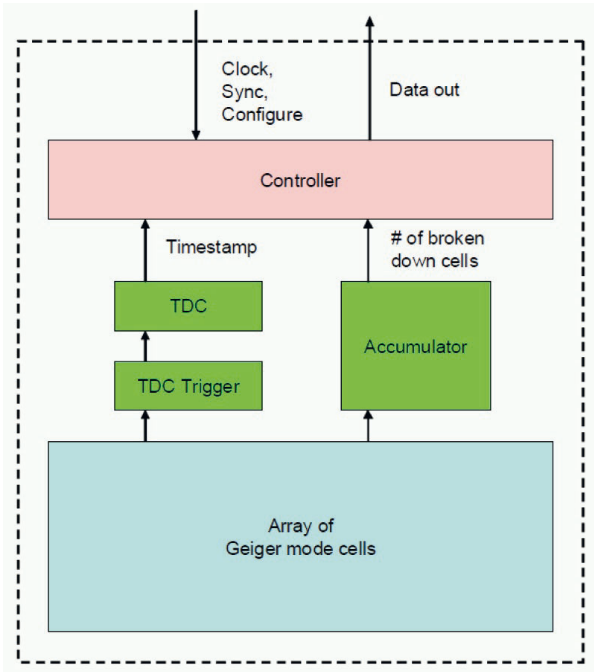

Figure 3.17: Block diagram of the signal flow within the digital SiPM (PDPC) showing the TDC and controller, which is triggered by detection of an optical signal. Picture taken from [82].

Table 3.2: Four trigger schemes and the logical (+ : OR, · : AND) interconnection of subpixels in PDPC (Adapted from V. Tabacchini et al., JINST, vol. 9(6), P06016, 2014).

Trigger scheme	Logical interconnection of subpixels (sp)	Min. no. of fired cells	Avg. no. of fired cells
1	sp1 + sp 2 + sp3 + sp4	1	1
2	[(sp1 + sp2) · (sp3 + sp4)] + [(sp1 + sp4) · (sp3 + sp3)]	2	2.3
3	(sp1 + sp2) · (sp3 + sp4)	3	3
4	sp1 · sp2 · sp3 · sp4	4	8.3

The four sub-pixels in a pixel are connected ANDed or ORed by a trigger logic that allows to select the trigger scheme (see Fig. 3.18). According to the application, the levels are selected to reduce the sensitivity towards dark count generated triggers. The Table 3.2 shows all four logic schemes and the corresponding association of sub-pixels. These schemes are statistical threshold that is dependent on photon distribution among the subpixels. With the assumption of homogeneous distribution of photons over the PDPC area, for logic 1 the four inputs are ORed to generate a master trigger if any of the subpixels generates a trigger signal, whereas this will happen only if all four sub-pixels are triggered in case of logic 4. The RTLs of 25 rows generates a sub pixel trigger signal initiated either by a photon or dark count event. Thus, for further suppression of dark counts the subpixels are subdivided into validation region to meet a second high-level threshold.

In validation condition the regions have further logical connections. Different validation patterns can be implemented to get to a logical *true* state of a subpixel. The schematic layout of the validation logic is shown in Fig. 3.18, while Table 3.3 shows the standard pre-configured pattern by the manufacturer. Once these logical conditions are met, the master trigger output of pixels are generated in a die, that are always connected logically by an OR gate. The master trigger serves as the start signal for a 9-bit TDC, whose reference clock is used to generate the stop signal. For overcoming the metastability of TDC created due to coincidence of the stop and start signals, two TDCs with complimentary clocks are utilized in the PDPC. The 200 MHz clock signal is internally generated and divided by 2 to track the absolute time of the event by a coarse counter [81].

The TDC unit and the main controlling unit are both shared by all the microcells in

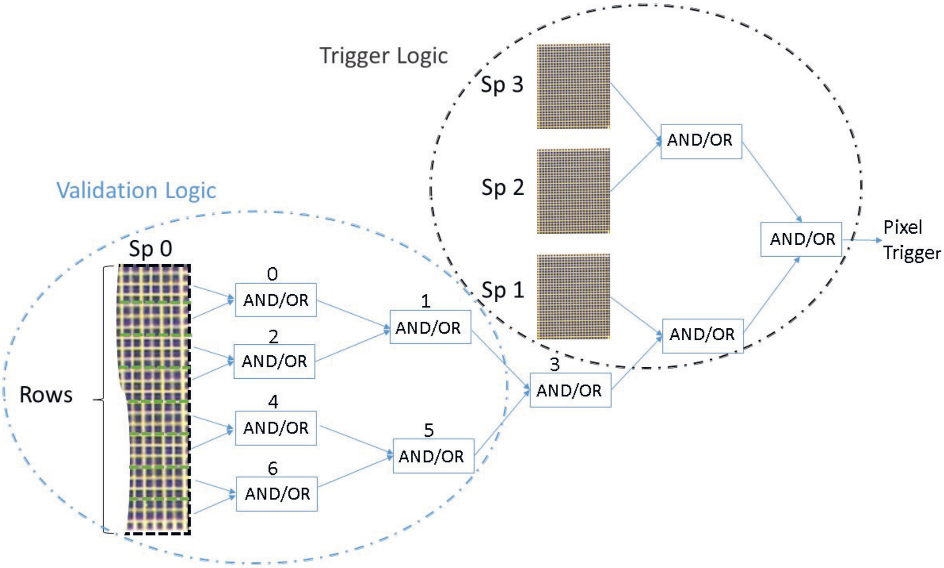

Figure 3.18: Schematic of subpixel validation and trigger logic in built in the digital SiPM (PDPC).

Table 3.3: Validation schemes and their corresponding logical interconnection of subpixels in PDPC (Adapted from V. Tabacchini et al., JINST, vol. 9(6), P06016, 2014).

Validation pattern	Logical gate assignment 0	1	2	3	4	5	6	Sub-pixel connection
1-OR	OR	OR	OR	OR	OR	OR	OR	OR
2-OR	OR	OR	AND	OR	OR	OR	OR	OR
4-OR	OR	AND	OR	AND	OR	AND	OR	OR
8-OR	AND	AND	AND	AND	AND	AND	AND	OR
4-AND	OR	AND	OR	AND	OR	AND	OR	AND
8-AND	AND	AND	AND	AND	AND	AND	AND	AND

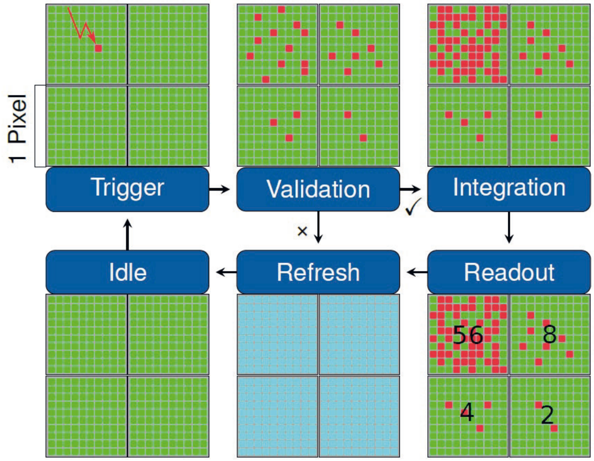

Figure 3.19: Visualisation of acquisition sequence of digital SiPM (PDPC) readout. Reproduced with permission from [156].

a PDPC pixel. The main controller implements the event based acquisition sequence (see Fig. 3.19) using a finite state machine (FSM). The FSM stays in a READY or IDLE state until a master trigger from any of the pixels in a die, satisfying the configured pixel logic, starts the acquisition of the event. This leads the FSM into a user defined *validation interval*. The duration of this can be up to 16 clock cycles (1 clock cycle = 5 ns), during which time it evaluates the probability of events to be validated as photon driven and reduces the dead time due to dark counts. If the validation threshold is not fulfilled, the sequence forces the FSM into the *refresh* mode to quickly (10 ns to 40 ns) recharge it to the IDLE state for next event, while the previous one is discarded. Else, it initiates the acquisition loop and enters into the *integration phase*.

The number of photons detected, used as a threshold to validate a certain event, can be seen as a analogous approach employed in analog SiPM to discriminate the background noise using the energy threshold. Within the radiation integration time (*integration phase*), which is configurable (0 µs to 20 µs), the sensor accumulates the subsequent photons belonging to the same event. After the integration, FSM enters into the *readout phase* (680 ns) and starts reading the triggered cells in each pixel with the output of data at a rate of ∽20 Mbit/s. Finally, the sensor is refreshed to prepare for the next detection.

Table 3.4: Settings of PDPC readout cycle utilized in the present work.

Trigger scheme	Validation scheme	Validation interval	Integration interval	Readout time	Refresh time
4	8-AND	35 ns	165 ns	680 ns	20 ns

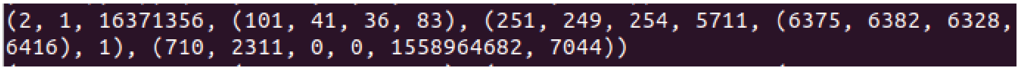

Figure 3.20: Snapshot of the PDPC output data for a single event.

For the present work, the sensor readout configuration are listed in Table 3.4. The structure of the output data packet provided by the modules is shown in Fig. 3.20 and is generically described below:

[tile number, die number, timestamp, (pixel 0 count, pixel 1 count, pixel 2 count, pixel 3 count), header)]

3.5 Characteristics of SiPM

Different parameters needed to be defined so as to properly interpret the operation of SiPM. The understanding of the nature and influence of said parameters on the performance of a system based on SiPMs varies within the community of scientists and engineers using it, and different research groups have their own symbols and definitions to represent them. Moreover, the methods to evaluate these parameters are also not the same. However, an effort was made recently in a review article [84] to summarize these parameters and its characterization methods.

The properties of SiPM depend on the geometry and fabrication of the microcells. Here, a generic figures of merit (FOM) is discussed and that can be categorized into the following three sections.

3.5.1 Static Characteristics

The fundamental element of an SiPM is a p-n junction diode so the current voltage (I-V) curve holds the key for its behaviour. As mentioned already, the sensor operates when sufficiently large reverse voltage is applied that leads to breakdown. For a p-n junction, two mechanism are responsible for the breakdown: *electron tunneling process* and *avalanche* *multiplication*. The large electric field created at the SCR due to the high doping (>10^{17} cm^{-3}) and applied voltage allows an electron to cross the potential barrier generated at the p-n junction and make a transition from the valence band into the conduction band right through the energy bandgap. This transition of valence electron from the valence band to the conduction band is known as *tunneling* [41]. The other process mentioned, avalanche multiplication or *impact ionization* is the mechanism that generates the EHPs. In order to generate EHPs the ionization rates, i.e. creation of EHP by an electron (α_{n}) or hole (α_{p}) per unit distance travelled, of the carriers must be high ($\sim 1 \times 10^4\,\mathrm{cm}^{-1}$). The rates for both the carriers are dependent on the electric field strength. The EHP generation rate G_A from the avalanche process is given by (3.5.1) [85],

$$G_{\mathrm{A}} = \frac{1}{q}\left(\alpha_n|\mathrm{J}_n| + \alpha_p|\mathrm{J}_p|\right) \tag{3.5.1}$$

where J_n and J_p are electron and hole current densities.

The voltage at which the EHP generation rate rises exponentially is referred to as avalanche breakdown voltage (V_{BD}) and is very well studied since 1960s [86]. Assuming the $\alpha_n = \alpha_p = \alpha$ condition for V_{BD}, for a given depletion width w, follows (3.5.2) [41]:

$$\int_0^w dx\ \alpha(x) = 1 \tag{3.5.2}$$

The breakdown can be initiated due to either of the above mentioned mechanisms or in combination, depending on the value of the V_{BD} compared to E_g/q, where E_g is the bandgap energy and q is the elementary charge. For $V_{BD} < 4{\cdot}(E_g/q)$, mainly *tunneling process* is responsible and for $V_{BD} > 6{\cdot}(E_g/q)$ *impact ionization*, while for in between values the result is a mixture of both processes [87]. For a p-n junction operating in Geiger mode, i.e. SiPM, the significant factor in breakdown mechanism is *impact ionization*.

It is evident from Fig. 3.2 that V_{BD} can be estimated from the I-V curve, however this value corresponds to the "onset of avalanche" and can differ up to 300 mV from values determined by other methods, such as for example their extraction from the gain vs. voltage bias curve, as explained in [88,89]. The lower value obtained from interpolation of the curve to the unity gain might be attributed to the "switching off avalanche" and other physical phenomena [88]. Moreover, there exists no standard method among the community for evaluation of the SiPM breakdown voltage.

The breakdown voltage strongly depends on temperature. At higher temperatures V_{BD} increases due to a decrease in the probability of impact ionization events, resulting from an increase of the amount of *phonon* scattering.

Once the junction breaks down, it conducts a very large current constituted by *drift* and *diffusion* components [85]. The drift current is generated due to the applied electric field that results in carrier transport along the lines of the electrical field with a maximum drift velocity (10^7 m/s for Si at 300K [85]). Another current is due to the carrier concentration gradient. Considering n+/p/p-epi/p+ structure, it is noted that mostly photons are absorbed in p or p-epi region because n+ is usually very thin and out of that p-epi and p are photogeneration or absorption and avalanche regions respectively. If the electron-hole pairs are generated outside of the SCR, they start diffusing and some of them eventually reach the SCR and get drifted by the electrical field induced there.

As it can be observed from Fig. 3.21 when a photon penetrates within a diffusion length outside the SCR photogenerated electron moves from high concentration to low concentration towards the SCR, phenomenon called as *diffusion*, and then drift to the n side. On the other hand, if absorption happens in SCR, due to the high field hole drift towards the p region to diffuse into the neutral p region and combines with electron entered from negative terminal. Resulting in photogenerated macroscopic avalanche current that follows the behaviour determined mainly by resistivity of the quenching element.

The forward I-V curve of the diode is utilized to evaluate the equivalent quenching resistor by evaluating the slope of the curve once the bias voltage exceeds the forward voltage (0.6 V for Si). Further, individual resistor values can be estimated by knowing the number of microcells and with the assumption of each having uniform value.

3.5.2 Dynamic Characteristics

In order to analyse the performance of the SiPM, it is important to understand its dynamic behaviour and a starting point could be the signal shape. Since, the carriers, generated either by thermal or photo events, traversing the high field region can trigger an avalanche. There exists no qualitative difference in the output of SiPM produced with or without light. Fig. 3.22 shows an example for the signal of an SiPM under light illumination along with its temporal characteristics. It is noted that the shape and the values are only valid for the output (standard/fast) used with the given readout electronics. The rise and fall time values

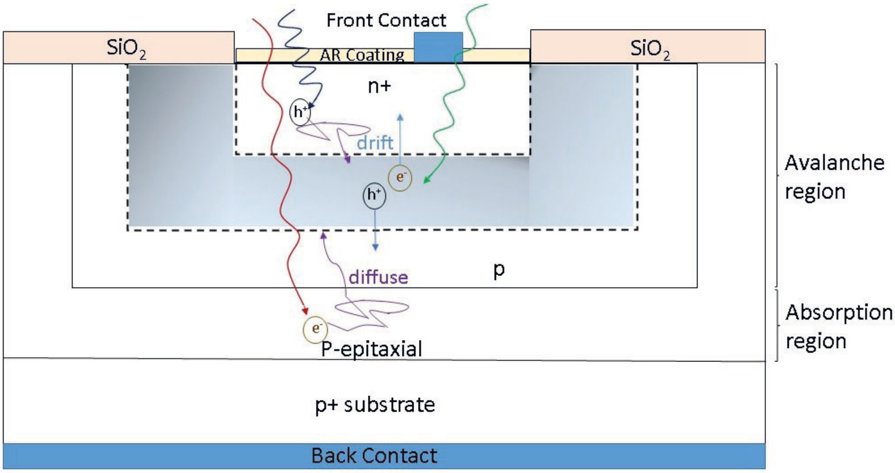

Figure 3.21: Simplified representation of carrier transport for n+/p/p-epi/p+ structure (not to be scaled). SCR is shown as shaded region and both mechanism (Drift and Diffusion) responsible for carrier transport are depicted here.

are dependent on the device structure and its junction capacitance.

Given the electrical model of the SiPM as per Fig. 3.1 the leading edge of the signal, which is a surge of current resulted due to an avalanche and can be characterized by a time constant $\tau_{discharge} \approx R_D(C_D + C_Q)$ [48]. As mentioned earlier, this current will be self-sustaining unless the voltage is dropped across a quench resistor R_Q. The latter is responsible for exponentially ceasing of the signal and its falling edge can be approximated over a load resistor R_L as $\tau_{recharge} \approx R_L(C_{tot} + C_g) + R_D(C_D + C_Q)$ [48], assuming $R_Q \gg R_D \gg R_L$. Where $C_{tot} = C_{Dtot} + C_{Qtot} =$ Number of microcell $(C_D + C_Q)$ and C_g is capacitance due to the metal grid over the diode surface, known as parasitic grid capacitance.

Although in the Geiger mode with the initiation of avalanche, the charge multiplication is limitless, i.e. infinite but quenching mechanism limits this factor to around 10^6 in one avalanche to avoid any damage in the device arising from heat produced due to the high current density. This multiplication factor is called gain (G) and which represents the charge generated by the avalanche process in a SPAD and mathematically represented as [48]

$$G = \frac{Q}{e} = \frac{(C_D + C_Q)(V_{OP} - V_{BD})}{e} \tag{3.5.3}$$

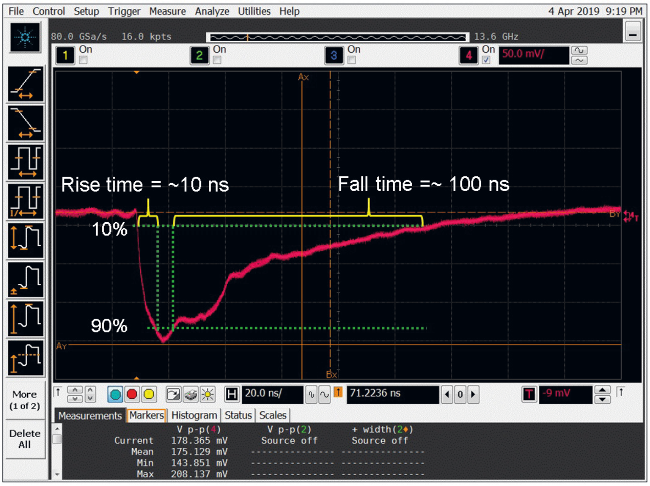

Figure 3.22: A standard output signal recorded with an oscilloscope for an SiPM from *SensL* showing the rise and fall time. Reproduced with permission from [126].

where $V_{OP} - V_{BD}$ (ΔV) is excess voltage, Q is the charge generated in one avalanche event and C_D, C_Q are same as defined before, i.e. diode and junction capacitance respectively. Experimentally it can be calculated by the time integral of the current or analysing single photon spectra. It is clear from the 3.5.3, that the gain depends on ΔV, which in turn implies to its dependency on temperature.

The avalanche multiplication in SPAD is a stochastic process, i.e. for every absorbed photon at a given distance in SCR, not the same amount of EHPs are generated. This means all the carriers traversing the high-field region do not yield the same number of ionization events and this statistical fluctuation of charge multiplication process is termed as excess noise factor (F). It can be calculated as ratio of the mean square of the gain to the square of the mean gain and is mathematically expressed by (3.5.4) [90],

$$F = \frac{\langle G^2 \rangle}{\langle G \rangle^2} = G \left[1 - (1-k) \left(\frac{G-1}{G}^2 \right) \right] \approx kG + 2(1-k) \tag{3.5.4}$$

where carrier ionization ratio $k = \frac{\alpha_p}{\alpha_n}$ and F depends on the types of carrier injected in the depletion region and is a function of electric field across the structure. From above equation it can be concluded that the lower the value of k and G, the better will be F. For SiPM this value lies around 1.

The avalanche trigger can happen through spurious emission of carriers, due to lattice thermal energy, even when the device is kept under dark conditions and contribute as the main noise source of the SiPMs. It is important to be able to separate the charge according to its physical origin. The latter is done through proper characterization and an analysis based on the probability (statistics) that governs each of the two mechanisms. The mean value of this output pulse rate is called dark count rate (DCR) and can be approximated as (3.5.5):

$$DCR = \frac{I_{\text{dark}}}{e \cdot G} \tag{3.5.5}$$

where I_{dark} is the current measured in absence of light. DCR is expressed in terms of kilo counts per second (kcps) and is desired to have as low as possible (few tens kcps/mm^2) in SiPMs. It is primarily created due to the thermally generated EHPs and analogous to reverse current in p-n junction, which is dominated by the generation in the SCR [91] and is well known by Shockley-Read-Hall (SRH) process.

For an indirect semiconductor (for e.g. Si) simultaneous energy and momentum transfer to the lattice vibration, i.e. *phonon* is required to excite an electron to jump to the conduction band. In contrast, carrier transitions occurs via direct band to band recombination in direct semiconductor (for e.g. GaAs). According to SRH theory, there exists localized energy states in the forbidden energy gap, known as generation recombination (GR) centres, in the indirect semiconductor that facilitates the transition of EHPs via carrier capture and emission (see Fig. 3.23) [41]. These GR centres can also be introduced due to the dangling bond creation on the surface, called as *surface states* [41] and may enhance the generation process and EHPs.

In addition to the temperature-assisted process there are also field-assisted processes that can generate the EHPs. Depending on the electric field profile of the device, there might be creation of EHPs due to tunnelling (direct band to band and trap-assisted), and Poole-Frenkel effect (conduction of electricity in insulator) caused by the high electric field [92] at the junction. However, the measurements shows that at room temperature these effect are negligible compared to the SRH thermal generation process [91] and relates the direct dependence of DCR with temperature.

With increase in the ΔV, carrier generation is enhanced together with avalanche initiation probability (refer to sec. 3.5.3) leading to an increase in DCR. It is advisable to limit the

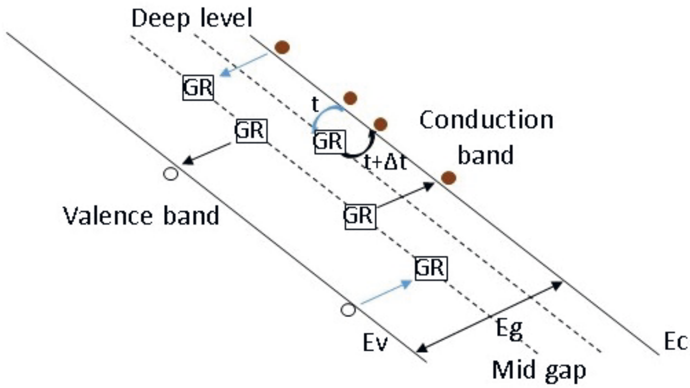

Figure 3.23: Carrier (hole: hollow circle, electron: brown circle) capture (in blue) and emission (in black) process within the generation recombination center created in mid gap ($E_g/2$) and in deep levels. It also depicts the afterpulse phenomenon due to trapping of carrier in deep level and emission with a considerable delay (Δt).

electric field intensity level that suffice the condition for avalanche breakdown, in order to minimize the DCR. This can also be achieved by operating the SiPMs at lower temperatures. Additionally, improved material growth and enhanced device fabrication during production can also reduce the DCR created due to the crystal defects.

The crystal defects such as impurities, dislocations, interstitial atom, vacancies etc. not only generates the GR centres at mid-gap, but also at deep-level. These are intermediate energy levels created in the bandgap, between the mid-gap and band edge [92]. These deep-levels created in the avalanche region act as trapping centers for minority carriers due to the fact that large number of carriers crosses the junction. These trapped carriers depopulate after a significant delay (see Fig. 3.23) and may re-trigger an avalanche process following the actual photogenerated avalanche event, provided the device is biased above V_{BD} [92]. Consequently, the pulse detected can be due to unrelated photon events and is contributed due to the superposition of primary and secondary pulses. The probability of subsequent release of carriers leading to a pulse produced due to false avalanche event is termed as *afterpulse*.

For avoidance of these additional spurious signals, a longer hold-off time can be utilized so that maximum carriers are emptied from the traps. This additional de-trapping time will add to the dead-time and impairs the dynamic range of the device (see Fig 3.6). Cooling the

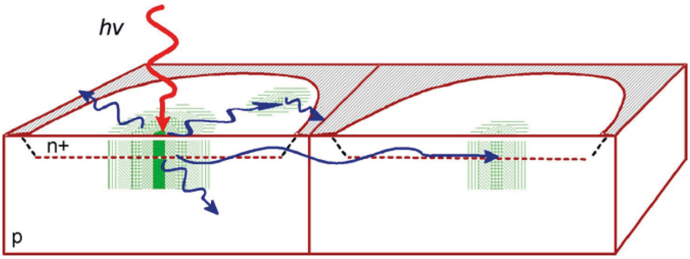

Figure 3.24: Representation of *optical crosstalk* (radiative recombination) and *electrical crosstalk* (lateral diffusion) between two SPADs. Picture taken with permission from [91].

SiPM in this case will have an adverse effect on after-pulse due to exponential increase in the lifetime of the traps [92].

Another significant FOM in SiPM is named *crosstalk*, which is a co-related noise due to the ignition of an avalanche in the neighbouring cell and affect the independence of the SPADs. It is defined as the ratio of detection of secondary photons to the original photon. It can be classified into two categories: *optical*, and *electrical crosstalk* (see Fig. 3.24). Latter is due to lateral diffusion of carriers assisted by avalanche multiplication [93]. Once an avalanche is initiated, few photogenerated carriers diffuse to the adjacent SPADs due to gradient of carrier concentration and trigger a co-related avalanche.

It may happen that carriers generated in the SPAD high field region emit photons through the radiative recombination process [85]. This phenomenon of light emission in avalanche by hot cells is well known [94] and on average 3 photons are emitted per 10^5 generated carriers [95]. This leads to *optical crosstalk* and can induce simultaneous avalanche through direct propagation of photons to the neighboring cells or indirectly by the photons reflecting from the bottom of the device.

An obvious solution to reduce the optical crosstalk will be to maintain the distance between the SPADs, but that will decrease the active area and PDE. Another one is introducing optical barrier structures between neighboring SPADs, filled with optically opaque material and etching the trench structure (guardrings, or using shallow trench isolation (STI)), $\backsim$1 µm thick, between the SPADs again at an expense of lower fill factor (refer to next section). Additionally, electrical isolation of the SPAD´s epitaxial layer with deep diffusion of the same substrate type helps to limit the electrical crosstalk.

3.5.3 Optical Characteristics

Three FOM for the optical performance of an SiPM can be derived under light illumination. These are the most important properties of SiPMs defining its overall performance.

The probability of a SPAD to create an output pulse in response to photon illumination is defined photon detction efficiency (PDE). Experimentally, it can be evaluated as the ratio of the number of incident photons to the number of detected photons. For detecting a photon, light has to impinge onto the active area of the SPAD and get absorbed in the crystal to create an EHP that could onset an avalanche trigger. Thus, PDE is the product of the pixel's fill-factor (FF), its quantum efficiency, and the probability of a generated electron to trigger an avalanche multiplication process, as expressed in (3.5.6):

$$PDE = FF \cdot \eta(\lambda) \cdot P_{\mathrm{T}} \tag{3.5.6}$$

In a SPAD, the whole area is not effective for photon absorption due to electronic circuitry around it (refer to Fig. 3.11). The fraction of the total area occupied by the SPAD is called *fill factor (FF)*, i.e. the ratio of sensitive area to the total area, and merely refers to the geometrical efficiency of the SPAD.

Quantum efficiency is defined as the ratio of the generated EHP to the input light flux, denoted by η and is given by (3.5.7) [96]

$$\eta(\lambda) = (1 - R)\left(1 - \exp^{-\alpha(\lambda)w}\right) \tag{3.5.7}$$

where w is the depletion width, R is the Fresnel reflection coefficient and α is the absorption coefficient. The latter is the inverse of the distance for a photon flux to decay 67 %, as the photon optical absorption in the junction follows the Lambert-Beers law: (3.5.8) [96]

$$I(\lambda, \delta) = I(\lambda) \cdot \exp^{-\alpha(\lambda)\delta} \tag{3.5.8}$$

with δ being the penetration depth. At cut-off wavelength $\lambda_c = \frac{1.24}{E_g}\mathrm{\mu m} = 1100\,\mathrm{nm}$ for Si, α decays rapidly [85]. This sets the fundamental limit of the photon energy, below which no absorption takes place. On the other hand, for shorter wavelength (300 nm) or photon energy above 4 eV they get absorbed near to the surface and do not diffuse to high field region to initiate an avalanche because the top layer is formed by implantation or diffusion process.

It is clear from 3.5.7 that the physical phenomenon of reflection plays an important role due to the air (n=1)/silicon (n=3.5) interface, that can reach up to 30 % according to the Fresnel reflection calculation [97] for the light hitting perpendicularly to the SPAD surface. For circumvention, anti reflecting coatings e.g. MgF_2 (n=1.38) for visible light, Si_3N_4 (n=1.9) and TiO_2 for NIR region, are used to maximize the photon absorption and consequently improve the PDE.

If the photons are absorbed in the active volume and they manage to generate EHPs, then it is also not sure that all of these EHPs traversing through the high field region will trigger an avalanche. The joint probability of electrons and holes passing through the SCR that starts the multiplication until the whole junction is discharged is known as *avalanche triggering probability* P_T.

Besides pair generation position, or the types of carrier injection, it is mainly dependent on the α_n and α_p, which in turn are depending on the electric field intensity shaped by the doping. And this establishes a strong dependence of P_T on the ΔV (excess voltage). Though $\alpha_n > \alpha_p$ as per the model derived in [98], the difference decreases with higher ΔV and both of them take part equally in triggering. A recent study [99] suggests that if the photon generation happens in the p side then α_n will take over the α_p in UV region else opposite is true in IR region for a better avalanche triggering probability. However, there is a lack of unanimity for a given model developed to characterize α_n and α_p, respectively.

In general, it can be concluded that PDE is a function of λ and excess voltage (ΔV), and having an optimized thickness ($\alpha\delta = 1$) of depletion region will lead to higher PDE. For e.g. few microns should be effective for visible light absorption. However, a thicker SCR region will have good PDE but have limitation of noise increase and degradation in the timing resolution.

The uncertainty between actual and measured photon arrival time is defined as *timing resolution* (TR) of SiPM. It is characterized by the temporal response of the SiPM, as the width of the statistical distribution of the delay between photon arrival and the detection of the leading edge of the output pulse. The jitter is usually represented as the FWHM of the distribution shown in Fig. 3.25. In principle, it is the statistical fluctuation in the avalanche and may not have a Gaussian shape due the delayed jitter contributed by the diffusion tails.

It is possible that the photon absorption takes place in the SCR or the neutral region, so the jitter value has both components. For the latter, jitter is contributed by the carriers diffusing from the neutral to the SCR region and building up an avalanche. Hence, its value depends on the energy of the photon and avalanche buildup time or avalanche initiation

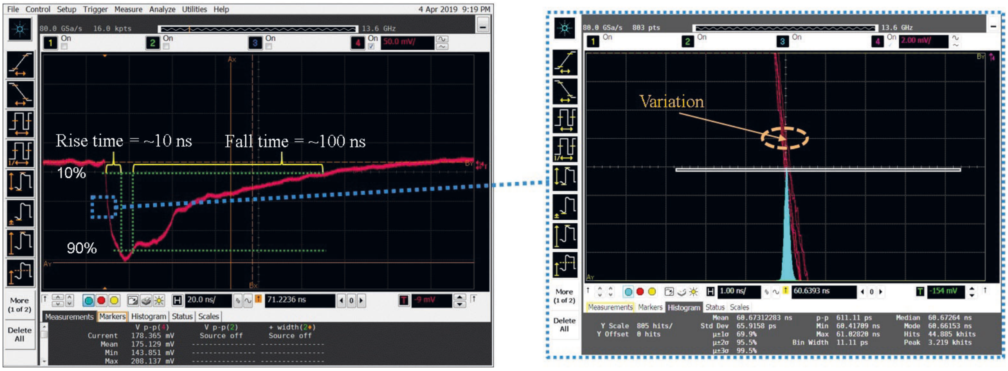

Figure 3.25: Picture showing the temporal characteristics of an SiPM signal along with zoom (on the right) on the variation of its leading edge. The FWHM or sigma of the histogram is referred to as *timing resolution* or *timing jitter* of the SiPM. Reprinted with permission from [126].

probability. Thus it gets better or lower with thinner junction, higher number of photons illuminating the SiPM and higher applied ΔV. Additionally, it turns out to be temperature dependent due to the avalanche process. Because probability of impact ionization event depends on temperature caused by the contribution of *phonon* movement. These movements leads to an increase in the charge carrier generation that causes an increase in the electrostatic potential within the avalanche multiplication volume, which results in an increase in the intrinsic electrical field. So, to induce the electrical field required to trigger the avalanche process a lower bias voltage would be required at higher temperatures.

Another important parameter of the SiPM is its non-linearity. Due to the fact that SiPMs are an array of finite number of SPADs, the output pulse is limited with respect to the incident light. Because once a SPAD detects a photon, it has to reset and go through the quenching process before detecting the subsequent photon. Thus, at photon impinging rates higher than the SPAD dead time (see Fig. 3.6) it starts loosing the photons to be detected due to already busy SPAD. This happens even at lower rates due to the Poisson statistics of the photons and leads to saturation of SPADs and consequently, deviation from linearity in the SiPM response. The deviation can be also be observed, if the number of photons impinging the SPADs are increased. This will result in decrease in PDE. Generally, for the non-linearity correction of SiPM 3.5.9 is utilized assuming a homogeneous distribution of light among the SPADs.

$$N_{firedcells} = N_{cells}\left(1 - \exp^{\left(\frac{-N_{ph}\cdot PDE}{N_{cells}}\right)}\right) \tag{3.5.9}$$

where $N_{firedcells}$ is the number of discharged SPADs, N_{cells} the number of SPADs and N_{ph} is the number of incident photons.

As the process of detection is statistical due to the probability of sensing the randomly distributed photons by a number of SPADs, it set the dynamic range of the SiPM. In general, for avoiding saturation the number of photons should not be more than, as a rule of thumb, one third of the number of SPADs and incident rate should be comparable to the dead time. Another approach could be increasing the number of SPAD, but it will increase the capacitance (C_{tot} and C_g, see sec. 3.5.2) and ultimately affect the TR.

It can be concluded that SiPMs are getting attention for various research as well as industrial applications, which requires detecting extremely low light intensity, down to single photon, with an excellent timing resolution. For designing and fabricating, application specific efficient SiPMs efforts are underway and some of them were mentioned above. Although, there is a lack of unanimity in the SPAD community for the definition of FOM of SiPM and techniques for its characterization, PDE, TR, DCR and co-related noises (cross talk and afterpulse) are considered important. Physical phenomenon behind the FOM were introduced and their inter dependence has been briefly discussed.

Chapter 4

Radiation Damage in Silicon

Radiation detectors may get damaged due to the radiation itself. Radiation damage in silicon is an important mechanism to investigate for the application of SiPMs in harsh radiation environments: neutrons in the present case. Radiation effects depend on the type of particle being detected and associated energy. The damage induced in semiconductors due to various particles has been studied for many years [100–104] and is very well documented by a group at Hamburg University as *Hamburg model* that serves as the base of these investigations. Still, it is considered a complex study given the identification of microscopic phenomena responsible for corresponding effects on macroscopic level caused by the radiation. For a detailed treatment of this topic, the reader is referred to the PhD thesis of M. Moll [105] and the ROSE collaboration (RD48) at CERN [106]. A recent literature on review of the radiation damage in SiPMs due to various particles can be found in [107]. It is useful to understand the basics of the damage induced by different particles in Si, in order to analyse the effect due to the particle of interest, i.e. cold neutrons that will be dealt later on. These are illustrated in the following section and can be classified into two types: *bulk* and *surface damage* (see Fig. 4.1).

4.1 Bulk Damage

Particles traversing silicon can dislodge atoms from the lattice creating crystal defects, depending on the energy and the momentum transferred. This displacement of atoms or primary knock on atom (PKA) is called *displacement damage* or *bulk damage* and is mainly produced by high energy particles (pions, protons, photons, electrons) and neutrons. The damage

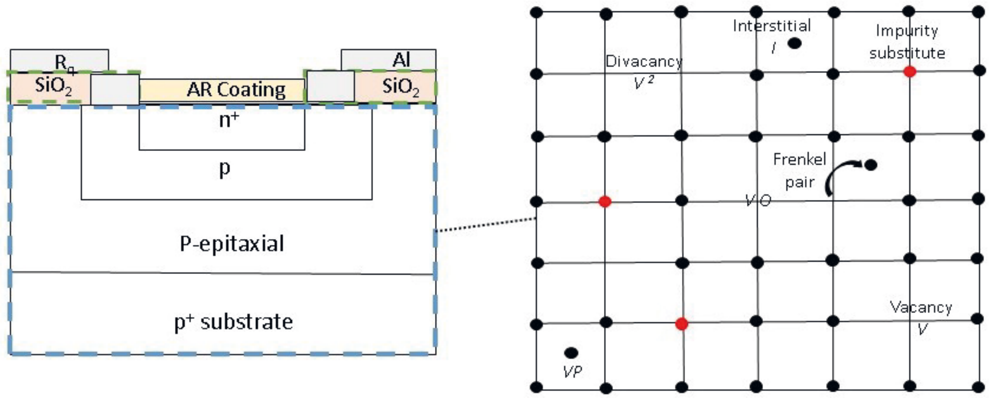

Figure 4.1: Figure showing an example of a possible SiPM structure with the bulk damage region (in blue) and surface damage region (in green). Also shown is a 2D artistic impression of the silicon lattice on the right with few probable defects due to atomic displacements.

is linked to non ionization energy loss (NIEL), i.e. energy lost by the particle that does not go into ionization [108]. According to this hypothesis, the damage effect is proportional to the displacement damage function D, which is defined in terms of MeV/cm^{2}g or MeVmb and normalized with a reference value of 1 MeV neutron equivalent (n_{eq}) = 95 MeVmb, a standard practice in the community to report the damage investigations. The damage manifestation depends only on energy transferred in collisions regardless of particle energy and type and hence, in literature without specific reference to a particle type all fluxes are given as 1 MeV n_{eq}. D accounts for both the energy released in creating displacements and the cross section for displacing silicon atoms. Fig. 4.2 shows the scaling of the bulk damage for a range of particles and energies. Though NIEL scaling is very useful in damage predictions, one has to be cautious in applying NIEL scaling universally, as some deviations from the prediction have been reported [109–111] for protons and electrons.

The recoil energy at which the displacement probability is half is known as displacement energy (E_d) and for silicon it is 25 eV [101]. If the energy exceeds E_d then it may displace a Si atom, creating a *Frenkel pairs* (Vacancy and Interstitial), while lower energy will probably lead to lattice vibration only [101]. For instance a 1 MeV n_{eq} transfers 60 keV to 70 keV to Si leading to around 1,000 atom displacements within 0.1 µm [103]).

The displacement of atoms results in primary and complex defects (see Fig. 4.1). Interstitial I (atoms between regular lattice sites) and Vacancy V (empty lattice sites) are the

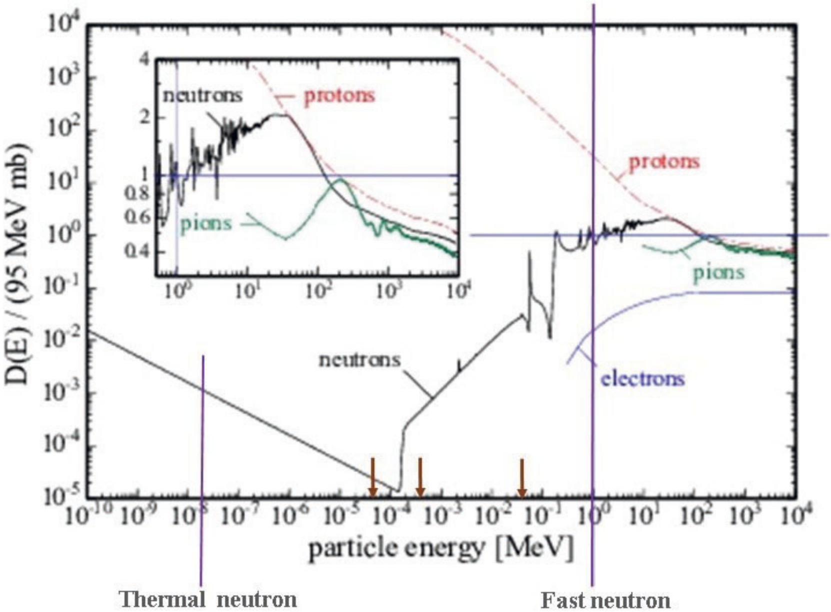

Figure 4.2: Non ionizing energy loss (NIEL) cross section for different particles used commonly as the displacement damage in Si due to the listed particles. D is the displacement damage function normalized for 1 MeV neutron cross section. The thermal and fast neutrons shown serves as guide to eye and not represent the whole range. The brown arrows shown are the neutron threshold energies (25 eV, 175 eV and 35 keV) for *PKA, cluster defect* and *Frenkel pairs* respectively. Picture adapted with permission from [102].

primary defects and play an important role because they are mobile at room temperature. This in turn can form complex defects, e.g. multi Vacancy and multi Interstitial due to diffusion processes. These defects become immobile at room temperature and may be already present in the crystal. This will lead to removal or formation of additional donors (VP) and acceptors (VO). The VO are formed due to combination of V and the oxygen present in the Si and create A-centers. Another stable defect is an E-center formed by the V and dopants used in the n-type Si, i.e. Phosphorous.

Due to its mobility there is a probability of reduction in damage defects due to the recombination of primary defects. Damage may disappear or diffuse out of the surface. For instance, recombination of I and V will return the lattice to its original state. Other defects can combine forming more complex defect clusters, a process that normally takes longer than primary recombination. The latter process is called *reverse annealing* or *anti annealing*, while the beneficial one is called *annealing* and both processes are temperature dependent. In general, bulk damage is partially cured by increasing the temperature for some time.

As the SCR depends on bulk properties, any change in Si bulk will ultimately affect its performance. Therefore, these microscopic changes in the bulk induced by the damage will result in changes in macroscopic properties: *reverse bias current*, *output signal* and *doping density*. These effects will differ depending on the type of detectors and their application. The lattice displacements introduce intermediate states in the bandgap: mid-gap and deep levels (refer to sec. 3.5.2). These states facilitate the transition of carriers generating a current, i.e. an increase in the reverse or leakage current in p-n junction diodes. In addition, carrier trapping also increases as already mentioned in section 3.5.2. Due to the trapping process the carrier lifetime decreases and this leads to reduction in the output signal and in combination with the increased leakage current results in higher electronic shot noise. Another significant change is in the doping density. A higher particle flux ($\backsim 1 \times 10^{13}\,\mathrm{cm}^{-2}$) can lead to *type inversion*, for e.g. under protons exposure the effective doping of an initial n-type Si decreases to intrinsic and then turns to p-type [103].

The defect generation is proportional to the flux. The leakage current I_d is given as a function of the damage coefficient α, which depends on particle type and flux ϕ [103]:

$$I_\mathrm{d}(\alpha) = I_\mathrm{O} + \alpha \cdot \phi \cdot A \cdot d \tag{4.1.1}$$

https://ifftex.fz-juelich.de/project/5f1978f4439c2d32e014ec04 where I_{O} is the current before particle irradiation, A and d are the detector area and thickness respectively. I_{d} increases linearly with flux as found in many experiments [112–114] .

As mentioned earlier in the section 3.5.1, two contributing mechanism towards the leakage current is the diffusion term I_{diff} arising from the minority carrier's movement from the neutral region to the SCR and generation term I_{gen} contributed due to the trap and field assisted process. The latter dominates for the dark current and has the following temperature dependency [107]:

$$I_{\mathrm{gen}} \propto T^2. \left(\exp -\frac{E_{\mathrm{a}}}{kT}\right) \tag{4.1.2}$$

Where E_{a} is activation energy (0.605 eV for irradiated samples [107], whereas for non-irradiated it is half of band gap energy [103]), and k is the Boltzmann constant. At room temperature, usually the dark current decreases by half for approximately every 8°C temperature change [107], a similar trend reported in [9] for DCR.

The trapping of carriers increases with the concentration of trapping centers created by the defects, and consequently the charge collection efficiency degrades. The carrier lifetime is given by (4.1.3) [103],

$$\frac{1}{\tau} = \frac{1}{\tau_i} + \frac{\phi}{k} \tag{4.1.3}$$

where τ_i is initial lifetime and k is trapping constant. As the damage term prevails after low flux, so it can be assumed that

$$\tau \approx \frac{k}{\phi}$$

and the life time will decrease with higher flux. As the net signal charge is proportional to $\exp(-t_c/\tau)$ [103] for a given thickness of sensor and collection time t_c, change in flux from 10^{14} to 10^{15} will lead to one order magnitude decrease in lifetime and substantial charge loss, as well as an adverse effect on the charge collection and signal.

Irradiating n-type Si with high particle flux will lead to a change in doping density. This is due to the creation of effective donor or effective acceptor defects assuming positive or negative charge state in the SCR, or capture of original donors and acceptors by formation of complex defects (e.g. VP, VO/VB). This effective doping concentration N_{eff} depends on the

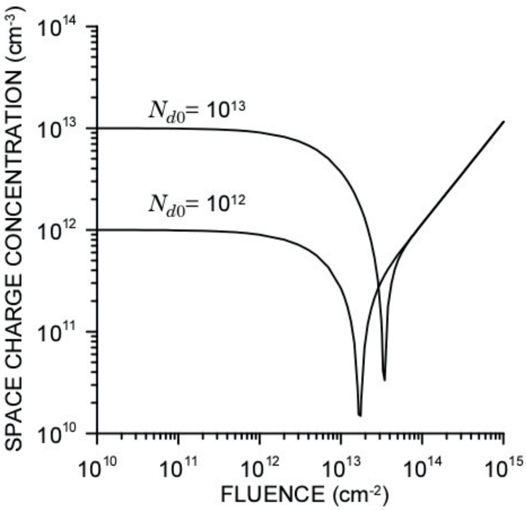

Figure 4.3: Calculated space charge or effective doping (N_{eff}) vs. high-energy proton flux for n-type silicon with initial donor concentrations (N_{do}) of 10^{12} and 10^{13} cm-3. Picture taken with permission from [103].

flux and can result in *type inversion*. As shown in Fig. 4.3, an effective doping for an n-type Si with high energy proton flux changes the positive charge state in SCR, by neutralizing original donor states with new acceptor states, and becomes neutral at the flux of $1 \times 10^{13}\,\mathrm{cm}^{-2}$, then turns negative and increases proportionally with the flux due to domination of acceptor defects caused by displacement damage. It has to be noted that due to the *type inversion* it appears to be a p-type Si. But in reality it differs from the conventional p doped Si due to its electrically inactive nature, as inversion is not only associated with the creation of mobile holes, but the acceptor states [103]. However, this mechanism induces a change in the SCR and consequently affects the operating voltage as well. In [107], it has been mentioned that the breakdown voltage shift due to irradiation will have some dependence on the width of the multiplication region.

It has been observed that after the irradiation of the detector, the damage effect diminishes by itself after some time. This process is called *self annealing* and strongly depends on the temperature environment. It is related to the disappearance of defects. Different particles lead to different optimal temperature treatments that cannot be generalized due to the complex mechanisms playing the role behind it and there is no general optimal annealing temperature. For 1 MeV n_{eq}, it has been observed that heating the device to 60°C for 80 minutes can reduce the damage coefficient to $\alpha = 4 \times 10^{-17}\,\mathrm{A\,cm^{-1}}$ from $6 \times 10^{-17}\,\mathrm{A\,cm^{-1}}$ [105] [115] and improve the charge collective efficiency.

The detailed mechanism behind the annealing is not very well understood but it can be estimated that besides short term beneficial annealing at certain stage the primary defects that were helping the damage recovery start forming second order stable defects, which in turn lead to long term defects, a process known as *reverse annealing* [103].

In summary, to analyze the bulk damage defects and its impact on the parameters, defect types (point or clusters), energy levels created by defects, leakage current, space charge region, trapping and defect development with time needed to be studied in detail.

4.2 Surface Damage

The radiation induced damage in the oxide (SiO_2) and surface interface ($Si - SiO_2$) is called surface damage. It is primarily caused by charged particles, x-rays and photons (below 300 keV), introduced by ionization energy loss (IEL) and not by atomic displacement [107]. The damage is due to induced charges in the oxide and surface interface, and interface traps [101].

The oxide region is highly irregular in contrast to the single crystal of the semiconductor. This results in lattice mismatch and dangling bonds, which lead to a very high concentration of already present defects at the interface compared to ones introduced by irradiation. Since the bandgaps of SiO_2 (8.8 eV) and Si_3N_4 (5 eV) are very high, the generated carriers are trapped in these defects, due to very low chances of emission. The trapping of holes is more likely than that of electrons, because the mobility of electrons in oxide is several orders of magnitude higher than the hole mobility, allowing them to leave the oxide [103]. This in turn changes the oxides' material properties caused by positive charge states and interface traps.

The creation of high field strengths contributes to the surface current part in the dark current. Altogether, surface damage can deteriorate sensor performance by affecting the field inside the device and by increasing the noise due to the capacitance increase [104].

One can safely conclude that above a dose of $1 \times 10^9\,\mathrm{n_{eq}/cm^2}$, major problems associated with radiation are loss of signal, high leakage current and doping density change. Radiation not only changes the electrical properties of the semiconductor, but also of an insulator. Thus, in order to have a radiation hard device, it is advisable to design a device which can either tolerate the radiation induced effects by not changing its characteristics or can maintain its performance even after the introduction of the radiation induced changes. The latter is a more practical approach and has achieved some significant results [115].

There are groups actively researching device and defect engineering, using the standard radiation measurement techniques such as deep-level transient spectroscopy (DLTS) and thermally stimulated current (TSC). The most prominent work is ongoing within the framework of the international RD50 collaboration at CERN [116], whose task is to search for radiation hard Si devices for high energy physics. Besides different growth techniques of substrates with different diffusing atoms (e.g. carbonated, oxygenated), cooling and thermal annealing could be beneficial to circumvent the damages. Additionally, different materials, e.g. GaN and SiC, are also being investigated.

It has been experimentally found that DLTS and TSC are not applicable in SiPM due to large capacitance and high dopant concentration [107]. Given the dopant concentration of $\backsim 1 \times 10^{16}\,\mathrm{cm}^{-3}$ DLTS sensitivity limit for trap concentration is $\backsim 1 \times 10^{12}\,\mathrm{cm}^{-3}$, which is much higher than the expected traps produced due to the radiation. While, as mentioned in [107] very small depleted volume might be the reason for TSC limitation.

4.3 Neutron Radiation Damage to SiPM

Different groups have investigated SiPM performance under neutron irradiation with flux up to $1 \times 10^{14}\,\mathrm{n/cm}^2$ [117,118] and found that SiPMs were operable with significant performance degradation. Moreover, numerous groups have exposed SiPMs to fast neutrons (i.e. 1 MeV) and have investigated the damage caused [112–114, 119, 120]. The results show a significant increase in dark current and loss in signal amplitude. Other parameters such as PDE, G, C_D and V_{BD} do not show any significant changes. These changes depend on the integrated dose, neutron energy and employed SiPM technology. However, to the best of the author's knowledge, no study besides our group has been performed with cold/thermal neutrons, that are utilized in SANS.

The significance of this work arises due to the difference in the energy of neutrons, which translates into different damaging effects. For instance, the threshold energy for creation of cluster defects (35 keV), Frenkel pairs (175 eV) and PKA (25 eV) [102] are higher than the energy of cold or thermal neutrons (several meV). Additionally, as per the energy dependent damage scale shown in Fig. 4.2, it can be expected that the damage caused by cold and thermal neutrons would be three orders of magnitude lower than damage caused by fast neutrons. Therefore, an investigation of the dark current dependency on cold neutron irradiation has been performed, and within the scope of this work the characterization for PDE and TR are carried out.

4.3.1 Evaluation of DCR

In 2015 [9] all three mentioned SiPMs arrays, i.e. *Philips*, *SensL* and *Hamamatsu* were irradiated with neutrons of 5 Å wavelength up to a flux of $1 \times 10^{12}\,\mathrm{n/cm^2}$ at KWS-1 instrument (flux of $1 \times 10^{8}\,\mathrm{n/cm^2/s}$) [8] available at the research reactor FRM-II in Garching, Germany. During the irradiation SiPMs were constantly biased at the recommended excess voltage (ΔV) of 2.5 V and 2.4 V for *SensL* and *Hamamatsu*, respectively. For the digital SiPM (PDPC) 3 V was set in the digital evaluation kit provided by the manufacturer.

The results of the investigation [9] show a significant increase in the dark current for the total doses onto the SiPMs ($1.9 \times 10^{12}\,\mathrm{n/cm^2}$ for SensL, $6 \times 10^{12}\,\mathrm{n/cm^2}$ for Hamamatsu and $1.9 \times 10^{12}\,\mathrm{n/cm^2}$ for Philips). Two mechanisms are responsible for this: increase in electron concentration and creation of point defects.

The neutron transmutation doping (NTD) initiated by capturing thermal neutrons was used for uniform doping with Phosphorous in Si [121] in the 1950s. The nuclear reaction for the doping process follows (4.3.1) [122]:

$$^{30}\mathrm{Si}\,(\mathrm{n},\gamma) \longrightarrow {}^{30}\mathrm{Si} \longrightarrow {}^{31}\mathrm{P} + \beta^{-} \tag{4.3.1}$$

The thermal neutrons' interaction with Si results in a change of effective doping concentration (N_{eff}) and an increase of donor density due to additional Phosphorous donors, which in turn decrease the carrier lifetime of minority holes, i.e. the same term τ responsible for the bulk damage. Another effect observed experimentally is creation of 3 to 5 point defects (e.g. A-center, E-center, Divacancy) in Si per absorbed thermal neutron [122]. These electrically active defects act as the GR center and are the dominating effect that increases the I_{gen}, the ones responsible for the increase in dark current. However, as it can be observed from the second row in Table 4.1, the increase in dark current is not large after the expected total dose accumulated in a typical SANS experiment for 10 years. The DCR increase is well within the limit (see Fig. 4.4) and does not affect the performance of SiPM, given the maximum allowed

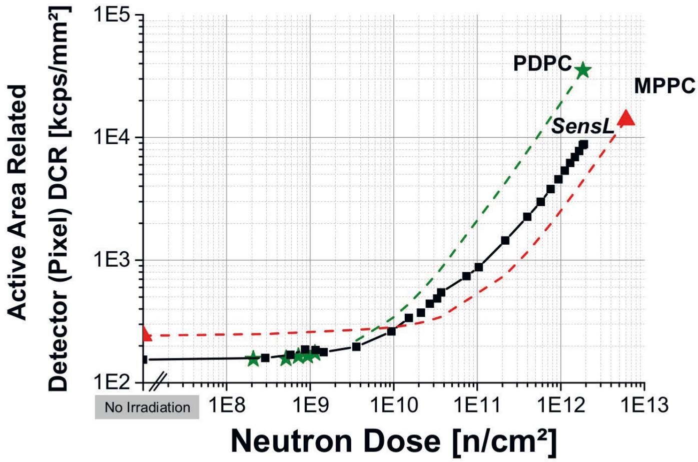

Figure 4.4: The neutron irradiation dose dependent DCR curve for *Philips* (PDPC), *Sensl* and *Hamamatsu (MPPC)* SiPMs at 23°C. Reprinted with permission from [9].

DCR of 280 Mcps as calculated in [9]. This result is valid under the consideration of main neutron beam blockage at the center by a beam stopper (for details refer to [9]). Moreover, Table. 4.2 shows direct irradiation of SiPMs covered by a ^{6}Li-glass scintillator (GS20) and placed in front of the neutron beam without any beam stopper. The increase in DCR (a factor of ∽4) is nominal due to the absorption (∽95 %) of neutrons in the scintillator. GS20 is also employed within this work for the development of the neutron detector.

Table 4.1: Neutron (3.27 meV) dose dependent dark current (nA) and DCR (Mcps/mm^2) for the *Sensl*, *Hamamatsu* and *Philips* (PDPC) SiPM evaluated at 23°C. The highlighted dose is total expected dose in 10 years for a typical SANS experiment. Whereas the values in third and fourth row correspond to direct irradiation with neutrons. Data adapted from [9].

Neutron Dose	SensL		Hamamatsu		Philips
(10^{10} n/cm^2)	Dark current	DCR	Dark current	DCR	DCR
0	667	1.4	625	2.4	1.7
3.5	2400	5	897	3.1	11.5
190	38000	81.7	12000	46.5	586
600	-	-	36000	140	-

Table 4.2: Neutron (3.27 meV) dose dependent dark current (nA) and DCR (Mcps/mm^2) for the *Sensl*, *Hamamatsu* and *Philips* (PDPC) SiPM evaluated at 23°C. The highlighted dose is with a ^{6}Li scintillator placed in front of the detector before irradiating with neutron beam, a similar setup present in this work. Data adapted from [9].

Neutron Dose	SensL		Hamamatsu		Philips
(10^{10} n/cm^2)	Dark current	DCR	Dark current	DCR	DCR
0	667	1.4	625	2.4	1.7
400	2900	6.2	2200	8.5	-

4.3.2 Characterization of PDE

In order to quantify the change in PDE caused by thermal neutron irradiation, a measurement system was developed and characterized to evaluate the wavelength dependent PDE of the above mentioned same irradiated SiPMs. The system consists of a Xenon arc lamp, a monochromator (200 nm to 1200 nm), lock-in and pre-amplifiers and a data acquisition module (see Fig. 4.5). This enables to evaluate the breakdown voltage (V_{BD}) using the I-V curve method (refer to sec. 3.5.1) and plot the PDE of SiPMs utilizing a reference photo diode. For details of the system and the method employed, the reader is referred to [10].

The reference diode was used to count the number of photons illuminating the SiPM for a given light wavelength and then the photodiode was replaced by the SiPM to evaluate its response. The ratio of the responses was calculated as the PDE at that wavelength. The result of the study [10] shows a relative reduction in the PDE at 420 nm of approximately 11.3 % for *Hamamatsu*, 5.2 % for *SensL* and 3.8 % for *Philips* (PDPC). One possible reason could be that due to increased DCR caused by the irradiation translates into lower availability of SPADs for the photon detection due to higher occupancy. Additionally, although it depends on the structure of the SPAD, the contribution in the photocurrent from the carrier generated outside of the avalanche region might got reduced due to diminished carrier life time resulted from the irradiation, which in turn affects the PDE.

The difference in PDE of non-irradiated and irradiated PDPC is not monotonous as seen in the curves plotted for the non-irradiated and irradiated SiPM (see Fig. 4.6). This is attributed to the change over short wavelengths due to the Fabry-Perot interferometer (FPI) or etalon effect (constructive or destructive interference caused by multiple reflection) arising at Oxide and Nitride interface. Nevertheless, considering the measurement certainty of up to 16 % and maximum decrease in PDE (11 %) for a dose two orders of magnitude higher than the expected 10 years operation, i.e. 10^{10} n/cm^2, it is safely concluded [10] that SiPM

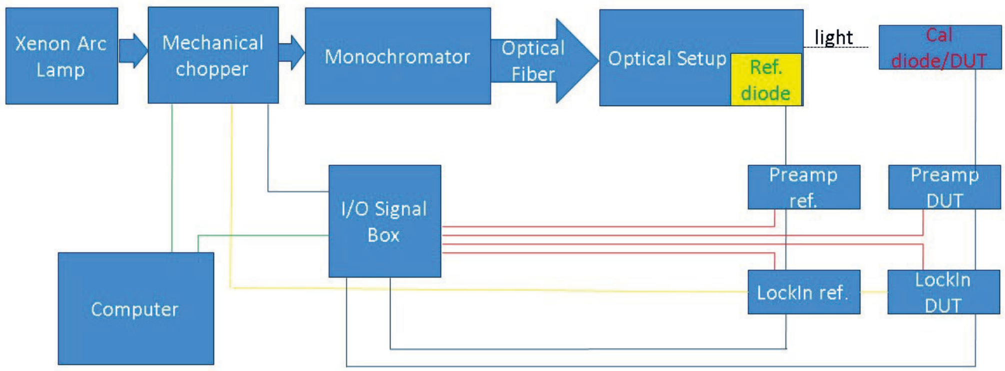

Figure 4.5: Diagram of the measurement set up employed for the evaluation of wavelength dependent PDE for given SiPMs. Picture reproduced with permission from [10].

technologies are feasible for SANS application without significant performance degradation in PDE over a detector's lifespan.

4.3.3 Effect on Timing Resolution

For the assessment of the SiPMs' applicability in TOF scattering experiments that also uses cold or thermal neutrons, an investigation of the changes in TR after irradiation has been performed. Due to the advantages associated with SiPMs (see Table 2.3), its TR is well within a few tens of ps [123]. This can be helpful to improve the existing TOF detector which has TR in sub ns range [124, 125].

For this purpose a measurement system was developed and characterized to measure and compare the TR of irradiated and non-irradiated analog SiPMs. As shown in Fig. 4.7, the main components of the system were a pulsed diode laser, an oscilloscope and further optical components. The details can be found in [126]. The methodology employed was to compare the time jitter of the SiPM output signal with a reference signal from that laser, synchronous to the optical pulse. Each laser pulse contained a few hundred photons.

A picosecond pulsed laser (405 nm wavelength) with a pulse width of 45 ps was employed as the light source. The laser was operated at a repetition rate of 1 MHz. For the signal analysis a fast digital oscilloscope (sampling rate of 40 GS/s and bandwidth of 13 GHz) was used.

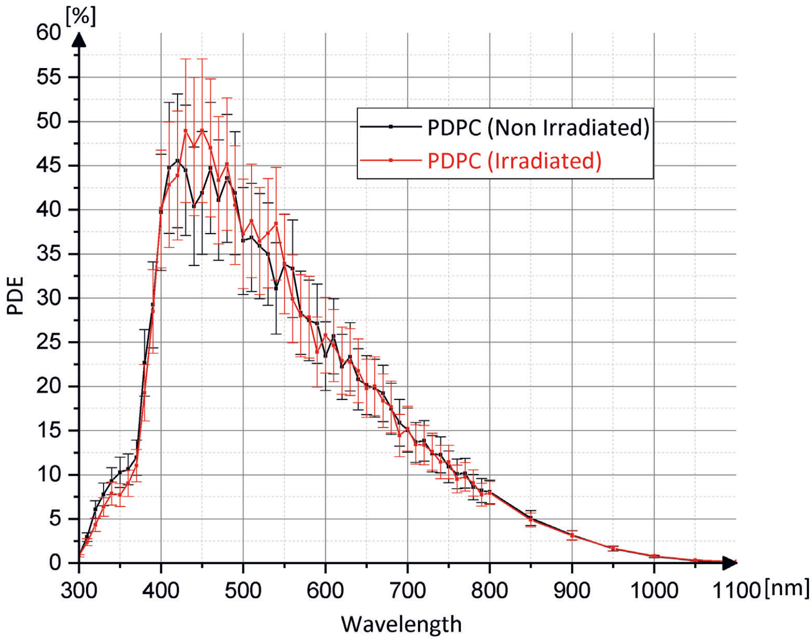

Figure 4.6: Graph showing the *photon detection efficiency (PDE)* measurement of irradiated (dose = $1.9 \times 10^{12}\,\mathrm{n/cm^2}$) and non-irradiated sensors from *Philips* (PDPC). The measurements were performed at 21°C. Picture reproduced with permission from [10].

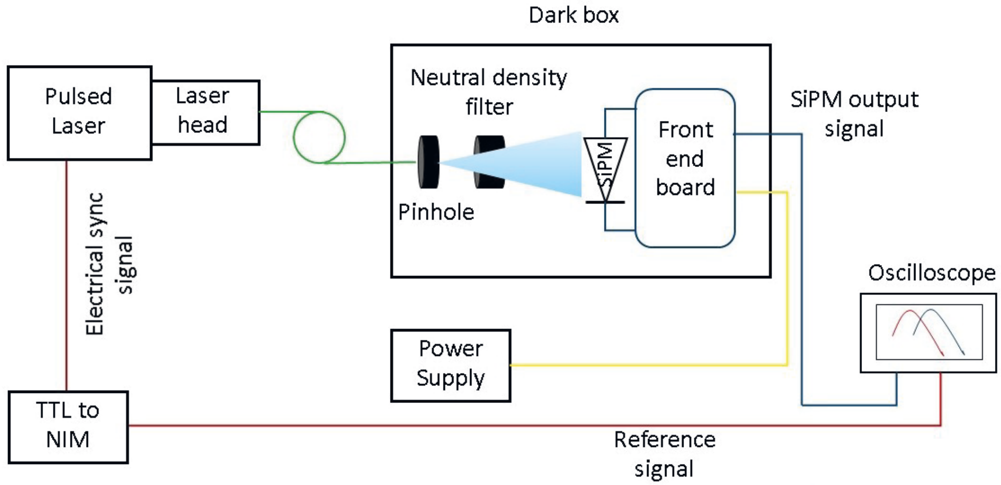

Figure 4.7: Schematic of the measurement system developed and characterized for the timing resolution (TR) calculation of *SensL* and *Hamamatsu* SiPMs. Reproduced with permission from [126].

The SiPM signal is generated by illuminating with the laser beam and as mentioned the laser trigger output was used as the reference signal. The temporal characteristics of these two signal were measured and plotted in a histogram by the oscilloscope (see Fig. 3.25). Further, the standard deviation σ of this histogram is calculated to evaluate the TR of the SiPM. During the measurements, the SiPMs have been maintained at a constant temperature (21±0.5°C) in dark environment.

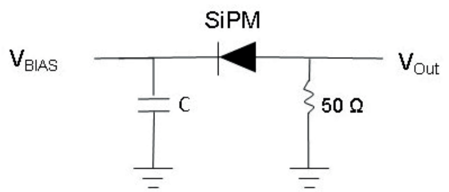

Figure 4.8: Circuit diagram for the SiPM read out. Where C is a decoupling capacitor of 10 nF for *SensL* and 0.1 µF for *Hamamatsu*.

The response of the SiPM was obtained from the standard read out circuitry recommended by the manufacturers. For both *SensL* and *Hamamatsu* arrays, a load resistor of 50 Ω was used along with a decoupling capacitor of 10 nF and 0.1 µF respectively (see Fig. 4.8). Furthermore, a constant threshold at 50 % of the signal amplitude was set during the measurements. The biasing of the SiPM was provided by a programmable power supply (*EA-PSI-6150-01*) with a resolution of 10 mV.

The values of the breakdown voltage for non-irradiated and irradiated SiPMs (∽25 V for *SensL* and ∽65 V for *Hamamatsu*) were taken from the past measurement [10] at the given temperature, which were obtained from the I-V curve method (refer to sec. 3.5.1). Different biasing voltages were applied during the experiment to achieve the range (2 V to 6 V) of excess voltage ΔV.

The trigger output pulse of the laser represents a 5 V TTL (transistor-transistor logic) signal, and for signal reconditioning we converted it into a −1 V NIM (nuclear instrumentation module) signal, using a NIM-TTL-NIM adapter (*EG&G, LA8000*). The pulse width of the trigger signal was measured to be 9 ns and the rise time was 4 ns, which was reduced to 3 ns after reshaping in the adapter. This reference signal was used to trigger the oscilloscope on one channel and the SiPM output signal was fed into another channel. The trigger threshold was kept constant at 50 % for all measurements.

The measured jitter value ($\sigma_{measured}$) includes two more contributions in addition to the time jitter of the SiPM (σ_{SiPM}). The first component (σ_{noise}) is the jitter produced by the associated electronics and can be evaluated as the ratio of the sigma of the baseline noise and the slope of the rising edge of the signal [127]. The second component is the overall contribution due to the setup (σ_{setup}), e.g. due to laser trigger output and TTL to NIM adapter. For estimating this, the electronic signal output from the laser via the adapter was split into two channels. Then we employed the same principle of triggering the oscilloscope on one channel and measuring the standard deviation of the histogram obtained from the other channel (see Fig. 4.9). Furthermore, the jitter in the optical pulse width of the laser should also be taken into account and have been obtained from the data sheet (3 ps). Thus, the measured value can be written as the quadrature sum of all the individual contributions as (4.3.2):

$$\sigma^2_{measured} = \sigma^2_{SiPM} + \sigma^2_{setup} + \sigma^2_{noise} \tag{4.3.2}$$

Moreover, σ_{SiPM} can be divided into the intrinsic jitter of an SiPM and the transit time spread that is defined as the timing skew of the SPAD arising from distance mismatch between individual SPADs and SiPM output node [128]. However, this was out of the scope of the study as the goal was not to find the absolute value of the σ_{SiPM}, but to calculate the relative comparison of TR for the irradiated and non-irradiated SiPMs. Therefore, the values of $\sigma_{measured}$ were reported only, consisting of all individual components along with

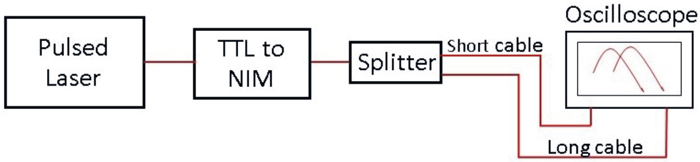

Figure 4.9: Schematic of the measurement system for the evaluation of timing jitter of the setup.

σ_{SiPM} as per (4.3.2). Nevertheless, σ_{noise} and σ_{setup} were calculated to ensure that they do not dominate. For the sake of ease of measurements we assumed them to be constant, since the same experimental conditions and equipment have been used at all times during this experiment. This implies that for all the measurements, we can assume that comparing $\sigma_{measured}$ is equivalent to comparing σ_{SiPM}. The results for the same are plotted in Figs. 4.10 and 4.11.

The outcome of the investigation for the same irradiated (dose up to $6 \times 10^{12}\,\mathrm{n/cm^2}$) SiPM suggests that there is no significant difference (1 ps for *SensL* and 6 ps for *Hamamatsu*) at $\Delta V = 3\,\mathrm{V}$ in the timing resolution before and after irradiation with cold neutrons. The slight increase of performance degradation in TR may be due to the following factors: dark current, point defects and inter-SPAD capacitance.

As the total current is the summation of the photon generated current and dark current, the increased contribution of the latter due to the radiation introduces more randomness in the signal leading to an increase in jitter. Additionally, as mentioned before the point defects introduced by thermal neutrons absorption act as the trapping centers resulting in delayed release of the carriers and affecting the precision of the signal. Furthermore, the trapping centers leads to higher capacitive coupling between the SPADs, thus resulting in higher charge collection sharing between SPADs and a small increase in the noise level. Therefore, an increase in the TR was observed after the irradiation.

Another observation can be made from Figs. 4.10 and 4.11: an increase of performance in TR for both irradiated and non-irradiated SiPMs with increase in excess volatge ΔV, which was also reported before [129, 130]. This is mainly due to reduced jitter in the avalanche generation at SPAD level caused by enhanced impact ionization mechanism at higher ΔV, leading to a faster signal generation and improved time resolution (refer to sec. 3.5.3). However, this improvement is limited due to dominance of increased dark current contribution at higher ΔV over the photon generated current, a similar effect caused by neutron irradiation.

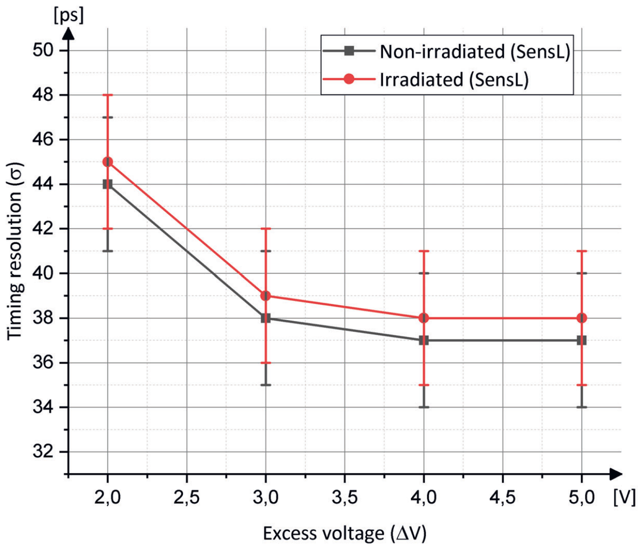

Figure 4.10: Timing resolution comparison of irradiated and non-irradiated *SensL* SiPM, performed at 21°C for approximately 600 photons per pulse and at a constant signal threshold of 50 %. The error bars represent the standard deviation of systematic and statistical error. Reprinted with permission from [126].

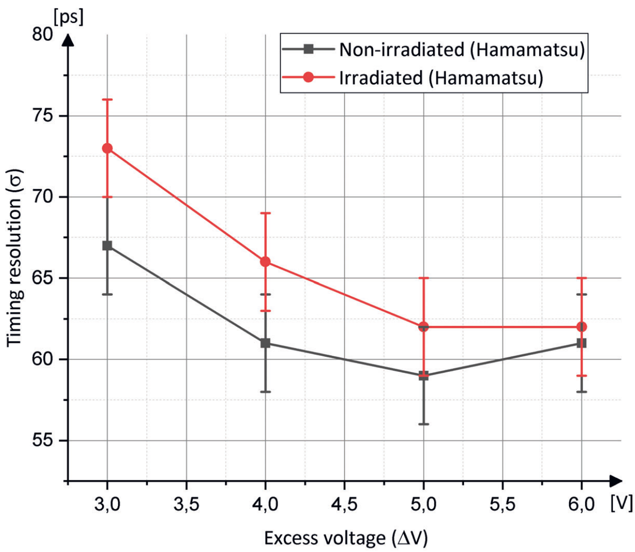

Figure 4.11: Timing resolution comparison of irradiated and non-irradiated *Hamamatsu* SiPM, performed at 21°C for approximately 600 photons per pulse and at a constant signal threshold of 50 %. The error bars represent the standard deviation of systematic and statistical error. Reprinted with permission from [126].

Table 4.3: Results of the investigations for the DCR, PDE and TR changes of *SensL*, *Hamamatsu* and *Philips* SiPM directly irradiated with cold neutrons (3.27 meV). Data adapted from [9,10,126].

Item	SensL	Hamamatsu	Philips
Total neutron dose (10^{12} n/cm^2)	1.9	6	1.9
Increase in DCR factor	58	58	344
Relative change in DCR	57 %	57 %	334 %
Decrease in PDE at 420 nm	1.8 %	5 %	1.7 %
Relative change in PDE at 420 nm	5.2 %	11.3 %	3.8 %
Increase in TR at $\Delta V = 3$ V	1 ps	6 ps	-
Relative change in TR at $\Delta V = 3$ V	2.6 %	8.9 %	-

We should keep in mind that the same samples were used to obtain the results for PDE and TR, irradiated during the DCR campaign (in 2015) and might have recovered somewhat due to self-annealing as they were kept at room temperature. However, the standard procedure of annealing, recommended by radiation community, for 60 min at 80 °C after the irradiation campaign was not performed. Moreover, it will be interesting to quantify these effects under thermal annealing as reported in some investigations [131–134], which reached recovery rates up to 50 % in DCR and almost 100 % in signal amplitude for 10^9 n_{eq}/cm^2. Nevertheless, as summarized in Table 4.3 and from Table 4.1 it can be concluded that SiPM technologies are feasible for neutron scattering, e.g. SANS and TOF applications.

Chapter 5

Detector Prototype

Motivated by the aforementioned findings, a detector prototype with an active area of 13.6 cm × 13.6 cm was built using the GS20 scintillator glass [17] together with the PDPC array [82]. The design focus was kept on three parts of the detector: optical front-end, readout electronics and cooling system (see Fig. 5.1). The latter is required to keep the temperature dependent performance of the SiPM array (PDPC) relatively constant by maintaining the temperature at about 21°C. It consists of two Peltier elements, an Aluminum heat sink and a fan. The whole detector system and its interface is shown in Fig. 5.2.

The readout of the detector employs the built-in data acquisition of the PDPC sensors connected with a printed circuit board (for data transmission and power supply to the sensor) through which data are forwarded to a concentrator board (FPGA based data sorting and processing) via HDMI cables and further to a computer via USB 3.0 interface (300 MB/s) for storage and reconstruction (see Fig. 5.3). The maximum event data rate for each *tile* (total 16 *tile* in the whole detector) of the sensor is ∽20 MB/s and the output is the number of photons detected per pixel along with the timestamp and temperature. The details of the readout system are similar to the work reported in [135].

The optical front-end consists of four PDPC *modules*, i.e. 1024 pixels (SiPMs), a light guide and a 1 mm thick monolithic GS20 glass. Additionally, a light tight Al cap was used to prevent any stray light hitting the PDPC.

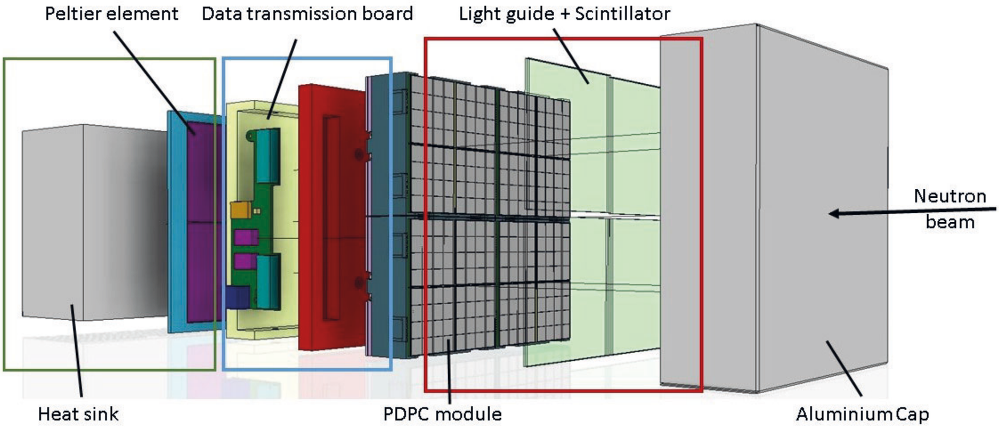

Figure 5.1: Expanded view of the detector. The main assemblies of the detector are: cooling system (in green block), read out electronics (in blue) and optical front-end (in red).

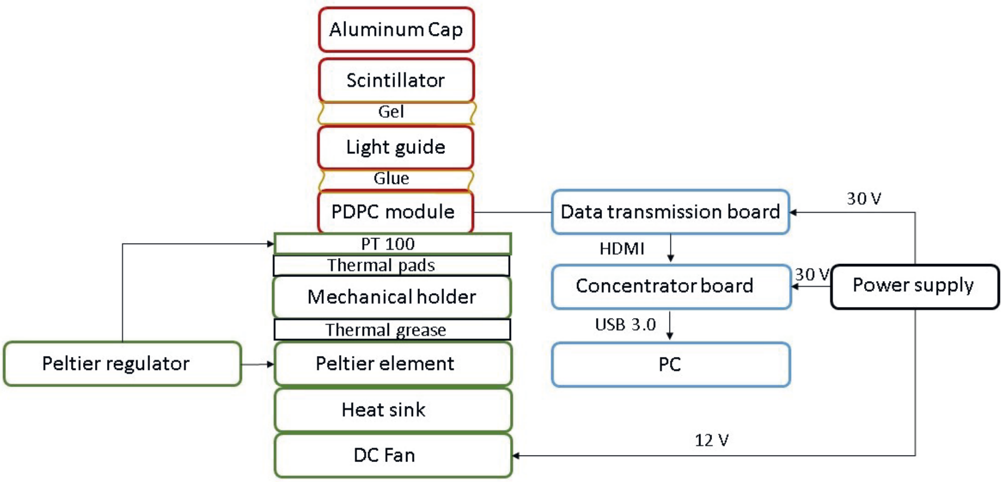

Figure 5.2: Representation of the system interface of the detector prototype. Blocks in red represent the optical front-end, cooling system in green and blue blocks depict the readout electronics.

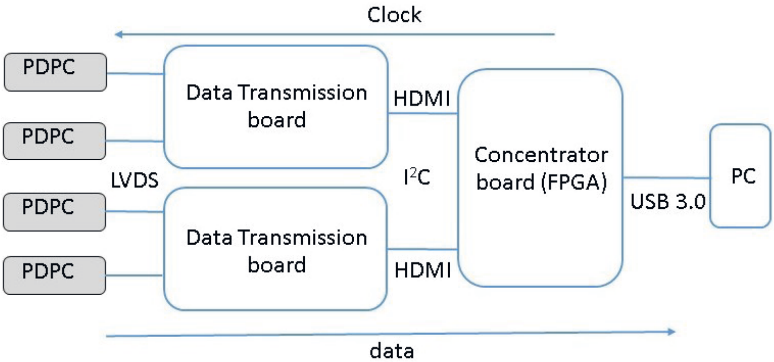

Figure 5.3: Diagram of the employed readout electronics and data transferring through PDPC, data transmission board, concentrator board and finally to the PC. The details of the read out mechanism can be found in [135].

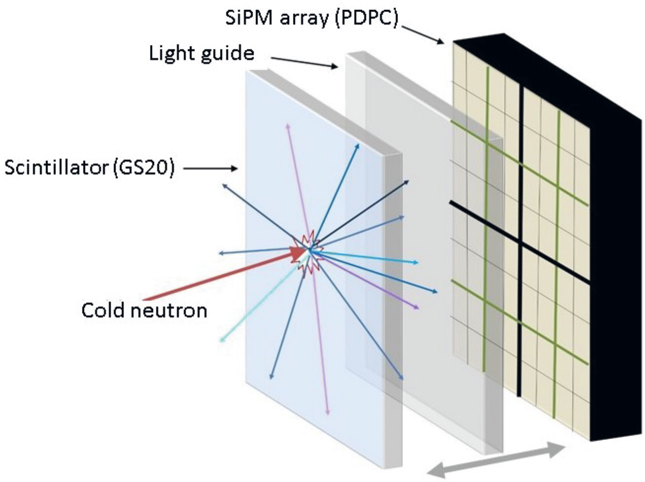

Figure 5.4: Representation of the front-end of the detector showing the light guide, and the capture of a neutron, producing isotropic scintillation light (300 nm to 500 nm) which is detected by the PDPC sensor array. Reprinted with permission from [152].

Table 5.1: The target specification of the detector for cold neutron (5 Å).

Detection efficiency	Count rate	Spatial resolution
75 %	20 Mcps/m^2	1 mm

5.1 Simulation

The target specifications for the development of the detector is listed in Table 5.1. Due to the PDPC pixel pitch of 4 mm the spatial resolution of 1 mm can only be achieved by interpolating the neutron position from multiple pixel counts. For each neutron event, the system provides four pixel counts corresponding to the event. In order to accomplish the targeted resolution, a light guide was introduced between the PDPC and the GS20 to spread the light across several pixels, which improves the reconstruction results. For this purpose intensive simulations of the optical front-end interfaces were performed in order to find the optimal thickness and refractive index of the light guide (see Fig. 5.4). Additionally, the simulation data were used for the reconstruction algorithm itself, which is based on the comparison of simulation data and experimental data.

5.1.1 Geant4

The simulation tool-kit employed was Geant4 (GEoemetry ANd Tracking) [136], developed under a worldwide collaboration of physicists and software engineers and maintained by CERN, which is a widespread tool in particle physics research. Geant4 is a Monte Carlo method [1] [137] based simulation software for passage of particles through matter. The package provides a complete range of functionality including geometry and materials, particle interaction, physics models, and tracking management. Due to its ability to simulate a variety of particles such as leptons, hadrons, neutrinos, and photons, and relevant processes of their interaction with detector components, it is also used for applications in nuclear physics, space engineering and medical science.

The version used in this work is `Geant4_v10.4` [138], which utilizes the object oriented programming feature of `C++` to handle the interaction of a wide energy range (few eV to TeV) of particles traversing through matter.

[1] method for solving deterministic problems using randomness

Table 5.2: Composition of the GS20 (Ce activated scintillator glass enriched with ^{6}Li to 95%) [17], considered for the Geant4 simulation model.

Compounds	Li_20	Al_2O_3	MgO	Si_2O_3	Ce_2O_3
Mass composition	0.157	0.603	0.169	0.034	0.037

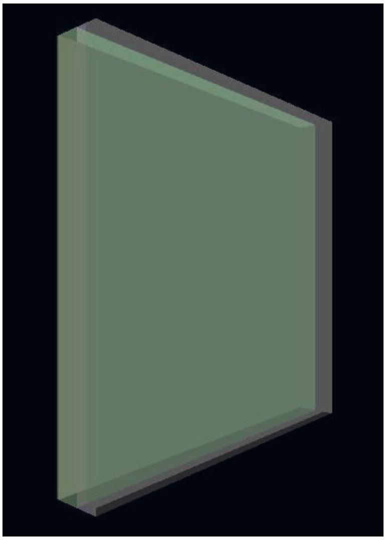

Figure 5.5: Picture of the optical front-end model implemented in Geant4, showing the slabs of glass and silicon. Reproduced with permission from [151].

The detector was modeled according to Fig. 5.5. It consists of slabs of glass and Silicon representing the scintillator, the light guide, and PDPC sensors respectively. The scintillator thickness was 1 mm and its relative composition for the consideration of simulation is given in Table 5.2. The interfaces between the light guide and the scintillator and the light guide with PDPC were also considered and simulated as gel (refractive index (RI): 1.47, thickness: 300 µm) and glue (RI: 1.52, thickness: 300 µm), respectively [139] and were defined as dielectric–dielectric and dielectric–metalloid surface boundaries. Neutron interaction with matter was simulated by including the `G4HadronPhysicsFTFP_BERT_HP` physics list. For the energy deposition by the alpha and tritium particles created by the capture of neutrons in the scintillator `G4EmStandardPhysics` list was included and the propagation of photons were simulated in the code with `G4OpticalPhysics`.

After simulations, the `ROOT 7_v6-08` [140] package was used for data analysis and processing of the simulation results. It is designed for particle physics and can handle large data sets with high computing efficiency. Further, a set of bindings called pyROOT were utilized to combine the scripting language Python with the ROOT tools, in order to calculate the desired figures of merit.

The objectives of the simulations were to find a suitable light guide and examine its influences on reaching the desired specification. For this purpose a series of dedicated simulations

Table 5.3: Simulation parameters utilized in the Geant4 model.

Variable name	Value	Description
/var/scint/beamWidth	1 mm	width of the neutron beam
/var/scint/neutronEnergy	3.27 meV	energy of neutron
/var/scint/beamAngle	0	angle of the beam
/run/beamOn	10,000	number of neutrons
/var/scint/aluminiumMount	true	aluminium cap on
/var/scint/aluminiumReflectivity	0.8	reflection percent of Al cap
/var/scint/gapLength	0.2 cm	gap between Al cap and GS20
/var/scint/thickness	1 mm	thickness of GS20
/var/scint/glassRindex	1.55	R.I of GS20 glass
/var/scint/backPolish	1	Back polishing on GS20
/var/scint/frontPolish	1	Front polishing on GS20
/var/scint/scintYield	6000	number of photons for each neutron
/var/scint/enrichment	0.95	Li-6 enrichment percentage in GS20
/var/scint/fastTimeScint	50 ns	GS20 fast decay time
/var/scint/slowTimeScint	70 ns	GS20 slow decay time
/var/scint/yieldRatio	0.5	GS20 yield ratio for fast and slow photons
/var/scint/glueThickness	300 µm	gel thickness between GS20 and PDPC
/var/scint/glueRindex	1.46	R.I of the gel between GS20 and PDPC
/var/gel/gapLength	1.1 mm	light guide thickness
/var/gel/gelRindex	1.523	R.I of the light guide
/var/photoncounter/glueThickness	300 µm	glue thickness between light guide and PDPC
/var/photoncounter/glueRindex	1.521	R.I of the glue between light guide and PDPC
/var/photoncounter/thickness	0.1 mm	thickness of the PDPC surface
/var/photoncounter/rindexSi	5	R.I of the PDPC

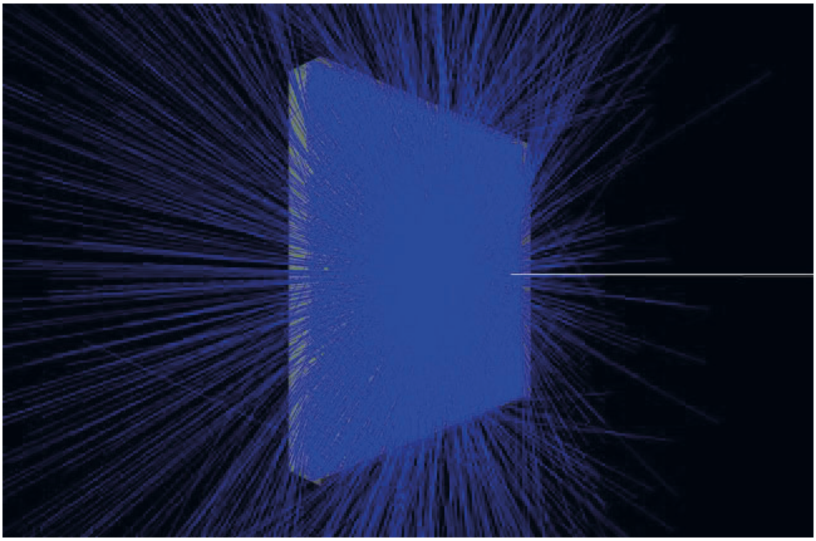

Figure 5.6: Picture of the Geant4 simulation of the model, showing a neutron event impinging perpendicularly onto the detector and generating isotropic scintillation photons (in blue). Reproduced with permission from [151].

were performed varying the thickness and the RI of the light guide by setting the respective variables (Fig. 5.6). For each parameter set, 10 000 neutrons ($\lambda = 5\,\text{Å}, \mathrm{E} = 3.27\,\mathrm{meV}$) were simulated (see Table 5.3).

5.1.2 ANTS2

Another simulation tool, ANTS2 [141], was also tested within this work due to its relatively easy usage. This tool is also implemented in `C++` and based on the Monte Carlo method, and is an acronym for Anger camera type Neutron detector: Toolkit for Simulation. Due to the generality of Geant4 and universal application, physics processes are elaborate. Therefore, it takes longer time and has difficulties in fine tuning parameters for optimization. This lead to the development of ANTS2 for *Anger* camera [11] based gamma or neutron detectors. In addition to simulating the particle source, tracking, generating and tracing scintillation photons, and generating photodetector signals, it also features the tools for position reconstruction from the simulated energy depositions, which is not available in Geant4. For storing the detector geometry and perform 3D navigation, ROOT package from CERN [142] is used

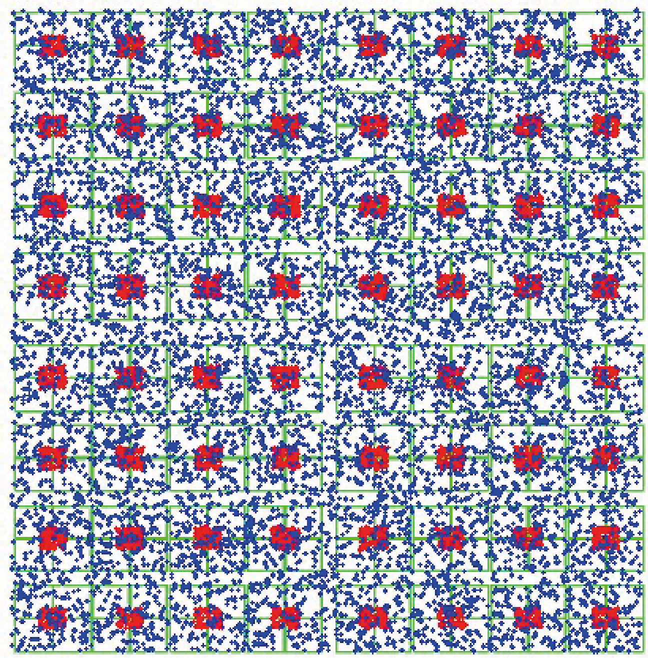

Figure 5.7: A photograph showing the model of one fourth of the detector and reconstructed image (blue dots: simulation points / red dots: reconstructed points) with center of gravity method for 100 000 neutrons events distributed randomly for the simulation using ANTS2 kit.

in ANTS2. The tool's strength lies in the iterative reconstruction of detector response employing different built-in algorithms to optimize the reconstruction procedure for a given detector. It also offers a selection of algorithms, including various statistical and neural network methods.

One quarter of the detector was modeled in the ANTS2 geometry along with the required simulation parameters and then the simplest method, COG (or centroid, detailed in sec. 6.1), was employed to check its performance. The implemented model and the reconstructed image for 100 000 neutron events is shown in Fig. 5.7, which shows a high discrepancy between simulated and reconstructed neutron positions. In order to obtain better reconstructed results, statistical methods with an iterative approach were implemented. These require the light response function (LRF) of the system, i.e. the expected signal depending on the position of the light source. In these approaches the LRFs for each PDPC pixel are calculated iteratively

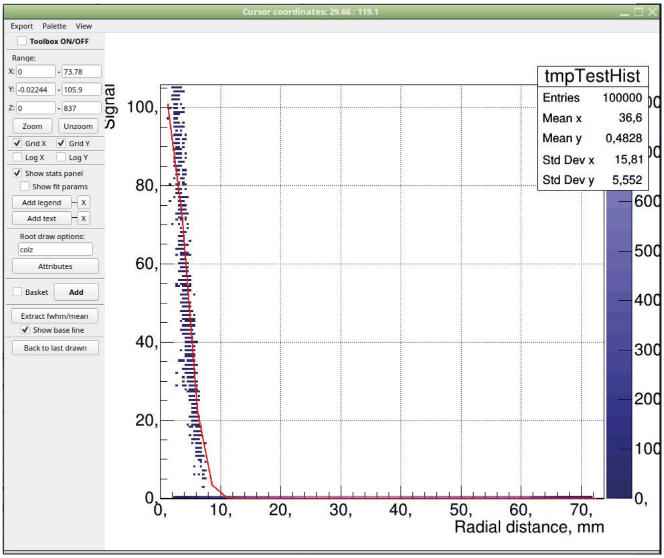

Figure 5.8: A photograph showing the light response function (LRF) created for the implemented detector prototype geometry in ANTS2. Where red line is the fit for data obtained from, four pixels only and further reconstruction using statistical method.

until a good fit between simulated and reconstructed response is achieved by tuning some parameters.

Unfortunately, the algorithms used in ANTS2 are optimized for detectors providing many pixel responses per event (9 or more), while our detector provides only four pixel counts per event. Therefore, the results with ANTS2 were not well suited due to unsatisfactory LRF (see Fig. 5.8) and needed further effort and time. Thus, Geant4 simulations results and a custom reconstruction algorithm for the detector were used.

5.2 Simulation Outcome

In case of a neutron capture, photons are created with random direction and wavelength according to the emission spectrum of Cerium doped ^{6}Li-glass. For each event the position and time of any photon, hitting the SiPM surface is stored for analysis. The geometry and performance of the PDPC pixels, as well as the PDPC readout cycle (see sec. 3.4.2) chosen, are taken into account during the data analysis. In order to analyse the simulation data for the selection of optimal light guide parameters, two figures of merit were defined: average number of photons detected per neutron event and distribution of light across the pixels. Higher the value of average photons detected more the statistics and better for the reconstruction algorithm. While distribution is also significant because wider the spread of the light, higher is the probability that multiple pixels will provide the data that will favour better reconstruction.

The simulation results as reported in [139] concluded that out of 0.2 mm to 2 mm thick glass and air, 1 mm thick glass with a RI of 1.5, closely matching to the scintillator glass (1.55) provides a good trade-off between detected photons and its distribution. For 1 mm thick glass, the average number of photons detected is approximately 400 (see Fig. 5.9) with a distribution of 4 mm FWHM (see Fig. 5.10). From these numbers light is sufficient for a good signal to noise ratio (> 4), i.e. threshold against gamma events and DCR, as well as reconstruction, i.e. distributed over multiple pixels for reconstruction with a sub-pixel accuracy. A thicker light guide leads to decrease in the photon density and triggering less microcells in PDPC, as indicated in Fig. 5.9. A similar effect can be observed for lower refractive index. Additionally, total internal effect also plays a role at the surface between scintillator glass and the light guide, leading to higher reflection for indices below the index of scintillator glass i.e. 1.55. With air (RI: 1.0) as the light guide, the detected photon count is relatively low, for instance 140 vs. 410 (for glass having RI: 1.5). This is mainly due to higher rate of internal reflection at the scintillator and light guide boundary. Therefore, an air gap was no longer considered for the light guide.

The simulations were also utilized for creation of LRFs by integrating the photon distribution over the pixel area, which was required for creation of look up table (LUT) (see Fig. 5.11). The latter was needed to estimate $\langle n_i \rangle_{x,y}$, the number of photons hitting a pixel for a neutron event at a specific position.

5.3 Assembly of the Detector

Beginning with the optical front-end, the first step of assembly was to glue the light guide (65.4 mm $\times$ 65.4 mm $\times$ 1.1 mm), i.e. glass onto the SiPM modules, i.e. PDPC. A UV and light curing epoxy resin [143] was used as the adhesive for this purpose and experts were asked to help to achieve this task. It is found during the gluing process that the surface of the PDPC module is not flat (uneven up to 0.4 mm), which might be due to tilting of

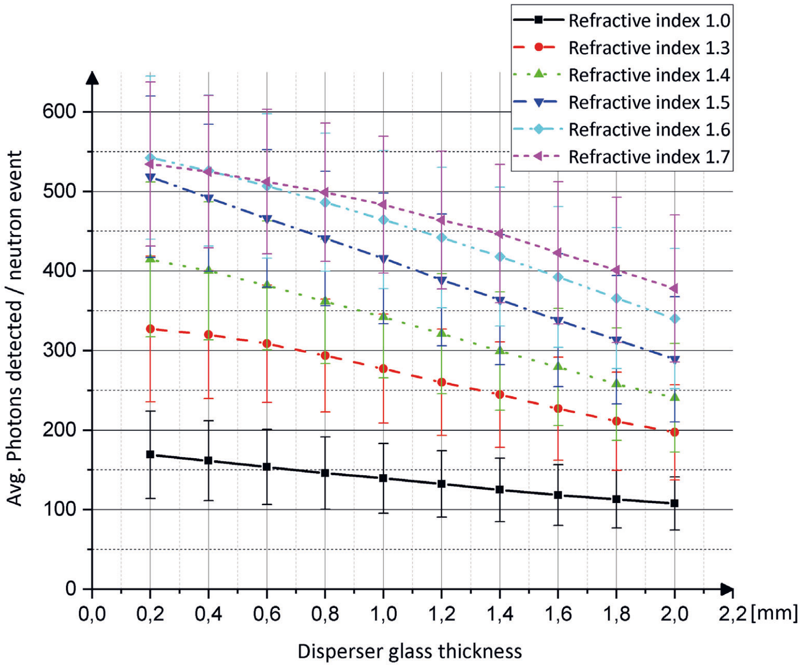

Figure 5.9: Geant4 simulation results, using 1 mm thick scintillator glass (GS20), showing the influence of the light guide's thickness and refractive index on the average number of photons detected. Reprinted with permission from [139].

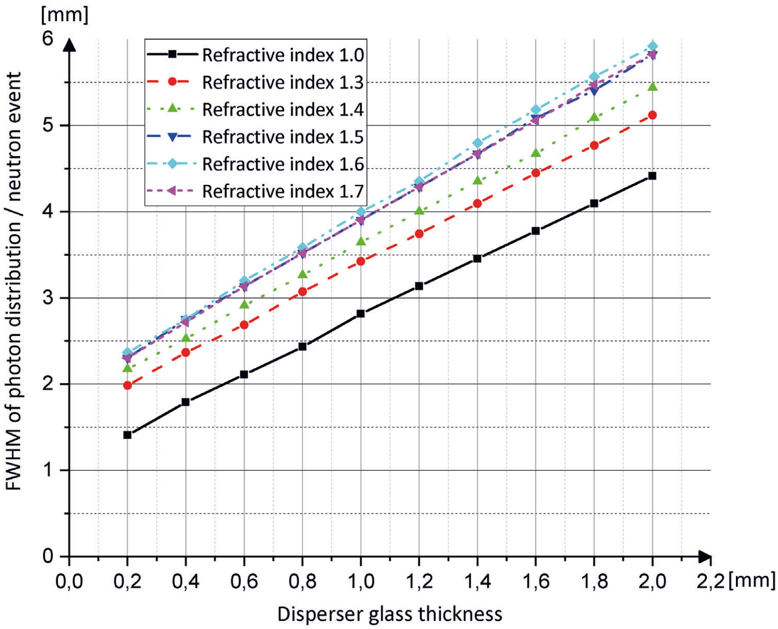

Figure 5.10: Geant4 simulation results, using 1 mm thick scintillator glass (GS20), showing the influence of the light guide's thickness and refractive index on the full width at half-maximum (FWHM) value of the photon distribution on PDPC surface. Reprinted with permission from [139].

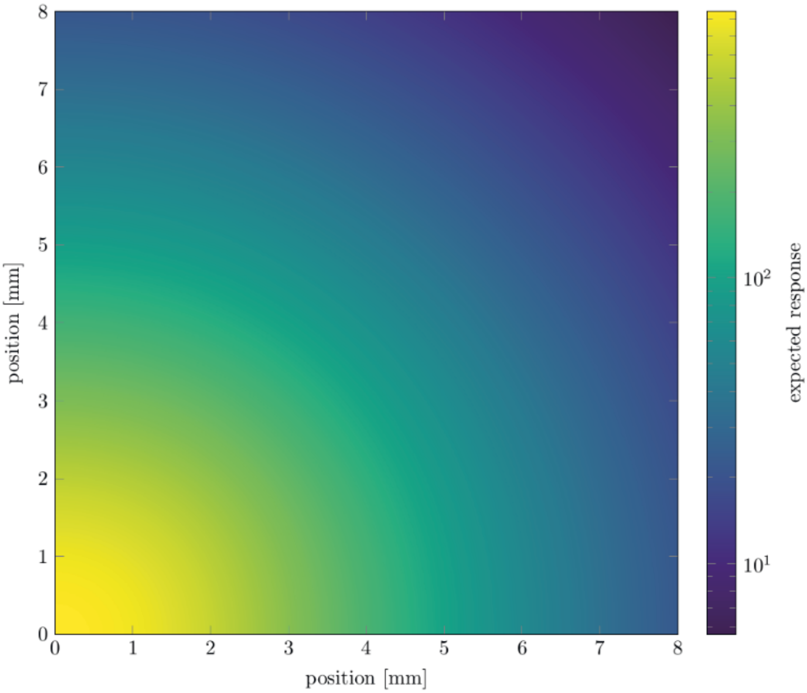

Figure 5.11: Example of a pixel look up table (LUT), created using the simulation data within 8 mm × 8 mm for pixel at (0, 0) and neutron event at (x, y), reproduced with permission from [156].

Figure 5.12: Picture of two PDPC modules mounted on the array holder and connected with the data transmission board during the assembling.

the *tiles* (four *tiles* in a *module*). This posed a challenge in determining the exact distance between scintillator and SiPM, which is needed in the simulations to calculate the LUT [144]. The PDPC modules were mounted on the array holder with a thermally conducting pad in between for a better heat conduction. The data transmission boards were then connected from behind to the Samtec connectors of the PDPC. With the readout boards in place, the array holder is then connected to the Peltier cooling system (see Fig. 5.12).

In order to find the optimal removable coupling between the scintillator and light guide, we compared different options like Silicon rubber pad, Silicon gel and Silicon grease [145,146]. The most important property for us was the RI, which should match our scintillator glass (1.55) for an efficient light transport with a minimum loss due to internal reflection. We chose a Silicon grease from Eljen [147] due to its excellent light transmission properties for wavelength range of our interest, i.e. 300 nm to 500 nm and its RI of 1.47. However, because of its moderate viscosity it was not an easy task to get a coupling free of air bubbles across the whole surface, especially on the edges (see Fig. 5.13). It is advised to carefully apply pressure to the scintillator glass in order to spread the gel uniformly. In our case, the glass suffered a little damage (see Fig. 5.14a) during this process. Later on we used grease from Saint-Gobain [148], which was easier to use. The layers of the optical front-end are shown in

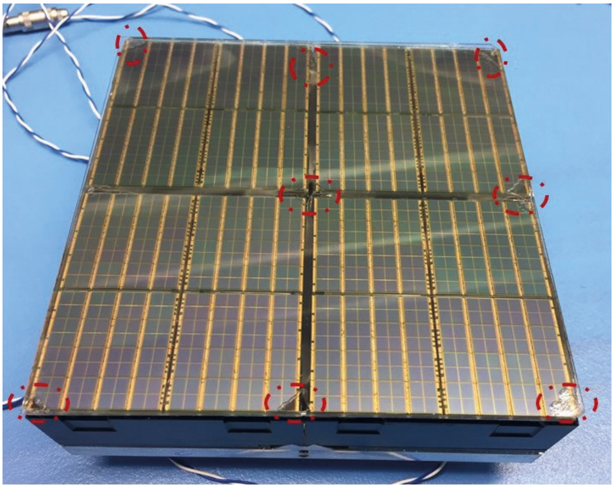

Figure 5.13: Picture showing the scintillator glass coupled with the light guide using Silicon grease. The dotted circles show air bubbles.

(see Fig. 5.14b).

After coupling PDPC, light guide and scintillator glass, the optical front-end is covered with a light tight Al cap. Then, the detector head is connected to the concentrator board, Peltier elements regulator, power supply and computer (see Fig. 5.15) to be ready for the measurements.

5.4 Validation of Simulation

It was necessary to validate the simulations, not only to confirm the light guide choice, but more importantly for the algorithm employed for the reconstruction. As mentioned, the algorithm is based on simulation data so it was necessary to compare it with the experimental data to check its reliability. Therefore, measurements have been performed at the detector test station V17 (flux of 3×10^5 n/cm^2/s) [149] at research reactor BER-II of the Helmholtz-Zentrum Berlin. Before the experimental campaign at BER-II, first measurements at TREFF [150] instrument at FRM-II, Garching, were performed. However, besides some initial data that was helpful for the test, we were not able to obtain significant results during that measurement due to technical problems.

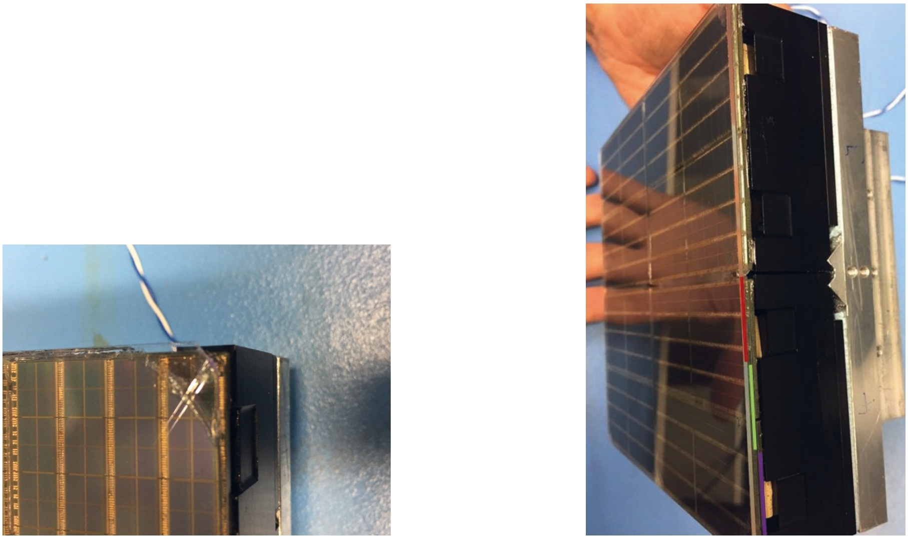

(a) **(b)**

Figure 5.14: Picture showing (a) broken scintillator glass at the edge during the optical coupling process (b) the optically coupled layers together, i.e. scintillator glass (in red), light guide (in green) and PDPC surface (in purple).

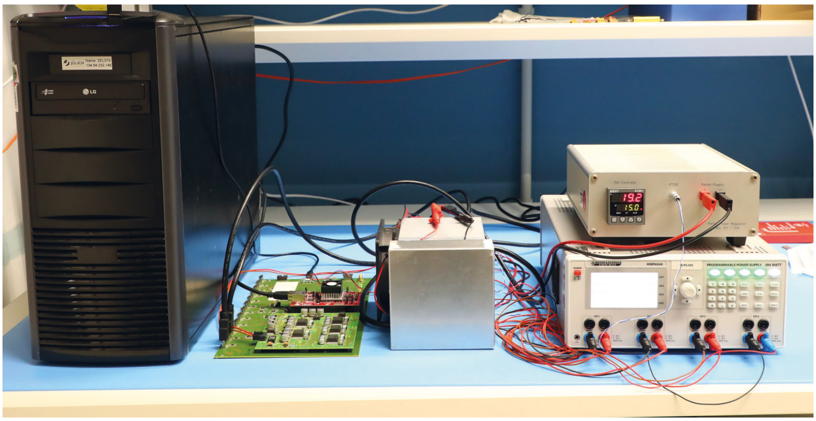

Figure 5.15: Photograph of the whole detector system (from left: PC, concentrator board, detector head, power supply and Peltier regulator.

The detector was placed directly in front of the beamline (see Fig. 5.16) with a beam aperture of 40 mm × 40 mm. For the different configurations of the light guide, we used the same measurement settings and exposed the detector for 5 minutes with cold neutrons ($\lambda = 3.35$ Å). Two parameters that can be calculated from the experiment results were chosen for the validation: average number of photons detected per neutron event and maximum brightness ratio, i.e. brightest pixel response divided by the sum of all pixel counts. Due to technical difficulties, only two measurements (1.1 mm and 1.65 mm thick) were done considering both glass and airgap as the light guide and the comparison between simulation and measurement results were plotted [151].

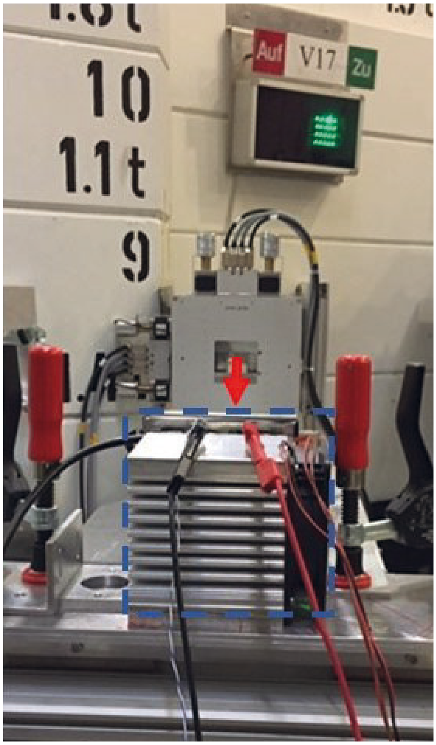

Figure 5.16: Photograph of the experimental setup of the detector prototype (blue dotted square) in front of the neutron beam line (red arrow) at V17 test station at BER II, Berlin.

The average number of photons detected per neutron event was calculated by adding the total number of photons detected by the whole SiPM array during the measurement time divided by the accumulated flux. As it is expected from Lambert-Beer law, thicker glass will absorb more photons and will lead to lower photon counts, a similar trend observable in both the curves from simulations and measurements in Fig. 5.17.

As mentioned, in order to reconstruct the position of a neutron with a sub-pixel accuracy, a certain distribution of light among the pixels is favored. For this purpose, maximum brightness ratio was defined to observe the distribution of photons across the SiPM surface. It was calculated by dividing the photon count of the pixel with the highest photon count by the sum of the counts of all pixels on the same neutron event, and averaging it over all neutron events. The maximum brightness ratio should decrease with increase in thickness of the glass because the photon density on the SiPM surface will decrease due to the divergence

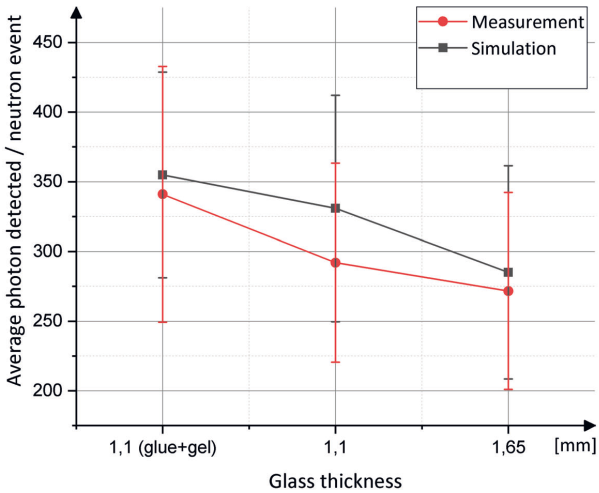

Figure 5.17: Comparison of average number of photons detected per neutron event, obtained from the Geant4 simulation results and the measurements performed at V17 instrument at BER-II, Germany for glass as the light guide configuration. The error bars shown in the graphs represents the standard deviation value. Reprinted with permission from [151].

of light from the isotropic source. This behaviour can be seen in both the simulation and measurement plots in Fig. 5.18. In addition to quantitative comparison of maximum ratio, qualitative comparison also suggests a good agreement between simulation (see Fig. 5.19) and measurement (see Fig. 5.20).

Figs. 5.17 and 5.18, show a good resemblance between the simulations and measurements. The obtained results confirm the validation of simulation data for various light guide configurations (for airgap refer to [151]) and are also comparable to the simulation results (see sec. 5.2). The quantitative and qualitative comparison (Figs. 5.19 and 5.20) of experimental and simulated data not only validates the implemented simulation model but also provides a better understanding of the detector prototype. Moreover, it also increased the confidence to use the simulation data for position reconstruction algorithm and contributed towards its improvement by utilizing appropriate simulation model.

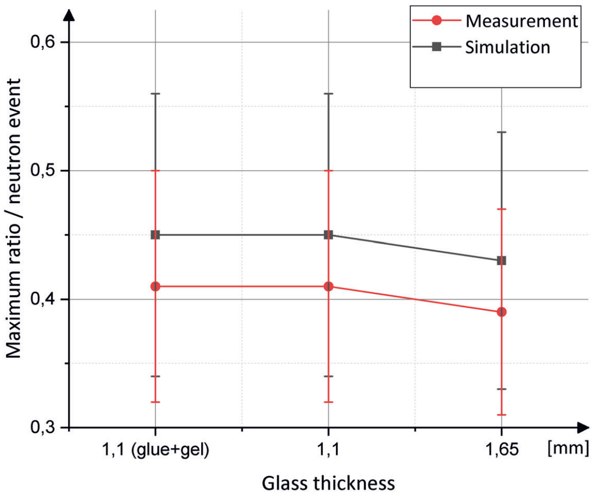

Figure 5.18: Comparison of the Geant4 simulation results and the measurements performed at V17 instrument at BER-II, Germany for the maximum ratio per neutron event for glass as the light guide. The error bars shown in the graphs are the standard deviation value. Reprinted with permission from [151].

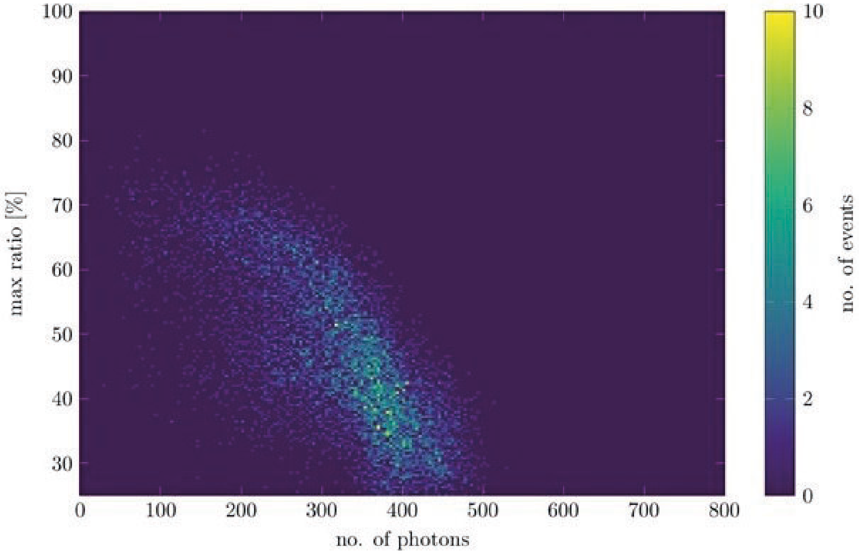

Figure 5.19: Graph for qualitative comparison of maximum ratio per neutron event from simulation data for 1.1 mm thick glass as the light guide.

5.5 Non-linearity Simulation

Non-linearity is an intrinsic property of an SiPM due to the limited number of SPADs, which are rendered unresponsive for a certain recovery time to subsequent photon hits after triggering. This is already discussed in sec. 3.5.3 and there exist studies for the non-linearity corrections (refer to (3.5.9)) under the assumption of homogeneous light exposure. However, during the simulation of the light guide (glass), it was observed that the light generated by neutron interaction with GS20 (see Fig. 5.4) is not homogeneous across the surface of a pixel. For a better understanding, a series of simulations were carried out to study the influence of light guide (glass) thickness on light inhomogeneity, which in turn leads to non-linearity due to microcell saturation.

The glass thickness was varied from 0 mm to 2 mm in the simulations at a step of 0.2 mm and photon density around the neutron event position was plotted in order to analyse the distribution of light. Fig. 5.21 shows the plot for a glass thickness of 1.1 mm, which illustrates inhomogeneity within a pixel. A peak incident photon density of ∽130 photons/mm^2 around the center of the pixel was observed for 0.2 mm thick glass. In comparison, the micro-cell

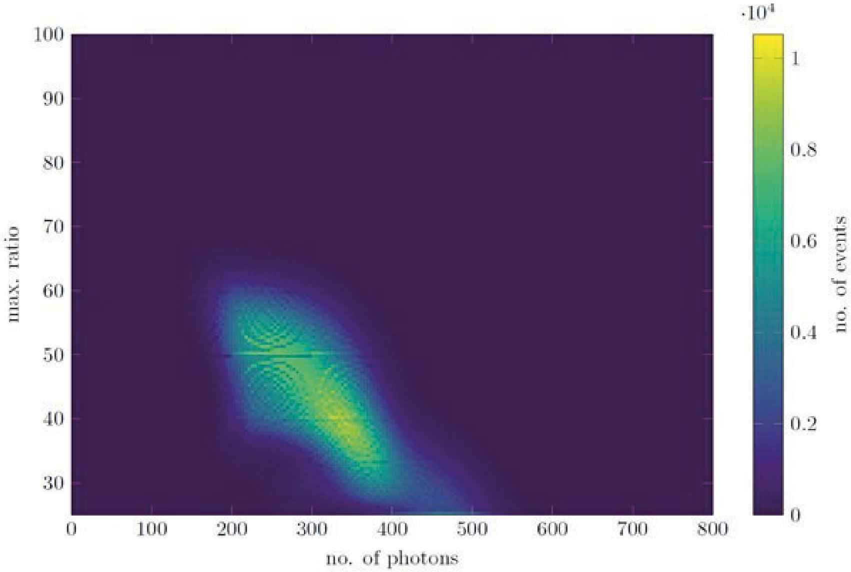

Figure 5.20: Graph for qualitative comparison of maximum ratio per neutron event from experimental data for 1.1 mm thick glass as the light guide.

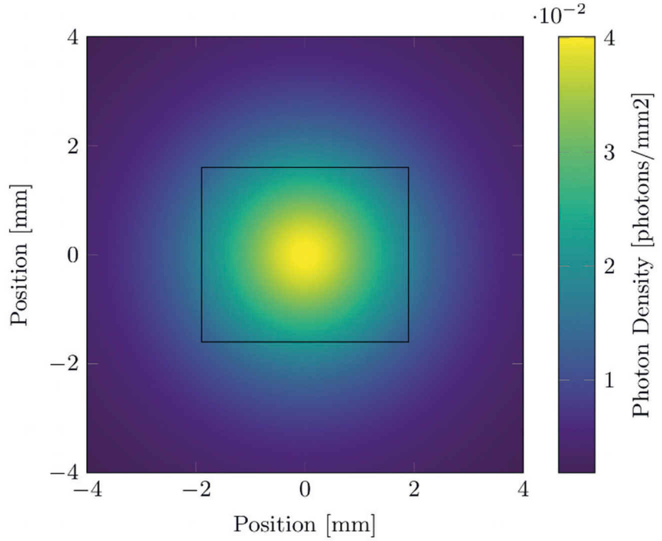

Figure 5.21: The plot for photon distribution density (photons/mm^2), using Geant4 simulation (10 000 neutrons) for 1.1 mm thick light guide for a neutron interaction simulated at (0, 0) mm perpendicularly. The rectangular box in the picture depicts the dimension of a pixel and clearly shows the inhomogeneity within it. Reproduced with permission from [152].

density of the PDPC is about ∽260 microcells/mm^2. In general, SiPMs respond linearly if the number of photons is significantly lower than the number of micro-cells, otherwise it will saturate and deviate from linearity. Due to this, a correction is required to evaluate the true number of photons detected.

These findings motivated to investigate the effect of inhomogeneity on the non-linearity correction. The correction is important for finding the correct number of photons, which is required by the reconstruction algorithm. There exist standard non-linearity correction formula ((3.5.9)) that can be implemented for finding the correct number of fired microcells for a given number of photons incident on the number of microcells. However, the formula ((3.5.9)) assumes a homogeneous photon distribution. Therefore, a study has been performed on the microcell level to consider inhomogeneity, which to the best of our knowledge has not been investigated before. For this purpose a model was derived utilizing the photon distribution density [152]. The model is based on simulation and not validated with measurements.

As mentioned earlier (sec. 2.2), each neutron creates an event with a decay time of 50 ns to 70 ns that causes a certain amount of photons to hit the photosensitive surface. Since the whole surface is divided into spatial intervals, i.e. micro-cells, it can be assumed that the total number of photons n hitting a single micro-cell i during a single neutron event follows a Poisson probability distribution, if we neglect correlated noise (e.g. crosstalk) (5.5.1):

$$P_i(n) = \exp\left(-\lambda_i\right) \cdot \frac{{\lambda_i}^n}{n!} \tag{5.5.1}$$

The mean λ_i of this distribution is the expected number of photons hitting micro-cell i during the neutron event. The expected number of fired cells during the event is (5.5.2):

$$\langle N_{firedcells} \rangle = N_{cells} - \langle N_{emptycells} \rangle \tag{5.5.2}$$

where N_{cells} is the number of cells in a pixel and $N_{emptycells}$ is the number of cells not triggered by a photon. If we assume that the statistical processes in different cells are independent of each other, using (5.5.1) we have

$$\langle N_{emptycells} \rangle = \sum_i P_i(0) = \sum_i \exp(-\lambda_i) \tag{5.5.3}$$

The λ_i are not equal to each other (for inhomogenous photon distribution) and can be calculated by integrating the photon distribution density ρ_{pd} of the neutron event over the microcell's area A_i:

$$\lambda_i = P_{PDE} \cdot \int_{A_i} \rho_{pd}\, dr^2 \tag{5.5.4}$$

where P_{PDE} is the photon detection efficiency of the SiPM and dr^2 means integration in two dimensions (x, y). Using the common assumption of a homogeneous photon distribution for (5.5.2), the Poisson parameters λ_i are all equal to $P_{PDE} \cdot N_{ph}/N_{cells}$, where N_{ph} is the number of impinging photons, and the usual non-linearity correction formula ((3.5.9)) is recovered.

For inhomogeneous distribution the non-linearity correction model for implementation on microcell level can be derived using (5.5.2) and (5.5.3), provided λ_i values are known from (5.5.4). For this correction model, the pixel is divided into smaller areas (e.g. 100 microcells), and $N_{firedcells}$ is evaluated by finding λ_i for the given areas.

Using a very thin (e.g. few µm) scintillator and neutron pencil-beam scan, the divergence of light on the SiPM could be determined experimentally. However, it would require a lot of resources, especially scanning at such a narrow step is a tedious task. Additionally,

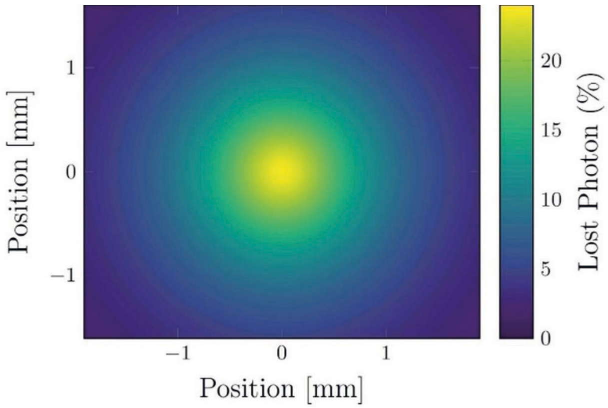

Figure 5.22: Depiction of a two dimensional diagram of photon loss within a pixel 3.8 mm × 3.2 mm i.e. on micro-cell level, according to the inhomogeneous photon distribution model for a 0.2 mm thick light guide. Reproduced with permission from [152].

availability of a pencil-beam and neutron detection efficiency with a thin scintillator is an issue. Therefore, it was not feasible to measure the ρ_{pd} experimentally and instead resorted to simulation data.

The photon loss N_{lost} and relative loss in % were calculated as:

$$N_{lost} = N_{ph} \cdot P_{PDE} - N_{firedcells} \tag{5.5.5}$$

$$N_{lost}(\%) = \frac{N_{lost}}{N_{firedcells}} \cdot 100 \tag{5.5.6}$$

The peak photon loss due to saturation in the case of 0.2 mm thick glass is 24 % (see Fig. 5.22). Whereas for 2.0 mm thick light guide, the peak loss observed is only 3 % (see Fig. 5.23). The correction using the standard homogeneity model for 0.2 mm thick glass provides 7 % (see Fig. 5.24) on the pixel level, while the inhomogeneity model gives a correction factor of 9 %. The difference in the model can be observed in Fig. 5.24. It is more significant for thinner light guide because of higher inhomogeneous distribution caused by lesser spread of the light.

The light guide employed in the detector prototype was 1.1 mm thick glass, based on the light guide analysis [139]. For this thickness, the 0.4 % difference between the homogeneous and inhomogeneous correction factor was considered negligible. Therefore, the homogeneous

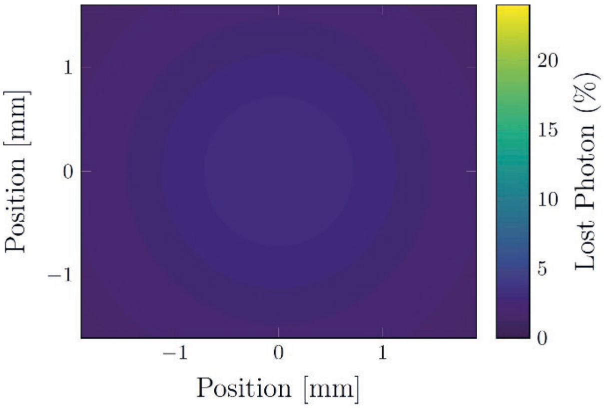

Figure 5.23: Depiction of a two dimensional diagram of photon loss within a pixel 3.8 mm × 3.2 mm i.e. on micro-cell level, according to the inhomogeneous photon distribution model for a 2.0 mm thick light guide. Reproduced with permission from [152].

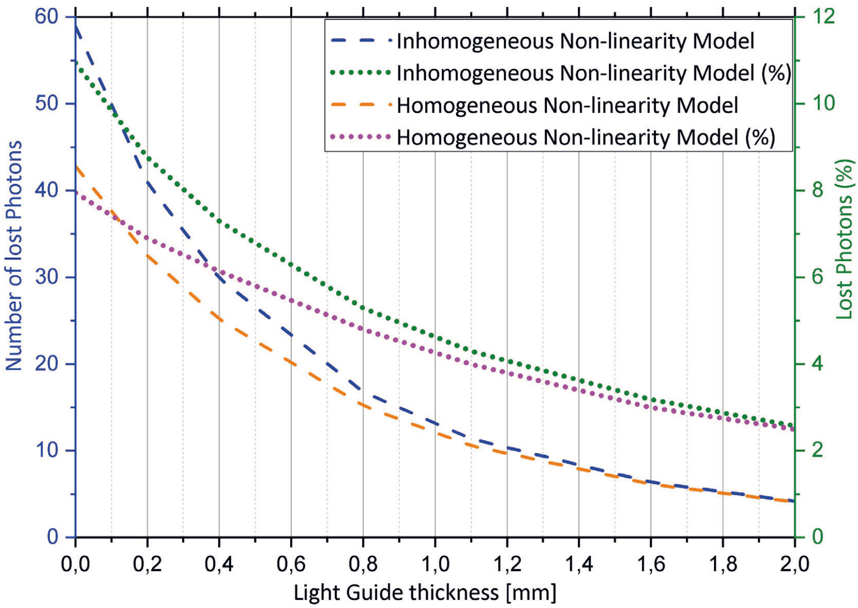

Figure 5.24: Graph showing a relation between light guide thickness and the number of photons lost averaged over a pixel due to micro-cell saturation, for homogeneous and inhomogeneous photon distribution models. Reproduced with permission [152].

model was used for non-linearity correction due to lower computational complexity. Nevertheless, the outcome of the investigation [152] suggests that in general the photon distribution should also be examined in non-linearity analysis of SiPM together with the number of photons.

In summary, a simulation model was developed for finding the optimal design of the optical front-end of the detector prototype, which favours 1.1 mm thick glass with 1.5 RI. As well as series of simulations were performed to generate the data for its utilization in reconstruction algorithm. Later on, bubble free (minimal) coupling of the scintillator glass onto the light guide was achieved and the detector system was assembled to carry out experiment. The detector was tested at BER-II and the experimental results verified the model. Additionally, non-linearity of SiPM was studied in detail to establish a correction model for inhomogeneous light impinging the SiPM. This helps in better understanding of photons detected by the SiPM in the detector system.

Chapter 6

Position Reconstruction Algorithm

Two approaches can be employed to locate the primary neutron interaction: statistical methods and neural network methods. The latter is inspired by biological process and based on human brain mimicry. Commonly implemented neural networks are artificial neural network (ANN) [153], convolutional neural network (CNN) [154] and k-nearest neighbour logic (kNN) [155]. These methods require detailed and extensive training data (simulation or experimental), which was not obtained in this work. Experimentally, this would require the detector's response to a pencil neutron beam, which is time consuming considering the beam-time availability in the research reactors (FRM-II and BER-II). Additionally, using the simulation data for training will be a reliability issue. This means that inaccuracy in simulation could lead to error in the output, i.e. the position of neutron, created from training that utilizes simulations. Therefore, analysis for neural network implementation was not within the scope of this work.

In the statistical approach, a mathematical model is developed that is compared with the simulation or experimental data. The values of the unknown parameters, in our case the position of the neutron, are estimated by an estimator function (Least square and Bayesian for this work).

6.1 Center of Gravity

The COG or centroid approach is probably the simplest statistical method to get information on the event position and is a classical method introduced by *H. O. Anger* in his gamma camera [11]. The location of the gamma ray interaction was estimated by the distribution of signal amplitudes in the photosensors (PMTs). This process involves summing the signal amplitudes of all PMTs and calculating the centroid of the position-weighted PMT outputs. It provides an approximate estimation of the event position, but suffers from distortion effects, especially at the edges, and has a bias towards the center of the PMT.

We utilized the COG method as an initial estimation for the neutron position, which is then refined by another statistical algorithm. The COG reconstruction is implemented as the weighted mean of all pixel positions with weight equal to the number of hits in that pixel (6.1.1):

$$\vec{x} = \frac{\sum C_i \cdot \vec{P}_i}{\sum C_i} \tag{6.1.1}$$

where $\vec{P}_i$ is the position assigned close to the corresponding corner of the die for each SiPM pixel and C_i is the pixel count in pixel i measured for the corresponding neutron event.

6.2 Least Square

This method searches the neutron position which results in the best match between the measured data and the expected response obtained from simulations. It uses the sum of the square of the difference weighted by the expected signal as a FOM. In essence, it searches for a minimum of the function W, defined as:

$$W(x, y) = \sum_{i=1}^{4} \frac{\left(\langle n_i \rangle_{x,y} - C_i\right)^2}{\langle n_i \rangle_{x,y}}, \tag{6.2.1}$$

where $\langle n_i \rangle_{x,y}$ is the expected number of photon counts in pixel i, which is the average response to many simulated neutron events at (x, y). The values for different positions were stored in a so called pixel expectation LUT (see Fig. 5.11 for example) for performance reasons.

For finding the minimum of W, a minimization algorithm such as steepest descent or contracting grid search can be used. For each event we limit the search to an area centered around the start search position, i.e. COG point, and try to find the minimum value of W, which is our estimation for the neutron position (refer to appendix. A.1). Discretization ($\backsim$100 µm) of the area was done to increase the performance of the algorithm, so that the algorithm does not look into the whole area and save the time. The 136.5 mm side length was divided into 1024 channels and only points (x, y) on the resulting mesh for minimization of the function W were considered to reduce the computational effort.

6.3 Bayes Inversion

The Bayes Inversion method is a probabilistic model in which an observation is given and the task is to infer properties of the system. It is necessary to specify a prior probability function over the variables of the model. The variables in this case are the expected number of photon counts for a given neutron position $\langle N_i \rangle_{x,y}$ obtained from simulations and photon counts $C_{i=1,2,3,4}$ (four pixels) in a *die* measured experimentally. The prior probability or conditional probability function was calculated implementing the Binomial distribution[1] for the probability of measuring a certain number of counts C_i out of an expected number of photons $\langle N_i \rangle_{x,y}$ and is expressed as (6.3.1),

$$P(c|(x,y)) = \prod_{i=1}^{4} \binom{\langle N_i \rangle_{x,y}}{C_i} \cdot p^{C_i} \cdot (1-p)^{\langle N_i \rangle_{x,y} - C_i} \tag{6.3.1}$$

where p is the PDE of the sensor (31 %, refer to sec. 2.3). Once the probability $(P(c|(x,y)))$ of counts for a neutron hit is calculated, the probability of a neutron hit at (x, y) for a given number of counts is evaluated following (6.3.2) through Bayesian inversion approach.

$$P((x,y)|c) = \frac{P(c|(x,y)) \cdot P(x,y)}{P(c)}, \tag{6.3.2}$$

where $P(c)$ is the prior probability and acts as a normalization factor.

The Binomial factor in (6.3.1) is zero for $C_i > \langle N_i \rangle_{x,y}$. It can be observed from Fig. 5.11 that the value of $\langle N_i \rangle_{x,y}$ decreases exponentially with distance to the neutron event position. Therefore, the support of $P((x,y)|c)$ is finite, and thus the integral can be computed exactly by integrating over a finite area.

Further, the expected positions are reconstructed as per (6.3.3) and (6.3.4), by integrating the above probability function $(P((x,y)|c))$ over the finite area A with COG point serving as the center of integration area A (refer to appendix. A.2).

[1] k (detected pixel counts from measurement) successes in n (expected pixel counts from simulation) trials.

$$\langle x\rangle = \iint_A (x \cdot P((x,y)|c)))\, dx\, dy \tag{6.3.3}$$

$$\langle y\rangle = \iint_A (y \cdot P((x,y)|c)))\, dx\, dy \tag{6.3.4}$$

6.4 Algorithm Comparison

Both algorithms were implemented in Python programming language (refer to appendix. A). Two parameters were considered for the comparison of their performance: position resolution and run time. Firstly, the algorithms were tested with simulation data and then with the measurement data. The measurement data were taken in May, 2019 at the V17 [149] test station of BER-II, Berlin (see Fig. 5.16).

Fig. 6.1 shows the reconstructed position of 50 events simulated randomly on the detector surface. It can be observed from the coordinates of the reconstructed neutron positions that both algorithms have similar response in terms of spatial resolution. The average difference observed between the algorithms towards X and Y coordinates were 0.6 channels (0.07 mm) and 0.5 channels (0.06 mm) respectively. Fig. 6.2 shows the reconstruction of experimental data and shows a similar behaviour with a smaller difference between the points reconstructed by the algorithms: 0.01 mm for X and 0.02 mm for Y. Note, that the difference varies across the detector surface and the values mentioned are only for particular 50 events. However, there exists a significant difference in the algorithms considering the run time, i.e. the time needed for reconstructing a single neutron event (see Table 6.1). The run time for Bayesian algorithm was too large and therefore, it was not feasible to get more samples for comparison.

The reason behind the slow runtime for Bayes is the methodology comprising two-dimensional integration steps ((6.3.3) and (6.3.4)) performed in Python. As there were problems in executing double integration, various methods were tried to improve the accuracy and run time. The first method was a standard function `scipy.integrate.dblquad` from `SciPy` library, which had problems integrating very small numbers (in the order of 10^{-20}) obtained from product of Binomial function ((6.3.1)) and was inaccurate. Two other functions were defined with grid and random approach. In the latter approach, 1 000 000 random positions were chosen within the integration area to obtain the sum as the integral. For the grid approach, 1000 bins were defined between the x and y limits and the function

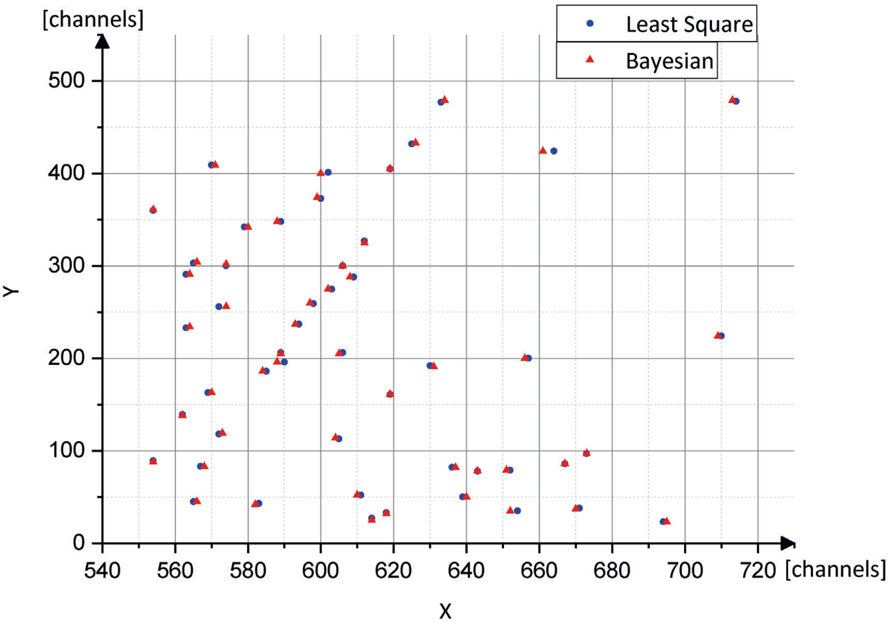

Figure 6.1: Graph depicting comparison of the reconstructed position of 50 neutron events by Least square and Inverted Bayesian algorithms from simulation data (1 channel = 0.13 mm).

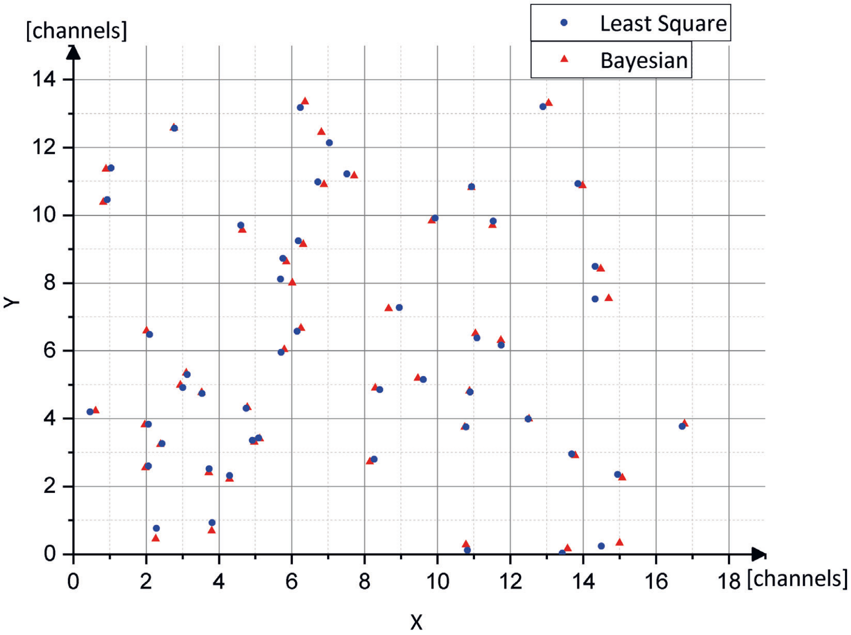

Figure 6.2: Graph depicting comparison of the reconstructed position of 50 neutron events by Least square and Inverted Bayesian algorithms from experimental data. The scaling is significantly smaller than the previous plot (1 channel = 0.13 mm).

Table 6.1: Comparison of spatial resolution and run time of least square and Bayes inversion algorithm implemented for data obtained from simulations and experiments.

Data	Difference in reconstructed position		Runtime per event	
	X	Y	Least Square	Bayes
Simulation	0.07 mm	0.06 mm	$\backsim$0.01 s	$\backsim$300 s
Experimental	0.01 mm	0.02 mm	$\backsim$0.01 s	$\backsim$300 s

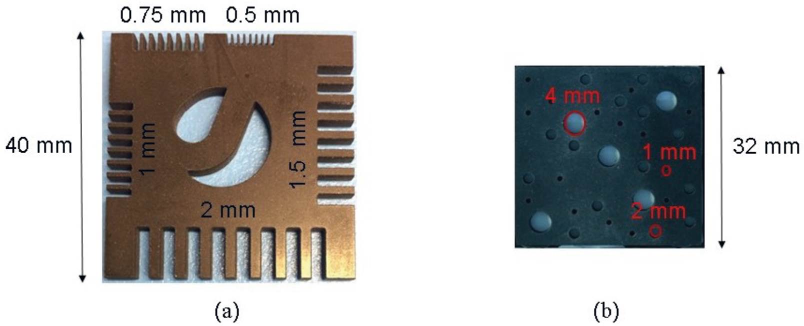

Figure 6.3: Picture of the B_4C mask built for spatial resolution evaluation of the detector prototype (a) J mask (4 cm × 4 cm) having slit structures of 0.5 mm to 2 mm (b) Hole mask (3.2 cm × 3.2 cm) having structures of diameter 1 mm to 4 mm.

value of each bin was multiplied with the bin-width and summed up to get the integral value. These approaches improved the integral accuracy, but the run time remained high. A possible solution could be implementing the algorithms in another programming language such as `C++`. During the measurements millions of neutron events have to be reconstructed to get an immediate image, least square was preferred over Bayes inversion due to the runtime.

6.5 Characterization of the Detector

In order to evaluate the resolution of the detector prototype, two masks (see Fig. 6.3) with different structures (0.5 mm to 4 mm) were made from B_4C for imaging. The least square algorithm (refer to sec. 6.2) was further optimized on the basis of certain parameters (DCR, PDE, and LUT) [144]. The LUT was a significant factor, because the surface of the PDPC was not completely level (discrepancy of $\backsim$0.4 mm) and therefore it was necessary to calculate the

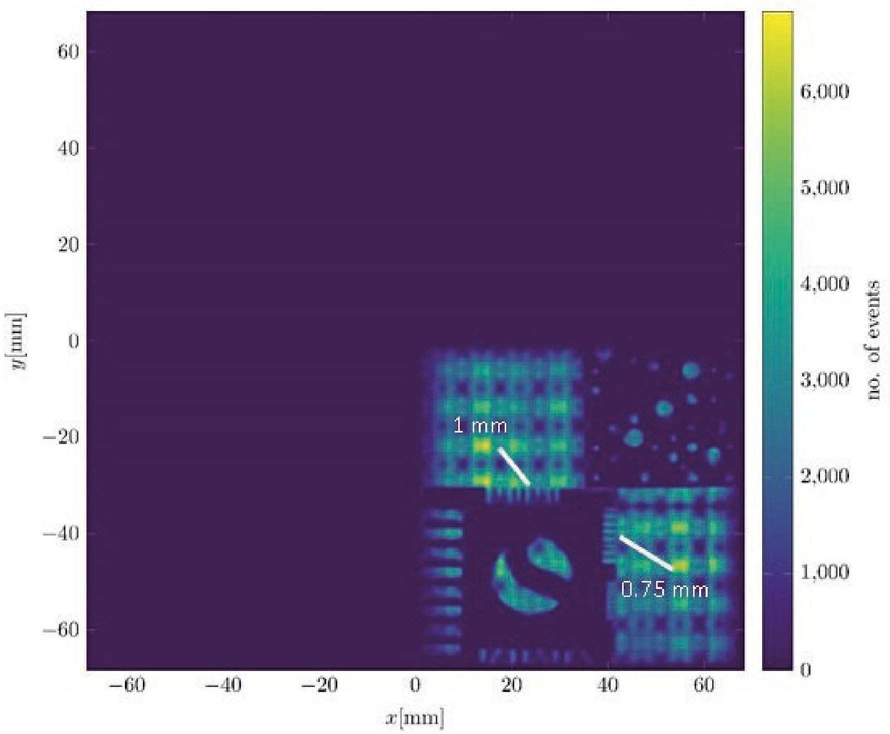

Figure 6.4: Image reconstructed with least square algorithm with both masks placed in one quadrant of the detector. Experiment performed at BER-II, Berlin.

effective light guide thickness for each die separately to create the corresponding LUT [144].

As mentioned earlier, the detector was tested at V17, BER-II with several 5 min measurements during which the masks were placed in front of the detector at different positions. The flux of the beam ($\lambda = 3.35\,\text{Å}$) was $3 \times 10^5\,\text{n/cm}^2/\text{s}$ with an aperture of $4\,\text{cm} \times 4\,\text{cm}$. Some of the reconstructed images are shown in Figs. 6.4, 6.5, and 6.6. It can be seen that the algorithm works effectively near the edges/periphery, which are a major problem associated with most of the available algorithms. Additionally, 0.75 mm slit shapes are also distinguishable in these images.

Moreover, for the quantitative evaluation of the resolution a 1 mm slit mask was placed vertically in front of the detector (see Fig. 6.7). Then the projection of the reconstructed image on the horizontal axis was plotted. Fig. 6.8 shows the plot together with a fit of

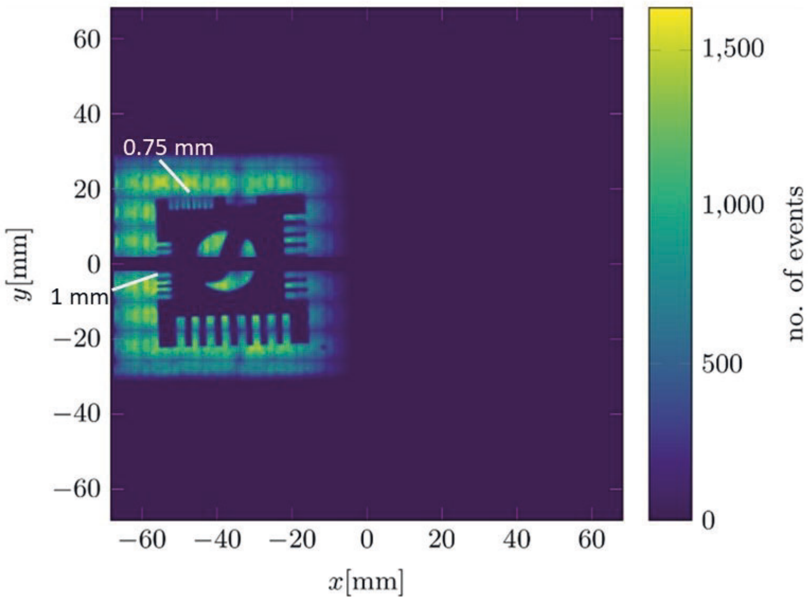

Figure 6.5: Image reconstructed with least square algorithm for J mask placed on the detector. Experiment performed at BER-II, Berlin.

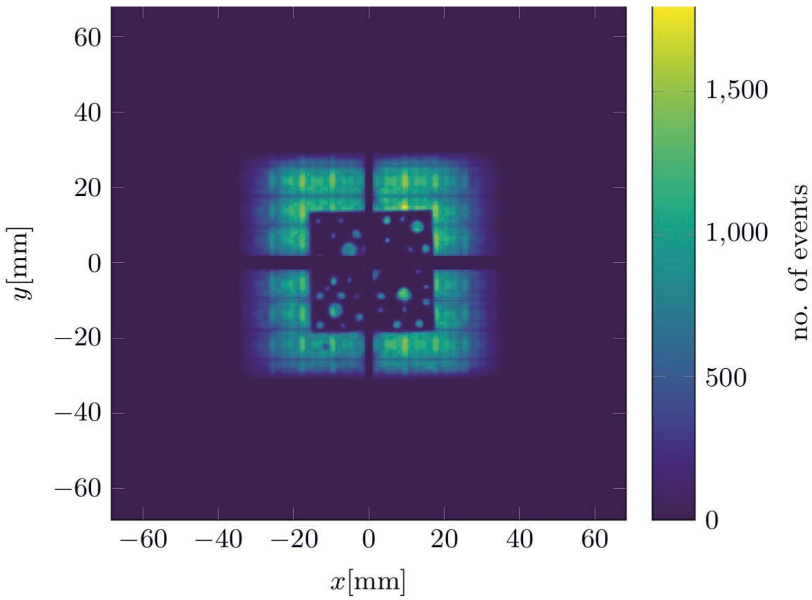

Figure 6.6: Reconstructed image of hole mask placed on the detector with least square algorithm. Experiment performed at BER-II, Berlin.

1 mm rectangular function with a Gaussian blur with standard deviation σ, which shows a resolution of 1.01 mm FWHM for a point source.

The detector was also characterized for count rate, detection linearity, gamma discrimination, and neutron detection efficiency, respectively [156]. The latter was measured relative to a ^{3}He tube, by comparing the number of events measured by the detector and the tube. The ^{3}He tube was placed between the detector and the beam in such a way that all neutrons were captured by the tube. Later on, the tube was removed and the neutron events were counted by the detector under identical measurement conditions, without altering the setup (see Fig. 6.9). Assuming 100 % efficiency for the ^{3}He tube, the measured maximum efficiency was approximately 96 %.

A fission chamber from LND Inc. [157], with ^{235}U (cross section of ∽500 barn) as the neutron-sensitive material and filled with Ar and N gases was utilized to determine the linearity of the detector. The measurement setup is shown in Fig. 6.10. 5 min measurement with 2 cm × 2 cm beam aperture for fission chamber and the detector is plotted in Fig. 6.11 with the attenuated beams, using up to 5 absorbers (1 mm thick, each absorbing 43 % of

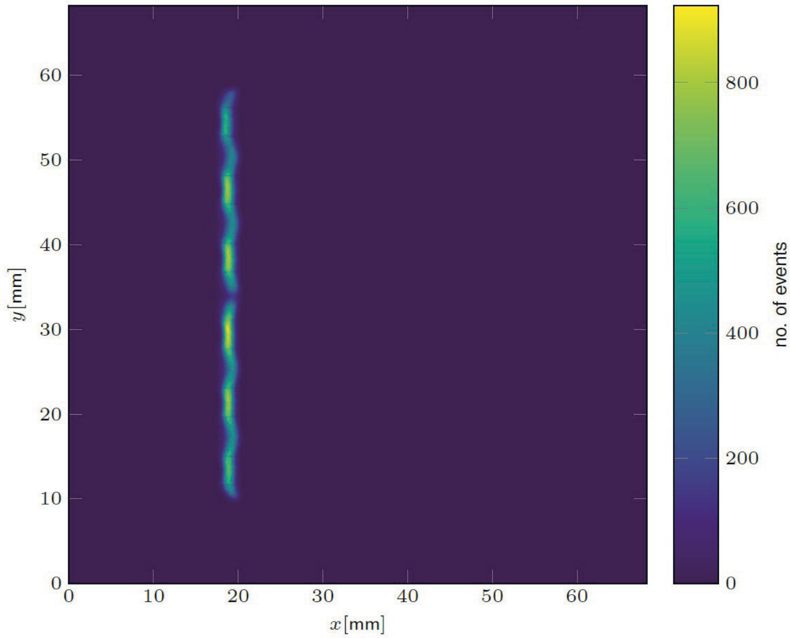

Figure 6.7: Reconstructed image of 1 mm slit aperture.

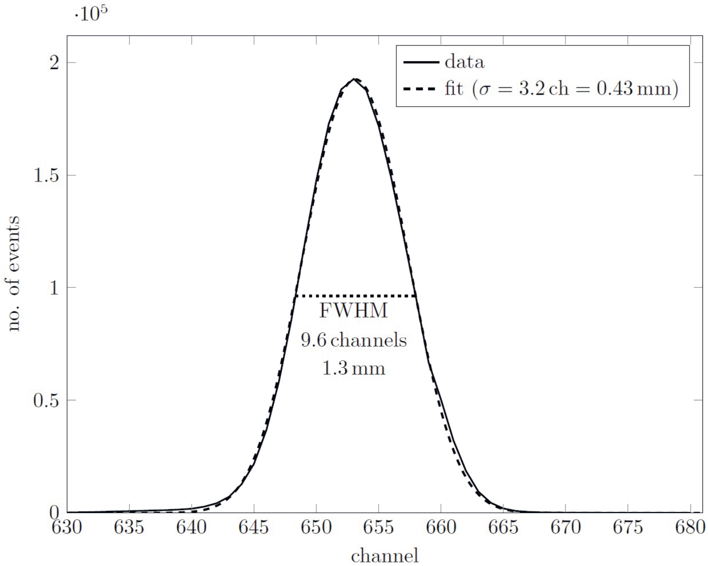

Figure 6.8: Graph showing the projection of counts onto the X-axis during irradiation through a 1 mm slit at V17 instrument in BER-II, Berlin. The data was fitted by a convolution of a Gaussian bell curve with a 1 mm rectangular function. Reprinted with permission from [156].

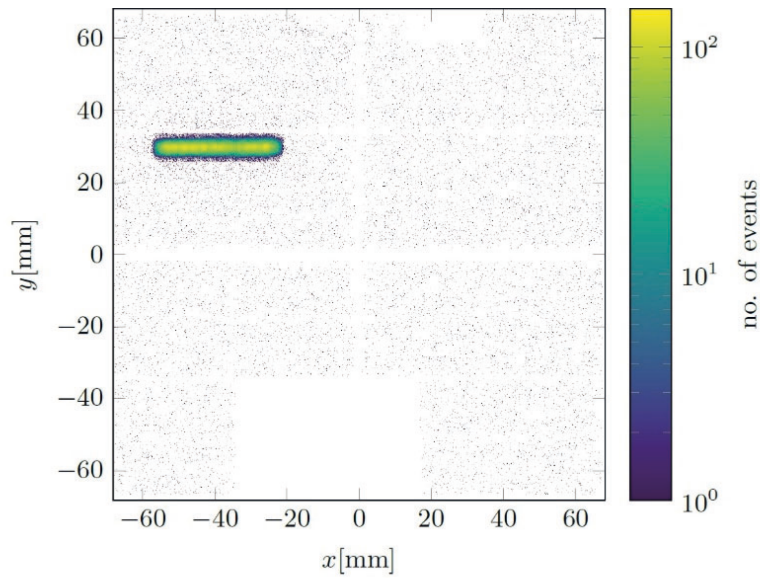

Figure 6.9: Reconstructed image, as seen by the detector, for the efficiency measurement after the ^{3}He tube was removed. Certain area (bottom center) of the detector was offline and did not record any event. Reprinted with permission from [156].

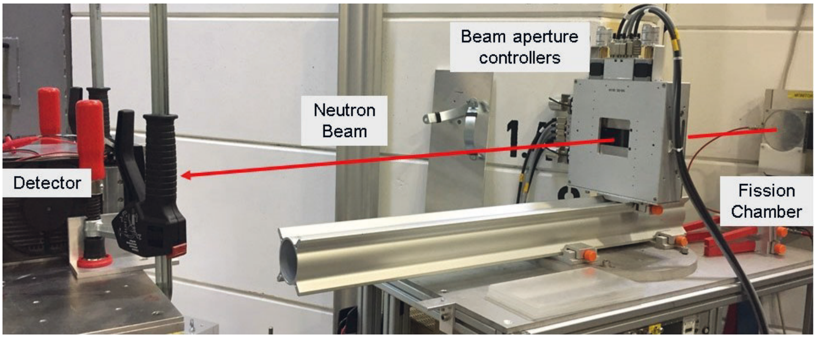

Figure 6.10: Photograph of the set up for measuring the count linearity and count rate of the detector at V17 instrument in BER-II, Berlin.

the neutrons). It shows that the response is proportional up until the highest intensity measurement, which results in count rates of 1.09 kcps/mm^2. This means that the value is the lowest bound and the highest bound of the count rate and linearity can only be determined by testing the detector under a more intense beam.

Furthermore, the detector was tested for its capabilities of differentiating neutrons from gamma rays, normally present as the background in such environments. Although, it was not the focus of the measurements, different gamma sources were placed directly in front of the detector and its response was measured. Fig. 6.12 shows one of the used set-ups for gamma response measurement. The discrimination ratio was expected by comparing the number of detected events to the expected number of incident gamma particles. It was approximated using the formula (6.5.1). Table 6.2 shows the measurement results for the settings that were optimized for neutron detection and not tweaked for gamma discrimination. Hence, the values reported here could be improved by optimizing the specific settings for gamma discrimination.

$$Discrimination\ ratio = \frac{detected\ events}{radioactivity \cdot time \cdot \gamma} \tag{6.5.1}$$

Additionally, an overnight measurement was carried out for assessing the long time homogenity operation. A Plexiglas (polymethylmethacrylate) was placed in front of the beam in order to scatter neutrons isotropically. The detector was placed at an angle so as to avoid the main beam impinging onto the detector. This means that the whole surface of the detector received a homogeneous neutron irradiation. The reconstructed image for the detected

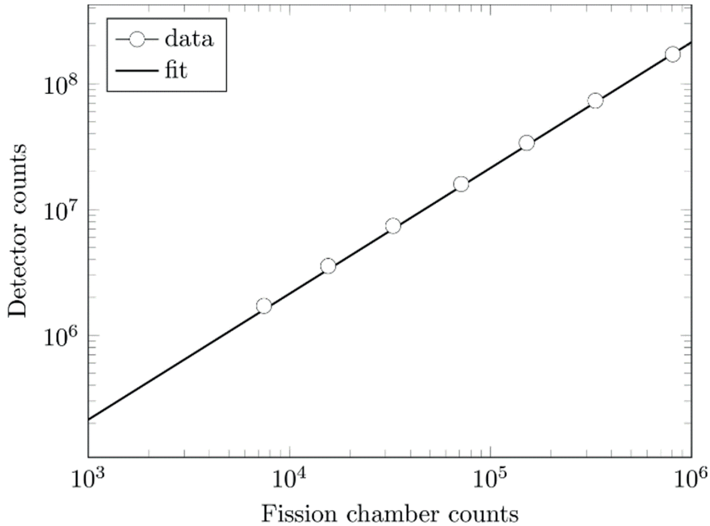

Figure 6.11: Comparison between detector and fission chamber response at V17 instrument in BER-II, Berlin to different neutron beam intensities, including a linear fit. Reprinted with permission from [156].

Figure 6.12: Setup showing Gamma source (wrapped in yellow tape) directly placed in front of the detector to measure the gamma discrimination ratio.

Table 6.2: Three gamma sources placed directly in front of the detector. The values are an approximation as the same threshold setting were used for the neutron measurements.

Isotope	Energy [MeV]	Radioactivity [1×10^5 Bq]	Detector count [cps]	Discrimination factor
^{60}Co	1.17, 1.33	4.7	250	10^{-4}
^{137}Cs	0.662	190	2.1	10^{-6}
^{241}Am	0.059	170	0.2	10^{-7}

Table 6.3: Table showing the comparison of target and achieved specification of the detector prototype with 3.35 Å neutrons.

Item	Detection efficiency	Count rate	Linearity at 1 kcps/mm^2	Position resolution	Gamma discrimination
Target	75 %	0.02 kcps/mm^2	-	1 mm	-
Achieved	96 %$^{\#}$	1.09 kcps/mm^2	100 %	1 mm	$10^{-4\star}$

($^{\#}$relative to ^{3}He-tube. *For ^{60}Co)

neutrons are depicted in Fig. 6.13. Certain areas (bottom center and top right) of the detector were not functional during the measurement, hence no data was recorded. From Fig. 6.13 it can be also seen that there were some air bubbles (bottom right corner and top center), which refracted light from neutron event, warping the outcome of the position reconstruction algorithm. However, it can be concluded that the detector has quite homogeneous response under continuous 8 h operation.

Table 6.3 shows the measured FOM of the detector and its comparison with the goal. For details of the detector´s performance measurement, the reader is referred to [156]. Although the detector's performance exceeded the target, it can still be improved further. An improved design for the SiPM´s tilability, a better cooling system, an efficient light tight cap and durable data connectors would be more beneficial on system level improvement.

Another focus could be on the issue of scalability. As mentioned, the USB 3.0 cables used for data transfer between concentrator board and PC acts as a bottle neck. Thus, other interfaces could be studied to get a data transfer rate higher than 300 MB/s so that the parallel nature of the PDPCs data collection can be fully utilized.

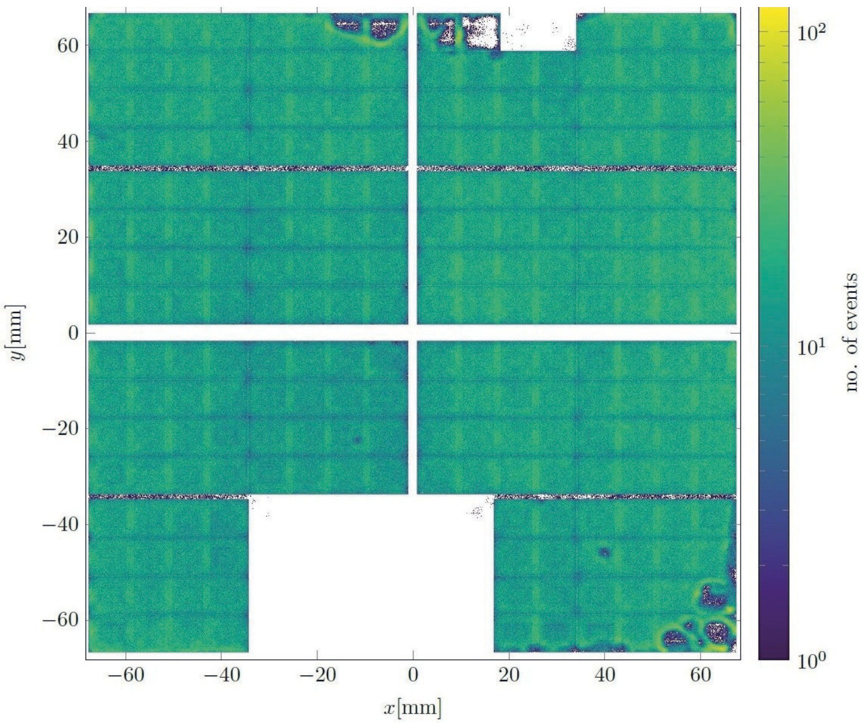

Figure 6.13: Reconstructed image from overnight measurement at V17 instrument in BER-II, Berlin under homogeneous illumination on the whole surface of the detector. Blank area (top right and center bottom) where no data were recorded due to offline pixels, as well as air bubbles (bottom right and top center) are visible.

Chapter 7

Conclusion and Outlook

The main goal of this thesis was to address the question of whether SiPMs are suitable for application in neutron scintillation detectors. The approach towards this research challenge was to study the radiation damage in SiPMs due to cold neutrons and subsequently, to develop a neutron detector prototype based on SiPMs. The radiation hardness was analyzed qualitatively and quantitatively to observe the changes in macroscopic properties of SiPMs. The investigations for PDE of three different (*SensL*, *Hamamatsu* and *Philips*) SiPM technologies after irradiation with cold neutrons, shows an insignificant change in PDE for their life time doses (up to $6 \times 10^{12}\,\mathrm{n/cm^2}$) under SANS experiments. Furthermore, the results of TR for approximately 600 incident photons indicates a nominal change in the same SiPM samples irradiated with neutrons. In addition, it provides a fruitful insight into SiPM applications in neutron TOF experiments.

Another challenge of this work was to reconstruct the position of neutrons with a precision better than 1 mm using data of four pixels (4 mm pixel pitch) only. This was achieved by developing customized algorithms (Least Square and Bayes inversion), and introducing a suitable light guide, i.e. a 1.1 mm thick glass of matching refractive index with the scintillator glass, between the scintillator and SiPM array. The light guide was useful to achieve a certain light distribution (spread of the light across several pixels) across the SiPM surface that was helpful for algorithms in achieving subpixel accuracy by using multiple pixel data. It was demonstrated that the Least Square algorithm was feasible to reach the goal of 1 mm resolution, and that the Bayesian algorithm yields almost identical reconstructed positions as Least Square. However, due to the implementation in Python programming language Bayes inversion suffers from poor speed and therefore was disregarded. Another programming language could be explored to improve the performance of Bayes inversion. Nevertheless, both algorithms give an understanding that data from four pixels are sufficient for reconstruction in these kind of neutron detectors.

A detector prototype with large active area (13.6 cm × 13.6 cm) was developed. It was integrated with digital SiPM (from *Philips*) arrays and 1 mm thick ^{6}Li scintillator glass. The detector was tested at the research reactor BER II of Helmholtz Zentrum Berlin to evaluate its performance. Enumerating the advantages, it is a very compact (see Fig 7.1), convenient for handling (∽18 kg), and efficient (∽96 %, relative to ^{3}He-tube) detector. The promising results of the prototype illustrate its potential to be the state-of-the-art neutron scintillation detector. For reference, the comparison among some of the existing detectors are summarized in Table 7.1. The detector developed in this work is abbreviated as TPP (TREFF PDPC Prototype), highlighted in red and its FOM are interpolated w.r.t. the whole active area.

Figure 7.1: Picture showing the dimensions of the detector prototype developed.

With the above mentioned investigations on radiation hardness of SiPM and the experimental results from the performance of the detector prototype it can be concluded that, SiPMs are not only suitable for cold neutron detection, but also they have great potential to become state-of-the-art additions to advanced neutron detectors.

Although the developed detector prototype has better performance than the target specification, there is still room for improvements. Other statistical reconstruction methods such as maximum likelihood or neural network based approaches could be investigated to explore further enhancement in the spatial resolution. Another possible alternative could be employing a position sensitive SiPM that can provide information of detected photons on µm scale [158] [159]. For example, in a 2.7 mm × 2.7 mm SiPM, a position resolution of 20 µm has been reported [160], which can be assessed for its utilization in neutron scintillation detector for getting the position resolution without any algorithm development. However, integrating these SiPMs in large arrays will be a challenge.

Table 7.1: Comparison of the developed detector prototype (TPP) with some of the existing detectors (data were taken as available on their web portal and true to the best of author knowledge) for a reference.

Detector	Location	Technology	Count rate	Spatial Resolution	Area	Specific count rate
TPP	ZEA-2, Jülich	^{6}Li glass + SiPM	20 Mcps*	1 mm	0.027 m^2	1000 Mcps/m^2
KWS-1	MLZ, Garching	^{6}Li glass + PMT	0.6 Mcps	5.3 mm	0.46 m^2	1.30 Mcps/m^2
KWS-2	MLZ, Garching	^{3}He	2 Mcps	8 mm	1 m^2	2 Mcps/m^2
EXED	HZB, Berlin	^{3}He	20 Mcps	2 mm	0.45 m^2	44.44 Mcps/m^2
D22	ILL, Greenoble	^{3}He	5 Mcps	7 mm	1 m^2	5 Mcps/m^2
TAIKAN	J-PARC, Tokai	Zns/LiF + PMT	0.46 Mcps	0.41 mm	0.05 m^2	0.92 Mcps/m^2

(*The measured count rate was 1.09 kcps/mm^2 and it is interpolated for the whole detector area assuming no data loss)

Additionally, the spatial resolution achieved here is not valid in certain areas of the detector due to the dead space caused by assembling multiple PDPC sensors to cover the large area. This can be observed in Figs. 6.5, and 6.6 as the blank lines in the images. This could be mitigated by joining existing large area analog SiPM arrays or fabrication of a dedicated digital SiPM, provided its availability and feasibility. Employing analog SiPMs could offer flexibility of analyzing raw multiple pixel data and could ease the implementation of reconstruction algorithms. However, it will come with a complexity of front-end electronics involved in readout of analog SiPMs.

Furthermore, as discussed within this study, it is also worth to investigate the annealing phenomenon and its impact on the SiPM´s FOM, which will provide a broader perception to the community for SiPM´s usability under neutron exposure.

Bibliography

[1] D. L. Price and K. Skold, “1. introduction to neutron scattering,” in *Methods in Experimental Physics*, vol. 23, pp. 1–97, Elsevier, 1986.

[2] T. Persons and G. Aloise, “Neutron detectors: Alternatives to using helium-3,” *United States Government Accountability Office GAO-11-753*, 2011.

[3] R. T. Kouzes *et al.*, “Neutron detection alternatives to helium-3 for national security applications,” *Nuclear Instruments and Methods in Physics Research Section A: Accelerators, Spectrometers, Detectors and Associated Equipment*, vol. 623, no. 3, pp. 1035–1045, 2010.

[4] V. Voitovetskii and N. Tolmacheva, “Scintillation glasses with increased light yield for detecting neutrons,” *The Soviet Journal of Atomic Energy*, vol. 10, no. 5, pp. 492–493, 1962.

[5] M. Strauss *et al.*, “2-d position-sensitive scintillation detector for neutrons,” *IEEE Transactions on Nuclear Science*, vol. 28, no. 1, pp. 800–806, 1981.

[6] G. Kemmerling *et al.*, “A new two-dimensional scintillation detector system for small-angle neutron scattering experiments,” *IEEE Transactions on Nuclear Science*, vol. 48, no. 4, pp. 1114–1117, 2001.

[7] S.-i. Takata *et al.*, “The design and q resolution of the small and wide angle neutron scattering instrument (taikan) in j-parc,” in *Proceedings of the 2nd International Symposium on Science at J-PARC—Unlocking the Mysteries of Life, Matter and the Universe*, p. 036020, 2015.

[8] H. Frielinghaus *et al.*, “Kws-1: Small-angle scattering diffractometer,” *Journal of large-scale research facilities JLSRF*, vol. 1, p. 28, 2015.

[9] D. Durini *et al.*, "Evaluation of the dark signal performance of different sipm-technologies under irradiation with cold neutrons," *Nuclear Instruments and Methods in Physics Research Section A: Accelerators, Spectrometers, Detectors and Associated Equipment*, vol. 835, pp. 99–109, 2016.

[10] S. Kumar *et al.*, "Photodetection characterization of sipm technologies for their application in scintillator based neutron detectors," *Journal of Instrumentation*, vol. 13, no. 01, p. C01042, 2018.

[11] H. O. Anger, "Scintillation camera," *Review of Scientific Instruments*, vol. 29, no. 1, pp. 27–33, 1958.

[12] R. Riedel *et al.*, "Design and performance of a large area neutron sensitive anger camera," *Nuclear Instruments and Methods in Physics Research Section A: Accelerators, Spectrometers, Detectors and Associated Equipment*, vol. 794, pp. 224–233, 2015.

[13] J. Chadwick, "The existence of a neutron," *Proceedings of the Royal Society of London. Series A, Containing Papers of a Mathematical and Physical Character*, vol. 136, no. 830, pp. 692–708, 1932.

[14] A. Peurrung, "Recent developments in neutron detection," *Nuclear Instruments and Methods in Physics Research Section A: Accelerators, Spectrometers, Detectors and Associated Equipment*, vol. 443, no. 2, pp. 400 – 415, 2000.

[15] "Neutron-scattering-materials-research-for-modern-life." `https://www.isis.stfc.ac.uk/Pages/Neutron-Scattering-Materials-research-for-modern-life.aspx`. Accessed: June 2020.

[16] G. F. Knoll, "Slow neutrons detection method," in *Radiation detection and measurement*, pp. 519–539, John Wiley & Sons, 2010.

[17] "6-lithium glass bespoke to your application." `https://scintacor.com/products/6-lithium-glass/`. Accessed: June 2020.

[18] D. Harris, C. Duffil, and L. Wraight, "Scintillation counters for neutron scattering experiments," in *Inelastic Scattering of Neutrons in Solids and Liquids. VI Proceedings of the Symposium on Inelastic Scattering of Neurons in Solids and Liquids*, 1963.

[19] A. Einstein, “On a heuristic point of view about the creation and conversion of light,” *Annalen der Physik*, vol. 17, no. 6, pp. 132–148, 1905.

[20] H. Iams and B. Salzberg, “The secondary emission phototube,” *Proceedings of the Institute of Radio Engineers*, vol. 23, no. 1, pp. 55–64, 1935.

[21] V. Golovin, “Avalanche photodetector, russian agency for patents and trademarks, patent no 2142175,” 1998.

[22] Z. Sadygov, “Avalanche photodetector, russian agency for patents and trademarks, patent no. 2102820,” 1998.

[23] P. Buzhan *et al.*, “The advanced study of silicon photomultiplier,” in *Advanced Technology and Particle Physics*, pp. 717–728, World Scientific, 2002.

[24] V. Saveliev, “The recent development and study of silicon photomultiplier,” *Nuclear Instruments and Methods in Physics Research Section A: Accelerators, Spectrometers, Detectors and Associated Equipment*, vol. 535, no. 1-2, pp. 528–532, 2004.

[25] C. J. Stapels *et al.*, “Characterization of a cmos geiger photodiode pixel,” *IEEE Transactions on Electron Devices*, vol. 53, no. 4, pp. 631–635, 2006.

[26] C. Piemonte and A. Gola, “Overview on the main parameters and technology of modern silicon photomultipliers,” *Nuclear Instruments and Methods in Physics Research Section A: Accelerators, Spectrometers, Detectors and Associated Equipment*, vol. 926, pp. 2–15, 2019.

[27] D. Renker and E. Lorenz, “Advances in solid state photon detectors,” *Journal of Instrumentation*, vol. 4, no. 04, p. P04004, 2009.

[28] P. P. Webb, R. J. McIntyre, and J. Conradi, “Properties of avalanche photodiodes,” *RCA Review*, vol. 35, pp. 234–278, 1974.

[29] R. J. McIntyre, “The distribution of gains in uniformly multiplying avalanche photodiodes: Theory,” *IEEE Transactions on Electron Devices*, vol. 19, no. 6, pp. 703–713, 1972.

[30] M. Atac *et al.*, "Scintillating fiber tracking for the ssc using visible light photon counters," *Nuclear Instruments and Methods in Physics Research Section A: Accelerators, Spectrometers, Detectors and Associated Equipment*, vol. 314, no. 1, pp. 56–62, 1992.

[31] R. J. McIntyre, "Theory of microplasma instability in silicon," *Journal of Applied Physics*, vol. 32, no. 6, pp. 983–995, 1961.

[32] R. H. Haitz, "Model for the electrical behavior of a microplasma," *Journal of Applied Physics*, vol. 35, no. 5, pp. 1370–1376, 1964.

[33] E. Rutherford and H. Geiger, "An electrical method of counting the number of α-particles from radio-active substances," *Proceedings of the Royal Society of London. Series A, Containing Papers of a Mathematical and Physical Character*, vol. 81, no. 546, pp. 141–161, 1908.

[34] S. Cova, A. Longoni, and A. Andreoni, "Towards picosecond resolution with single-photon avalanche diodes," *Review of Scientific Instruments*, vol. 52, no. 3, pp. 408–412, 1981.

[35] K. T. Son and C. C. Lee, "Multiple-target laser rangefinding receiver using a silicon photomultiplier array," *IEEE Transactions on Instrumentation and Measurement*, vol. 59, no. 11, pp. 3005–3011, 2010.

[36] P. D. Townsend, J. Rarity, and P. Tapster, "Single photon interference in 10 km long optical fibre interferometer," *Electronics Letters*, vol. 29, no. 7, pp. 634–635, 1993.

[37] N. Otte *et al.*, "The sipm—a new photon detector for pet," *Nuclear Physics B-Proceedings Supplements*, vol. 150, pp. 417–420, 2006.

[38] S. España *et al.*, "Performance evaluation of sipm photodetectors for pet imaging in the presence of magnetic fields," *Nuclear Instruments and Methods in Physics Research Section A: Accelerators, Spectrometers, Detectors and Associated Equipment*, vol. 613, no. 2, pp. 308–316, 2010.

[39] N. Otte *et al.*, "The potential of sipm as photon detector in astroparticle physics experiments like magic and euso," *Nuclear Physics B-Proceedings Supplements*, vol. 150, pp. 144–149, 2006.

[40] C. Bruschini *et al.*, "Single-photon avalanche diode imagers in biophotonics: review and outlook," *Light: Science & Applications*, vol. 8, no. 1, pp. 1–28, 2019.

[41] S. M. Sze and K. K. Ng, *Physics of semiconductor devices*. John wiley & sons, 2006.

[42] H. Spieler, "Signal formation and acquisition," in *Semiconductor detector systems*, vol. 12, pp. 43–102, Oxford university press, 2005.

[43] P. Antognetti, S. Cova, and A. Longoni, "A study of the operation and performances of an avalanche diode as a single-photon detector," tech. rep., 1975.

[44] S. Cova *et al.*, "Avalanche photodiodes and quenching circuits for single-photon detection," *Applied optics*, vol. 35, no. 12, pp. 1956–1976, 1996.

[45] P. Webb and R. McIntyre, "Single photon detection with avalanche photodiodes," in *Bulletin of the American Physical Society*, vol. 15, p. 813, 1970.

[46] R. H. Haitz, "Mechanisms contributing to the noise pulse rate of avalanche diodes," *Journal of Applied Physics*, vol. 36, no. 10, pp. 3123–3131, 1965.

[47] C. Piemonte, "A new silicon photomultiplier structure for blue light detection," *Nuclear Instruments and Methods in Physics Research Section A: Accelerators, Spectrometers, Detectors and Associated Equipment*, vol. 568, no. 1, pp. 224 – 232, 2006.

[48] N. Dinu, "Silicon photomultipliers," in *Photodetectors* (B. Nabet, ed.), ch. 8, pp. 245–294, Elsevier, 2016.

[49] W. Ootani, "Sipm: Status and perspectives, special workshop on photon detection with mpgds, june 10-11, 2015 cern." `https://indico.cern.ch/event/392833/contributions/1829473/attachments/785875/1077253/SiPMReview_OotaniRD51.pdf`. Accessed: June 2020.

[50] "Spad by technology." `http://www.micro-photon-devices.com/Products/SPAD-by-Technology`. Accessed: June 2020.

[51] S. Gnecchi *et al.*, "First results from cmos-integrated spad and sipm," in *Proc. Int. Symp. Med. Imag. Conf.*, 2017.

[52] J. A. Richardson, L. A. Grant, and R. K. Henderson, "Low dark count single-photon avalanche diode structure compatible with standard nanometer scale cmos technology," *IEEE Photonics Technology Letters*, vol. 21, no. 14, pp. 1020–1022, 2009.

[53] E. Charbon, H.-J. Yoon, and Y. Maruyama, "A geiger mode apd fabricated in standard 65nm cmos technology," in *2013 IEEE International Electron Devices Meeting*, pp. 27–5, IEEE, 2013.

[54] D. Durini *et al.*, "Silicon based single-photon avalanche diode (spad) technology for low-light and high-speed applications," in *Photodetectors* (B. Nabet, ed.), ch. 11, pp. 345–371, Elsevier, 2016.

[55] B. F. Aull *et al.*, "Geiger-mode avalanche photodiodes for three-dimensional imaging," *Lincoln Laboratory Journal*, vol. 13, no. 2, pp. 335–349, 2002.

[56] A. Rochas *et al.*, "Low-noise silicon avalanche photodiodes fabricated in conventional cmos technologies," *IEEE Transactions on Electron Devices*, vol. 49, no. 3, pp. 387–394, 2002.

[57] G.-F. D. Betta *et al.*, "Avalanche photodiodes in submicron cmos technologies for high-sensitivity imaging," in *Advances in Photodiodes* (G. F. D. Betta, ed.), ch. 11, IntechOpen, 2011.

[58] Y. Zou *et al.*, "Planar cmos analog sipms: Design, modeling, and characterization," *Journal of Modern Optics*, vol. 62, no. 20, pp. 1693–1702, 2015.

[59] N. D'Ascenzo *et al.*, "A novel high photon detection efficiency silicon photomultiplier with shallow junction in 350 nm cmos," *IEEE Electron Device Letters*, vol. 40, no. 9, pp. 1471–1474, 2019.

[60] N. D'Ascenzo, X. Zhang, and Q. Xie, "Application of cmos technology to silicon photomultiplier sensors," *Sensors*, vol. 17, no. 10, p. 2204, 2017.

[61] C. Niclass *et al.*, "A single photon avalanche diode implemented in 130-nm cmos technology," *IEEE Journal of selected topics in quantum electronics*, vol. 13, no. 4, pp. 863–869, 2007.

[62] E. A. Webster, L. A. Grant, and R. K. Henderson, “A high-performance single-photon avalanche diode in 130-nm cmos imaging technology,” *IEEE Electron Device Letters*, vol. 33, no. 11, pp. 1589–1591, 2012.

[63] M. A. Karami, H.-J. Yoon, and E. Charbon, “Single-photon avalanche diodes in sub-100nm standard cmos technologies,” in *Proc. Intl. Image Sensor Workshop (IISW)*, no. CONF, 2011.

[64] M.-J. Lee, H. Rucker, and W.-Y. Choi, “Effects of guard-ring structures on the performance of silicon avalanche photodetectors fabricated with standard cmos technology,” *IEEE Electron Device Letters*, vol. 33, no. 1, pp. 80–82, 2012.

[65] M. M. Vignetti *et al.*, “Design guidelines for the integration of geiger-mode avalanche diodes in standard cmos technologies,” *Microelectronics Journal*, vol. 46, no. 10, pp. 900–910, 2015.

[66] D. Durini *et al.*, “Backspad–back-side illuminated single-photon avalanche diodes: concept and preliminary performances,” *Proc. NSS/MIC*, pp. 1–2, 2012.

[67] W.-S. Choong and S. E. Holland, “Back-side readout silicon photomultiplier,” *IEEE Transactions on Electron Devices*, vol. 59, no. 8, pp. 2187–2191, 2012.

[68] G. Jegannathan, H. Ingelberts, and M. Kuijk, “Current-assisted single photon avalanche diode (caspad) fabricated in 350 nm conventional cmos,” *Applied Sciences*, vol. 10, no. 6, p. 2155, 2020.

[69] R. S. Patti, “Three-dimensional integrated circuits and the future of system-on-chip designs,” *Proceedings of the IEEE*, vol. 94, no. 6, pp. 1214–1224, 2006.

[70] B. Aull, “Geiger-mode avalanche photodiode arrays integrated to all-digital cmos circuits,” *Sensors*, vol. 16, no. 4, p. 495, 2016.

[71] M.-J. Lee and E. Charbon, “Progress in single-photon avalanche diode image sensors in standard CMOS: From two-dimensional monolithic to three-dimensional-stacked technology,” *Japanese Journal of Applied Physics*, vol. 57, p. 1002A3, sep 2018.

[72] M. J. Lee *et al.*, "High-performance back-illuminated 3d-stacked single-photon avalanche diode implemented in 45 nm cmos technology," *IEEE J. Selected Topics in Quantum Electronics*, vol. 24, no. 6, p. 3801809, 2018.

[73] J. M. Pavia *et al.*, "A 1× 400 backside-illuminated spad sensor with 49.7 ps resolution, 30 pj/sample tdcs fabricated in 3d cmos technology for near-infrared optical tomography," *IEEE Journal of Solid-State Circuits*, vol. 50, no. 10, pp. 2406–2418, 2015.

[74] K. K. Ryu *et al.*, "Rapid prototyping of single-photon-sensitive backside-illuminated silicon avalanche photodiode arrays," in *Image Sensing Technologies: Materials, Devices, Systems, and Applications VI*, vol. 10980, p. 109800L, International Society for Optics and Photonics, 2019.

[75] B.-L. Bérubé *et al.*, "Implementation study of single photon avalanche diodes (spad) in 0.8 um hv cmos technology," *IEEE Transactions on Nuclear Science*, vol. 62, no. 3, pp. 710–718, 2015.

[76] F. Nolet *et al.*, "A 2d proof of principle towards a 3d digital sipm in hv cmos with low output capacitance," *IEEE Transactions on Nuclear Science*, vol. 63, no. 4, pp. 2293–2299, 2016.

[77] M. M. Vignetti *et al.*, "Simulation study of a novel 3d spad pixel in an advanced fd-soi technology," *Solid-State Electronics*, vol. 128, pp. 163–171, 2017.

[78] T. C. de Albuquerque *et al.*, "Indirect avalanche event detection of single photon avalanche diode implemented in cmos fdsoi technology," *Solid-State Electronics*, vol. 163, p. 107636, 2020.

[79] S. Mandai and E. Charbon, "A 4 × 4 × 416 digital SiPM array with 192 TDCs for multiple high-resolution timestamp acquisition," *Journal of Instrumentation*, vol. 8, pp. P05024–P05024, may 2013.

[80] N. D'Ascenzo *et al.*, "The digital silicon photomultiplier," *Optoelectronics: Materials and Devices*, p. 463, 2015.

[81] D. R. Schaart *et al.*, "Advances in digital sipms and their application in biomedical imaging," *Nuclear Instruments and Methods in Physics Research Section A: Accelerators, Spectrometers, Detectors and Associated Equipment*, vol. 809, pp. 31–52, 2016.

[82] T. Frach *et al.*, "The digital silicon photomultiplier — principle of operation and intrinsic detector performance," in *IEEE Nuclear Science Symposium Conference Record (NSS/MIC)*, pp. 1959–1965, Oct 2009.

[83] C. Degenhardt *et al.*, "Arrays of digital silicon photomultipliers — intrinsic performance and application to scintillator readout," in *IEEE Nuclear Science Symposuim Medical Imaging Conference*, pp. 1954–1956, Oct 2010.

[84] R. Klanner, "Characterisation of sipms," *Nuclear Instruments and Methods in Physics Research Section A: Accelerators, Spectrometers, Detectors and Associated Equipment*, vol. 926, pp. 36–56, 2019.

[85] S. M. Sze, *Semiconductor devices: physics and technology.* John wiley & sons, 2008.

[86] K. McKay, "Avalanche breakdown in silicon," *Physical Review*, vol. 94, no. 4, p. 877, 1954.

[87] J. L. Moll, *Physics of semiconductors.* McGraw-Hill, 1964.

[88] N. Dinu, A. Nagai, and A. Para, "Breakdown voltage and triggering probability of sipm from iv curves at different temperatures," *Nuclear Instruments and Methods in Physics Research Section A: Accelerators, Spectrometers, Detectors and Associated Equipment*, vol. 845, pp. 64–68, 2017.

[89] V. Chmill *et al.*, "Study of the breakdown voltage of sipms," *Nuclear Instruments and Methods in Physics Research Section A: Accelerators, Spectrometers, Detectors and Associated Equipment*, vol. 845, pp. 56–59, 2017.

[90] R. McIntyre, "Multiplication noise in uniform avalanche diodes," *IEEE Transactions on Electron Devices*, no. 1, pp. 164–168, 1966.

[91] F. Zappa *et al.*, "Principles and features of single-photon avalanche diode arrays," *Sensors and Actuators A: Physical*, vol. 140, no. 1, pp. 103–112, 2007.

[92] S. Cova *et al.*, "Evolution and prospects for single-photon avalanche diodes and quenching circuits," *Journal of Modern Optics*, vol. 51, no. 9-10, pp. 1267–1288, 2004.

[93] A. Lacaita *et al.*, "Observation of avalanche propagation by multiplication assisted diffusion in p-n junctions," *Applied Physics Letters*, vol. 57, no. 5, pp. 489–491, 1990.

[94] A. Chynoweth and K. McKay, “Photon emission from avalanche breakdown in silicon,” *Physical Review*, vol. 102, no. 2, p. 369, 1956.

[95] A. L. Lacaita *et al.*, “On the bremsstrahlung origin of hot-carrier-induced photons in silicon devices,” *IEEE Transactions on Electron Devices*, vol. 40, no. 3, pp. 577–582, 1993.

[96] V. Saveliev, “Silicon photomultiplier-new era of photon detection,” *Advances in optical and photonic devices*, p. 352, 2010.

[97] W. Tsang, *Semiconductors and semimetals*. Academic Press, 1985.

[98] W. Grant, “Electron and hole ionization rates in epitaxial silicon at high electric fields,” *Solid-State Electronics*, vol. 16, no. 10, pp. 1189–1203, 1973.

[99] G. Gallina *et al.*, “Characterization of sipm avalanche triggering probabilities,” *IEEE Transactions on Electron Devices*, vol. 66, no. 10, pp. 4228–4234, 2019.

[100] R. Wunstorf, *Systematische Untersuchungen zur Strahlenresistenz von Silizium-Detektoren für die Verwendung in Hochenergiephysik-Experimenten*. PhD thesis, Physics Dept., Univ. of Hamburg, Germany, 1992.

[101] G. Lutz, *Semiconductor radiation detectors*, vol. 40. Springer, 1999.

[102] G. Lindström, “Radiation damage in silicon detectors,” *Nuclear Instruments and Methods in Physics Research Section A: Accelerators, Spectrometers, Detectors and Associated Equipment*, vol. 512, no. 1-2, pp. 30–43, 2003.

[103] H. Spieler, “Radiation effects,” in *Semiconductor detector systems*, vol. 12, pp. 277–309, Oxford university press, 2005.

[104] F. Hartmann, “Radiation damage in silicon detector devices,” in *Evolution of Silicon Sensor Technology in Particle Physics*, pp. 135–166, Springer, 2017.

[105] M. Moll, *Radiation damage in silicon particle detectors*. PhD thesis, Physics Dept., Univ. of Hamburg, Germany, 1999.

[106] “The rose collaboration at cern.” `https://rd48.web.cern.ch/Default.html`. Accessed: June 2020.

[107] E. Garutti and Y. Musienko, "Radiation damage of sipms," *Nuclear Instruments and Methods in Physics Research Section A: Accelerators, Spectrometers, Detectors and Associated Equipment*, 2019.

[108] M. Moll, "Displacement damage in silicon detectors for high energy physics," *IEEE Transactions on Nuclear Science*, vol. 65, no. 8, pp. 1561–1582, 2018.

[109] C. Inguimbert *et al.*, ""effective niel" in silicon: Calculation using molecular dynamics simulation results," *IEEE Transactions on Nuclear Science*, vol. 57, no. 4, pp. 1915–1923, 2010.

[110] S. R. Messenger *et al.*, "Correlation of telemetered solar array data with particle detector data on gps spacecraft," *IEEE Transactions on Nuclear Science*, vol. 58, no. 6, pp. 3118–3125, 2011.

[111] C. Inguimbert and S. Messenger, "Equivalent displacement damage dose for on-orbit space applications," *IEEE Transactions on Nuclear Science*, vol. 59, no. 6, pp. 3117–3125, 2012.

[112] I. Nakamura, "Radiation damage of pixelated photon detector by neutron irradiation," *Nuclear Instruments and Methods in Physics Research Section A: Accelerators, Spectrometers, Detectors and Associated Equipment*, vol. 610, no. 1, pp. 110–113, 2009.

[113] M. Angelone *et al.*, "Silicon photo-multiplier radiation hardness tests with a beam controlled neutron source," *Nuclear Instruments and Methods in Physics Research Section A: Accelerators, Spectrometers, Detectors and Associated Equipment*, vol. 623, no. 3, pp. 921–926, 2010.

[114] M. Andreotti *et al.*, "Radiation damage effects in silicon photo-multipliers," in *2013 IEEE Nuclear Science Symposium and Medical Imaging Conference (2013 NSS/MIC)*, pp. 1–4, IEEE, 2013.

[115] G. Lindstrom *et al.*, "Radiation hard silicon detectors—developments by the rd48 (rose) collaboration," *Nuclear Instruments and Methods in Physics Research Section A: Accelerators, Spectrometers, Detectors and Associated Equipment*, vol. 466, no. 2, pp. 308 – 326, 2001. 4th Int. Symp. on Development and Application of Semiconductor Tracking Detectors.

[116] "Radiation hard semiconductor devices for very high luminosity colliders." `https://rd50.web.cern.ch/`. Accessed: June 2020.

[117] Y. Musienko and A. Karneyeu, "Investigation of avalanche photodiodes after irradiation with neutrons up to 5 x 10^{14} n/cm˜2," *PoS*, p. 073, 2015.

[118] M. C. Vignali *et al.*, "Neutron irradiation effect on sipms up to neq = 5 × 1014 cm2," *Nuclear Instruments and Methods in Physics Research Section A: Accelerators, Spectrometers, Detectors and Associated Equipment*, vol. 912, pp. 137 – 139, 2018.

[119] P. Cattaneo *et al.*, "Radiation hardness tests with neutron flux on different silicon photomultiplier devices," *Journal of Instrumentation*, vol. 12, pp. C07012–C07012, jul.

[120] V. Kushpil *et al.*, "Neutron irradiation study of silicon photomultipliers from different vendors," *Nuclear Instruments and Methods in Physics Research Section A: Accelerators, Spectrometers, Detectors and Associated Equipment*, vol. 845, pp. 114–117, 2017.

[121] J. Cleland, K. Lark-Horovitz, and J. Pigg, "Transmutation-produced germanium semiconductors," *Physical Review*, vol. 78, no. 6, p. 814, 1950.

[122] R. Young *et al.*, "Radiation damage in neutron transmutation doped silicon: Electrical property studies," *Journal of Applied Physics*, vol. 49, no. 9, pp. 4752–4760, 1978.

[123] E. Martinenghi *et al.*, "Spectrally resolved single-photon timing of silicon photomultipliers for time-domain diffuse spectroscopy," *IEEE Photonics Journal*, vol. 7, no. 4, pp. 1–12, 2015.

[124] J. Ollivier, H. Mutka, and L. Didier, "The new cold neutron time-of-flight spectrometer in5," *Neutron News*, vol. 21, no. 2, pp. 22–25, 2010.

[125] W. Lohstroh and Z. Evenson, "Toftof: Cold neutron time-of-flight spectrometer," *Journal of large-scale research facilities JLSRF*, vol. 1, p. 15, 2015.

[126] S. Kumar *et al.*, "Timing resolution of sipm technologies before and after neutron irradiation," *Journal of Instrumentation*, vol. 15, no. 01, p. C01023, 2020.

[127] J. W. Cates, S. Gundacker, E. Auffray, P. Lecoq, and C. S. Levin, "Improved single photon time resolution for analog SiPMs with front end readout that reduces influence of electronic noise," *Physics in Medicine & Biology*, vol. 63, p. 185022, sep 2018.

[128] F. Acerbi, A. Gola, A. Ferri, N. Zorzi, G. Paternoster, and C. Piemonte, "Analysis of transit time spread on FBK silicon photomultipliers," *Journal of Instrumentation*, vol. 10, pp. P07014–P07014, jul 2015.

[129] V. Puill *et al.*, "Single photoelectron timing resolution of sipm as a function of the bias voltage, the wavelength and the temperature," *Nuclear Instruments and Methods in Physics Research Section A: Accelerators, Spectrometers, Detectors and Associated Equipment*, vol. 695, pp. 354–358, 2012.

[130] M. Nemallapudi *et al.*, "Single photon time resolution of state of the art sipms," *Journal of Instrumentation*, vol. 11, no. 10, p. P10016, 2016.

[131] Y. Qiang *et al.*, "Radiation hardness tests of sipms for the jlab hall d barrel calorimeter," *Nuclear Instruments and Methods in Physics Research Section A: Accelerators, Spectrometers, Detectors and Associated Equipment*, vol. 698, pp. 234–241, 2013.

[132] T. Tsang *et al.*, "Neutron radiation damage and recovery studies of sipms," *Journal of Instrumentation*, vol. 11, no. 12, p. P12002, 2016.

[133] M. Cordelli *et al.*, "Neutron irradiation test of hamamatsu, sensl and advansid uv-extended sipms," *Journal of Instrumentation*, vol. 13, no. 03, p. T03005, 2018.

[134] A. Heering *et al.*, "Low temperature characteristics of sipms after very high neutron irradiation," *Nuclear Instruments and Methods in Physics Research Section A: Accelerators, Spectrometers, Detectors and Associated Equipment*, vol. 936, pp. 671–673, 2019.

[135] H. Nöldgen *et al.*, "Read-out electronics for digital silicon photomultiplier modules," in *2013 IEEE Nuclear Science Symposium and Medical Imaging Conference (2013 NSS/MIC)*, no. FZJ-2015-00643, Zentralinstitut für Elektronik, 2013.

[136] S. Agostinelli *et al.*, "Geant4—a simulation toolkit," *Nuclear instruments and methods in physics research section A: Accelerators, Spectrometers, Detectors and Associated Equipment*, vol. 506, no. 3, pp. 250–303, 2003.

[137] N. Metropolis and S. Ulam, "The monte carlo method," *Journal of the American statistical association*, vol. 44, no. 247, pp. 335–341, 1949.

[138] J. Allison *et al.*, "Recent developments in geant4," *Nuclear Instruments and Methods in Physics Research Section A: Accelerators, Spectrometers, Detectors and Associated Equipment*, vol. 835, pp. 186–225, 2016.

[139] S. Kumar *et al.*, "Development of a solid-state position sensitive neutron detector prototype based on 6li-glass scintillator and digital sipm arrays," *Nuclear Instruments and Methods in Physics Research Section A: Accelerators, Spectrometers, Detectors and Associated Equipment*, vol. 954, p. 161697, 2020.

[140] R. Brun and F. Rademakers, "Root—an object oriented data analysis framework," *Nuclear Instruments and Methods in Physics Research Section A: Accelerators, Spectrometers, Detectors and Associated Equipment*, vol. 389, no. 1-2, pp. 81–86, 1997.

[141] A. Morozov *et al.*, "Ants2 package: simulation and experimental data processing for anger camera type detectors," *Journal of Instrumentation*, vol. 11, no. 04, p. P04022, 2016.

[142] R. Brun, A. Gheata, and M. Gheata, "The root geometry package," *Nuclear Instruments and Methods in Physics Research Section A: Accelerators, Spectrometers, Detectors and Associated Equipment*, vol. 502, no. 2-3, pp. 676–680, 2003.

[143] "Vitralit: Uv and light curing adhesives." `https://www.panacol.com/products/adhesive/vitralit/`. Accessed: June 2020.

[144] J. Seemann, "Design, implementierung und test einer teilautomatisierten kalibrierung eines verfahrens zur verbesserung der ortsauflösung bei einem neutronendetektor," bachelor's thesis, Fachhochschule Aachen, Campus Jülich, 2019.

[145] G. Finocchiaro, A. Aloisio, S. Baccaro, P. Branchini, S. Cavaliere, C. Cecchi, A. Cemmi, G. Corradi, E. De Lucia, G. De Nardo, *et al.*, "Radiation hardness and stability of optical coupling materials for belleii electromagnetic calorimeter," *Proc. of Science (TIPP2014)*, pp. 255–259, 2014.

[146] O. Pooth, T. Radermacher, S. Weingarten, and L. Weinstock, "Scintillator tiles read out with silicon photomultipliers," *Journal of Instrumentation*, vol. 10, no. 10, p. T10007, 2015.

[147] "Eljen silicon grease." `https://eljentechnology.com/products/accessories/ej-550-ej-552`. Accessed: June 2020.

[148] "Detector assembly materials." `https://www.crystals.saint-gobain.com/document/bc630-silicone-grease-sdspdf`. Accessed: June 2020.

[149] "Deector test station v17 at ber ii, berlin." `https://www.helmholtz-berlin.de/forschung/oe/em/transport-phenomena/neutronmethods/detektorlabor_en.html`. Accessed: June 2020.

[150] H. M.-L. Zentrum, "Treff: Reflectometer and instrument compo-nent test beamline at mlz," *Journal of large-scale research facilities*, vol. 3, p. A121, 2017.

[151] S. Kumar, M. Herzkamp, and S. van Waasen, "Sipm-based neutron detector design: validation of geant4 simulations," in *Hard X-Ray, Gamma-Ray, and Neutron Detector Physics XXI*, vol. 11114, p. 111140R, International Society for Optics and Photonics, 2019.

[152] S. Kumar, M. Herzkamp, and S. van Waasen, "Nonlinearity simulation of digital sipm response for inhomogeneous light," *IEEE Transactions on Nuclear Science*, vol. 68, no. 3, pp. 354–358, 2021.

[153] "Fann: Fast artificial neural network library." `http://leenissen.dk/fann/wp/`. Accessed: June 2020.

[154] I. Shilon *et al.*, "Application of deep learning methods to analysis of imaging atmospheric cherenkov telescopes data," *Astroparticle Physics*, vol. 105, pp. 44 – 53, 2019.

[155] H. T. van Dam *et al.*, "Improved nearest neighbor methods for gamma photon interaction position determination in monolithic scintillator pet detectors," *IEEE Transactions on Nuclear Science*, vol. 58, no. 5, pp. 2139–2147, 2011.

[156] S. Kumar *et al.*, "Performance of a position-sensitive neutron scintillation detector based on silicon photomultipliers," *IEEE Transactions on Nuclear Science*, vol. 67, no. 6, pp. 1169–1174, 2020.

[157] "Fission chamber for neutron detector." `https://www.lndinc.com/products/neutron-detectors/fission-chambers/3003`. Accessed: June 2020.

[158] M. McClish *et al.*, "Performance measurements from lyso scintillators coupled to a cmos position sensitive sspm detector," *Nuclear Instruments and Methods in Physics Research Section A: Accelerators, Spectrometers, Detectors and Associated Equipment*, vol. 652, no. 1, pp. 264–267, 2011.

[159] P. Dokhale *et al.*, "Imaging and timing performance of 1 cm x 1 cm position-sensitive solid-state photomultiplier," *Journal of Instrumentation*, vol. 8, pp. C02033–C02033, feb 2013.

[160] T. Zhao *et al.*, "New distortion correction algorithm for two-dimensional tetra-lateral position-sensitive silicon photomultiplier," *IEEE Electron Device Letters*, vol. 38, no. 2, pp. 228–231, 2017.

List of Publications

Articles:

- **S. Kumar**, M. Herzkamp, and S. van Waasen, “Non-linearity simulation of digital SiPM response for In-homogeneous light,” *IEEE Transactions on Nuclear Science , vol. 68, no. 3, pp. 354–358, 2021.*

- **S. Kumar**, M. Herzkamp, C. Degenhardt, J. Seemann, E. Vezhlev, and S. van Waasen, “Performance of a position-sensitive neutron scintillation detector based on silicon photomultipliers,” *IEEE Transactions on Nuclear Science, vol. 67, no. 6, pp. 1169–1174, 2020.*

- **S. Kumar**, M. Herzkamp, D. Durini, H. Noeldgen, and S. van Waasen, “Development of a solid-state position sensitive neutron detector prototype based on 6li-glass scnitillator and digital sipm arrays,” *Nuclear Instruments and Methods in Physics Research Section A: Accelerators, Spectrometers, Detectors and Associated Equipment, vol. 954, p. 161697, 2020.*

- **S. Kumar**, L. Niraula, D. Arutinov, A. Dalla Mora, and S. Van Waasen, “Timing resolution of SiPM technologies before and after neutron irradiation,” *Journal of Instrumentation, vol. 15, no. 01, p. C01023, 2020.*

- **S. Kumar**, M. Herzkamp, and S. van Waasen, “SiPM-based neutron detector design: validation of geant4 simulations,” in *Hard X-Ray, Gamma-Ray, and Neutron Detector Physics XXI, vol. 11114, p. 111140R, International Society for Optics and Photonics, 2019.*

- **S. Kumar**, D. Durini, C. Degenhardt, and S. van Waasen, “Photodetection characterization of SiPM technologies for their application in scintillator based neutron detectors," *Journal of Instrumentation, vol. 13, no. 01, p. C01042, 2018.*

International Conference Presentations:

- **S. Kumar**, M. Herzkamp, C. Degenhardt, S. van Waasen, "Application of Silicon Photomultipliers in neutron detection", (Poster) *International SPAD Sensor Workshop*, Online, June 2020

- **S. Kumar**, M. Herzkamp, S. van Waasen, "Performance of a position sensitive neutron detector based on Silicon Photomultipliers", (Poster) *IEEE Nuclear Science Symposium Medical Imaging Conference*, Manchester, UK, Oct. 2019

- **S. Kumar**, M. Herzkamp, S. van Waasen, "SiPM based neutron detector design: validation of Geant4 simulations", (Talk) *SPIE Optical Engineering + Applications*, San Diego, USA, Aug. 2019

- **S. Kumar**, L. Niraula, M. Herzkamp, D. Arutinov, S. van Waasen, "Timing resolution of SiPM technologies before and after neutron irradiation" (Talk) *International Workshop on Radiation Imaging Detectors*, Crete, Greece, July 2019

- **S. Kumar**, M. Herzkamp, S. van Waasen, "Non-linearity analysis of digital SiPM arrays response in a position sensitive neutron detector prototype ", (Poster) *IEEE Nuclear Science Symposium Medical Imaging Conference*, Manchester, UK, Nov. 2018

- M. Herzkamp, **S. Kumar**, S. van Waasen, "Development of a solid-state position sensitive neutron detector prototype based on 6Li - glass scintillator and digital SiPM arrays ", (Poster) *Symposium on Radiation Measurements and Applications*, Michigan, USA, June 2018

- D. Durini, **S. Kumar**, D. Arutinov, C. Degenhardt, S. van Waasen, "Assessment of photodetection performance of analog and digital SiPMs when exposed to cold neutrons", (Talk) *International Conference on the Advancement of Silicon Photomultipliers*, Schwetzingen, Germany, June 2018

- **S. Kumar**, D. Durini, C. Degenhardt, S. van Waasen,"Assessment of performance of silicon photomultipliers in scintillator based neutron detectors", (Poster) *International Workshop on Position Sensitive Neutron Detectors*, Jülich, Germany, May 2018

- **S. Kumar**, D. Durini, C. Degenhardt, S. van Waasen, "Photo detection characterization of SiPM technologies for their application in scintillator based neutron detectors", (Poster) *International Workshop on Radiation Imaging Detectors*, Krakow, Poland, May 2017

Theses:

- Davit Kordzaia, Characterization of Silicon Photomultipliers for detector developments, *Master thesis, Agricultural University of Georgia*, Principal advisors: Prof. Zaza Metrevel and Prof. Stefan van Waasen, Supervisor: **S. Kumar**, June 2020.

- Lokesh Niraula, Timing Resolution of Silicon Photomultipliers before and after irradiation with Cold Neutrons, *Master thesis, Politechnico Milano,* Principal advisors: Prof. Alberto Dalla Mora and Prof. Stefan van Waasen, Supervisor: **S. Kumar**, August 2019.

Appendix A

Reconstruction Algorithm Code

A.1 Look up Table, Center of Gravity and Least Square

```
import pdpc
import pdpc.from_root

try:
    import root_data
except ImportError:
    root_data = None

import plt

import numpy
import scipy.interpolate
import scipy.integrate
import scipy.optimize

import os
import cPickle as pickle

lut_length = numpy.max(pdpc.Die.pitch)
```

```
version = 3

class PhotonDistributionLUT:
    """
    Look-up-table for photon position distribution w.r.t.
    the corresponding neutron.
    """

    def __init__(self, series, selection=None, production_dir=None,
            length = 1.5*lut_length, nbins=300):
        """
        Obtain 1d look-up-table for photon distribution w.r.t the
        corresponding neutron position in a certain series with 2d
        value interpolation due to radial symmetry.
        @param series name of the series to be considered
        @param selection a root-like selection string for data
        @param production_dir the working directory, where the data
            was created
        @param length extent of underlying histogram in mm
        @param nbins number of bins of underlying histogram
        """

        # one dimensional photon histogram needs to span at least the
        # diagonal of the two dimensional expectation look up table
        # Therefore the default length and nbins is larger than for
        # e.g. PixelExpectationLUT

        self.rbins = plt.linbin(0., length, nbins)
        ph_count = 0
        number_of_events = 0
        ph_hist = numpy.zeros(nbins + 2)

        for photons, entry, npos in pdpc.from_root.get_raw_events(
```

```
                        series, selection, include_pde = False,
                          production_dir=production_dir):

            # Count how many photons hit the PDPC surface
            ph_count += len(photons)
            number_of_events += 1

            for time, y, z, energy in photons:
                # collect hits according to their distance from
                    the neutron event
                ph_hist[self.rbins(numpy.sqrt((y-npos[0])**2 +
                        (z-npos[1])**2))] += 1.

        self.timestamp = os.stat(os.path.join(series, "events.root")).st_mtime

        # divide each bin count by bin size, which is a circle shaped stripe
        # also divide by the total amount of photons for normalization
        self.ph_hist = ph_hist[1:-1] / numpy.array([ 2.*i + 1. for i in range
                (self.rbins.nbins) ])
                      / numpy.pi / self.rbins.binwidth**2 / sum(ph_hist)
        # interpolation is needed to provide more accurate values in between
        # bin boundaries
        self.ph_dist = scipy.interpolate.interp1d(self.rbins, self.ph_hist,
                      fill_value='extrapolate')
        self.number_incident_photons = float(ph_count) / number_of_events

    # direct call will return the interpolated value
    def __call__(self, x, y):
        """
        Although the underlying histogram is one dimensional,
        the lookup is based on the detector area, which is
        two dimensional. This is possible due to the radially
        symmetric nature of photon position distribution around
```

```
        the neutron position.
        """
        return self.ph_dist(numpy.sqrt(x**2 + y**2))


class PixelExpectationLUT:
    """
    Look-up-table for the expectation of ratio of photons
    hitting a PDPC pixel in case a neutron hits at a
    certain position relative to the pixel. This class
    uses a PhotonDistributionLUT at initialization, but
    doesn't store it beyond that. It simply creates its
    own two dimensional histogram with integral values.
    This enables the saving and loading of PixelExpectationLUT
    objects, which avoids long waiting times of the
    calculation of the histogram.
    """


    def __init__(self, series, selection=None, production_dir=None,
                 length=lut_length, nbins=200, cell_density=0):
        """
        Obtain 1d look-up-table for expected ratio of photons
        hitting a PDPC pixel in case a neutron hits at a certain
        position relative to the pixel.
        @param series name of the series to be considered
        @param selection a root-like selection string for data
        @param production_dir the working directory, where the data
            was created
        @param length extent of underlying histogram in mm
        @param nbins square root of number of bins of underlying histogram
        @param cell_density number of cells per square mm of the pixel.
        Don't take into account local saturation effects if cell_density is 0.
```

```
"""
self.series = series
self.selection = selection
self.production_dir = production_dir
self.length = length
self.nbins = nbins
self.cell_density = cell_density

ph_dist = PhotonDistributionLUT(series, selection, production_dir,
                                2*length, 2*nbins)
self.timestamp = ph_dist.timestamp
self.nph = ph_dist.number_incident_photons

self.bins = plt.linbin(0., length, nbins)

# determine the width of a single pixel in terms of number of bins
xpix_width = self.bins(pdpc.Pixel.size[0])
ypix_width = self.bins(pdpc.Pixel.size[1])

# Imagine the pixel centered on (0,0) for the first value. Then half
# of it is protruding into the negative direction in x and y directions
# Therefore, we need to integrate over
xbins = plt.linbin(-.5 * pdpc.Pixel.size[0], length +
                   .5 * pdpc.Pixel.size[0], nbins + xpix_width)
ybins = plt.linbin(-.5 * pdpc.Pixel.size[1], length +
                   .5 * pdpc.Pixel.size[1], nbins + ypix_width)

bin_area = xbins.binwidth * ybins.binwidth

# create temporary histogram of photon distribution values for easy
    mass integration
ph_dist_2d = self.nph * numpy.array([ [ ph_dist(x, y) *
                bin_area for y in ybins ] for x in xbins ])
```

```
        if cell_density > 0:
            ph_dist_2d *= 1. - numpy.exp(-ph_dist_2d / bin_area
                            / cell_density)

        self.expect_hist = numpy.zeros((nbins, nbins))

        self.expect_hist[0,0] = ph_dist_2d[:xpix_width,:ypix_width].sum()

        for i in range(nbins):
            if i > 0:
                # add sum in next line and subtract sum of first line,
                # thus movingcalong the integral area a tiny bit
                self.expect_hist[i,0] = self.expect_hist[i-1,0] -
                            ph_dist_2d[i-1,:ypix_width].sum() +
                            ph_dist_2d[i+xpix_width-1,:ypix_width].sum()

            for j in range(1,nbins):
                # use the same scheme as with horizontal movement of the
                    integral area.
                self.expect_hist[i,j] = self.expect_hist[i,j-1]
                 - ph_dist_2d[i:i+xpix_width,j-1].sum()
                 + ph_dist_2d[i:i+xpix_width,j+ypix_width-1].sum()

        self.expect_interp = scipy.interpolate.RectBivariateSpline
                            (self.bins, self.bins, self.expect_hist,
                                kx=1, ky=1)

    def __str__(self):
        return 'series = {}\nselection = {}\nproduction dir = {}\nlength
            = {}\nnbins={}'.format(self.series, self.selection,
                self.production_dir, self.length, self.nbins)
```

```
def __call__(self, x, y):
    return self.expect_interp.ev(numpy.abs(x), numpy.abs(y))

def save(self, filename):
    """
    Save the current histogram to a file
    """
    try:
        with open(filename, 'w') as target:
            pickle.dump((version, self), target)
    except IOError as e:
        print("pdpc.pos_reco.PixelExpectationLUT.save(): Cannot
            write to file'{}': {}".format(filename, e.message))

@staticmethod
def retrieve(filename):
    """
    load a PixelExpectationLUT from a file, if possible.
    """
    with open(filename, 'r') as source:
        this_version, lut = pickle.load(source)
        if this_version != version:
            raise DeprecationWarning('Version of lut found in file is old!
            Version found: {}. Current version: {}'.format(this_version,
                version))
        if lut is None:
            raise EOFError("No lut found in file {}".format(filename))
        return lut

@staticmethod
def retrieve_or_create(series, selection=None, production_dir=None,
        length=lut_length, nbins=200, cell_density=0, filename=None):
    """
```

```
Given a series, obtain the PixelExpectationLUT for that series
either by loading if possible, or creating it new and immediately
saving it. This function checks all parameters of an lut found in
a file, and if there is any deviation, creates a new one and
overwrites the file.
@param series name of the series to be considered
@param selection a root-like selection string for data
@param production_dir the working directory, where the data
    was created
@param length extent of underlying histogram in mm
@param nbins square root of number of bins of underlying histogram
@param cell_density number of cells per square mm of the pixel. Don't
    take into account local saturation effects if cell_density is 0.
@param filename name of the file to use. If None, defaults to
    'pixel_expecation.lut' in the corresponding series folder.
"""
if root_data is None:
    return PixelExpectationLUT.retrieve(filename)

if production_dir is None:
    production_dir = root_data._production_dir

if filename is None:
    suffix = '_'.join([ str(x).replace(' ', '-') for x in
        (length, nbins, cell_density) ])
    filename = os.path.join(production_dir, series,
                'pixel_expectation{}.lut'.format(suffix))
try:
    root_data._link_series(series, production_dir)
    if os.stat(filename).st_mtime < os.stat(os.path.join
                    (series, 'events.root')).st_mtime:
        print('pdpc.pos_reco.PixelExpectationLUT.
            retrieve_or_create(): file {} is outdated
```

```
                (there is new simulation data available)'.format
                (filename)) raise DeprecationWarning('file {}
                    is outdated'.format(filename))
        lut = PixelExpectationLUT.retrieve(filename)
        if series == lut.series and selection == lut.selection and
                            os.path.abspath(production_dir)
                    == os.path.abspath(lut.production_dir) and
                            length == lut.length and nbins
                    == lut.nbins and cell_density == lut.cell_density:
            print('pdpc.pos_reco.PixelExpectationLUT.retrieve_or_create()
                    : retrieved valid lut.')
        else:
            print('pdpc.pos_reco.PixelExpectationLUT.retrieve_or_create()
                    : retrieved lut doesn\'t
                  have matching attributes.')
            print('Required attributes: {}'.format((series, selection,
                    production_dir, length,
                    nbins, cell_density)))
            print('Found attributes: {}'.format((lut.series, lut.selection,
                lut.production_dir, lut.length, lut.nbins, lut.cell_density)))
            raise AssertionError('lut in file has different attributes.')
    except (OSError,IOError,DeprecationWarning,EOFError,AssertionError):
        print('pdpc.pos_reco.PhotonDistributionLUT.retrieve_or_create():
                Creating new lut.')
        lut = PixelExpectationLUT(series, selection, production_dir,
                length, nbins, cell_density)
        lut.save(filename)

    return lut


class Optimizer:
    def __init__(self, pixel_expectation_lut, expected_dark_counts_per_event=0,
```

```
            photon_detection_efficiency=0.29):
        self.detector = pdpc.Detector()
        self.lut = pixel_expectation_lut
        self.dcr = expected_dark_counts_per_event
        self.pde = photon_detection_efficiency

    def get_die(self, event):
        return self.detector.modules[event[4][5]-1].tiles[event[0]].dies[event[1]]

    def exp(self, m, die):
        return numpy.array([ self.lut(m[0] - p.position[0], m[1] -
                p.position[1]) * self.pde for p in die.pixels]) + self.dcr

    def dev(self, m, event):
        die = self.get_die(event)
        return ((self.exp(m, die) - event[3])**2 / self.exp(m, die)).sum()

    def first_guess(self, event):
        die = self.get_die(event)
        return sum( (2.*p.position - die.position) * c for p,c in
                        zip(die.pixels, event[3]) )
                    / sum(event[3])

    def optimize(self, event):
        return scipy.optimize.fmin(self.dev, self.first_guess(event),
                (event,), full_output=True, disp=False)

    def dev_multiple_events(self, m, event_list):
        """
        Return deviation of expected pixel count from measurement
        including mutliple events, grouped via coincidence
        @param m two dimentional position of the neutron event
        @param event_list list of event objects containing die number,
```

```
            photon counts etc. Format needs to be identical as the
            event objects returned by the module sipm.
        """

        return sum(self.dev(m, event) for event in event_list)

    def first_guess_multiple_events(self, event_list):
        """
        Obtain first guess for neutron position from event data.
        This can then be used to optimize the deviation function.
        Currently take the center of gravity as initial guess
        @param event information about die number, photon counts etc.
            Format needs to be identical as the event objects returned
            by the module sipm.
        @return two dimensional first guess for neutron position
        """
        return sum( self.first_guess(event) * sum(event[3])
                    for event in event_list )
                    / sum( c for event in event_list for c in event[3] )

    def optimize_multiple_events(self, event_list):
        """
        Find the best estimation for the neutron position using
        the deviation function defined in the dies.
        @param event_list list of event objects containing die number,
            photon counts etc. Format needs to be identical as the
            event objects returned by the module sipm.
        @return two dimensional best estimation for neutron position
        """
        return scipy.optimize.fmin(self.dev_multiple_events,
            self.first_guess_multiple_events(event_list), (event_list,),
                full_output=True)
```

```
class DieExpectation:
    """
    Wrapper class, using a single PixelExpectationLUT
    to obtain the expected pixel counts of a full die.
    """

    def __init__(self, pdpc_die, pixel_expectation_lut,
            expected_dark_counts_per_event, photon_detection_efficiency):
        """
        @param pdpc_die geometric information about the position of the die
            (should be a pdpc.Die object)
        @param pixel_expectation_lut the underlying PixelExpectationLUT object
        @param number_incident_photons The total expected number of photons
            incident on the SiPM surface after a single neutron event
        @param expected_dark_counts_per_event mean number of dark counts per
            neutron event.
        @param photon_detection_efficiency average photon detection efficiency
            of the detector.
        """
        self.die = pdpc_die
        self.pixexplut = pixel_expectation_lut
        self.expected_dark_counts_per_event = expected_dark_counts_per_event
        self.photon_detection_efficiency = photon_detection_efficiency

    def __call__(self, m):
        """
        Obtain expected number of photons in each of the four pixels
        in case of a neutron event at position m
        @param m two dimentional position of the neutron event
        """
        return numpy.array([ self.pixexplut(m[0] - p.position[0], m[1] -
                p.position[1])* self.photon_detection_efficiency for p
```

```
                in self.die.pixels]) + self.expected_dark_counts_per_event

    def dev(self, m, c):
        """
        Deviation of expectation from measurement
        @param m two dimentional position of the neutron event
        @param c list-like measured pixel counts in an event.
            length needs to be 4.
        """
        return ((self(m) - c)**2 / numpy.maximum(1., c)).sum()


class TileExpectation:
    """
    Wrapper class, using a single PixelExpectationLUT
    to obtain the expected pixel counts of pixels of
    any die. It also features the optimization of a
    deviation function in order to get the best
    estimation for the neutron position, given a
    measured event.
    """

    def __init__(self, pdpc_tile, pixel_expectation_lut,
                 expected_dark_counts_per_event=0.,
                 photon_detection_efficiency = 0.29):
        """
        @param pdpc_tile geometric information about the position of the
        tile (should be a pdpc.Tile object or subclasses thereof)
        @param pixel_expectation_lut the underlying PixelExpectationLUT
        object
        @param number_incident_photons The total expected number of photons
            incident on the SiPM surface after a single neutron event
        @param expected_dark_counts_per_event mean number of dark counts per
```

```
            neutron event.
        @param photon_detection_efficiency average photon detection efficiency
            of the detector.
        """
        self.tile = pdpc_tile
        self.pixexplut = pixel_expectation_lut
        self.expected_dark_counts_per_event = expected_dark_counts_per_event
        self.photon_detection_efficiency = photon_detection_efficiency

    def __call__(self, m, die_number):
        """
        Return expected pixel count of certain die in case a neutron
        hits
        @param m two dimentional position of the neutron event
        @param die_number number of die to check
        """
        return numpy.array([ self.pixexplut(m[0] - p.position[0], m[1]
                - p.position[1])* self.photon_detection_efficiency
                            for p in self.tile.dies[die_number].pixels ]) +
                                    self.expected_dark_counts_per_event

    def dev(self, m, event):
        """
        Return deviation of expected pixel count from measurement
        @param m two dimentional position of the neutron event
        @param event information about die number, photon counts etc.
            Format needs to be identical as the event objects returned
            by the module sipm.
        """

        return ((self(m,event[1]) - numpy.array(event[3]))**2 /
                self(m, event[1])).sum()
```

```
# first guess is the weighted mean of all pixel position
# with weight equal to number of hits in that pixel
def first_guess(self, event):
    """
    Obtain first guess for neutron position from event data.
    This can then be used to optimize the deviation function.
    Currently take the center of gravity as initial guess
    @param event information about die number, photon counts etc.
        Format needs to be identical as the event objects returned
        by the module sipm.
    @return two dimensional first guess for neutron position
    """
    return sum( (2.*p.position - self.tile.dies[event[1]].position) *
            c for p,c in zip(self.tile.dies[event[1]].pixels,
                            event[3]) ) / sum(event[3])

def optimize(self, event):
    """
    Find the best estimation for the neutron position using
    the deviation function defined in the dies.
    @param event information about die number, photon counts etc.
        Format needs to be identical as the event objects returned
        by the module sipm.
    @return two dimensional best estimation for neutron position
    """
    return scipy.optimize.fmin(self.dev, self.first_guess(event),
            (event,), full_output=True, disp=False)

def dev_multiple_events(self, m, event_list):
    """
    Return deviation of expected pixel count from measurement
    including mutliple events, grouped via coincidence
    @param m two dimentional position of the neutron event
```

```
        @param event_list list of event objects containing die number,
            photon counts etc. Format needs to be identical as the
            event objects returned by the module sipm.
        """

        return sum(self.dev(m, event) for event in event_list)

    def first_guess_multiple_events(self, event_list):
        """
        Obtain first guess for neutron position from event data.
        This can then be used to optimize the deviation function.
        Currently take the center of gravity as initial guess
        @param event information about die number, photon counts etc.
            Format needs to be identical as the event objects returned
            by the module sipm.
        @return two dimensional first guess for neutron position
        """
        return sum( self.first_guess(event) * sum(event[3])
                    for event in event_list )
                    / sum( c for event in event_list for c in event[3] )

    def optimize_multiple_events(self, event_list):
        """
        Find the best estimation for the neutron position using
        the deviation function defined in the dies.
        @param event_list list of event objects containing die number,
            photon counts etc. Format needs to be identical as the
            event objects returned by the module sipm.
        @return two dimensional best estimation for neutron position
        """
        return scipy.optimize.fmin(self.dev_multiple_events,
            self.first_guess_multiple_events(event_list),
               (event_list,), full_output=True)
```

A.2 Bayes Inversion

```
import numpy
import math

import pdpc

from pdpc.pos_reco import PixelExpectationLUT
from pdpc.pos_reco import TileExpectation
from scipy.stats import binom
from scipy import integrate
from numpy.random import rand

def integrate_grid(func, center_x,center_y):

 xlim = [center_x-4, center_x+4]
 ylim = [center_y-4, center_y+4]

 nbins=1000

 xbin= numpy.linspace(xlim[0],xlim[1],nbins)
 ybin= numpy.linspace(ylim[0],ylim[1],nbins)

 xbinwidth = xbin[1] - xbin[0]
 ybinwidth = ybin[1] - ybin[0]

 integral= sum( func(x, y) for x in xbin for y in ybin )

 return integral * xbinwidth * ybinwidth

def integrate_random(func, center_x, center_y):

 N = 1000000
```

```
 samples = rand(N, 2) * 8. + numpy.array([center_x, center_y])- 4.
 return sum(func(x, y) for x, y in samples) * 64. / N

def integrate(func, center_x, center_y):
 grid = integrate_grid(func, center_x, center_y)
 random = integrate_random(func, center_x, center_y)
 return (grid + random)/2.

class BayesReconstructor:

    def __init__(self,pelutfile,pde):

        self.pelut = PixelExpectationLUT.retrieve(pelutfile)
        self.tile = pdpc.Tile()
        self.texp = TileExpectation(self.tile, self.pelut,
                    photon_detection_efficiency=1.)
        self.pde = pde

    def reconstruct(self, event):

        # event structure = [tile, die, timestamp, pixels count,.. ]

        c = numpy.array(event[3])
        die_number = event[1]

        die = self.tile.dies[die_number]

        # Calculate center of gravity
        m = self.texp.first_guess(event)

        # Expected number of pixel count in specified die
        n = lambda m : self.texp(m, die_number)
```

```
#define binomial function P(c | x,y) binom.pmf (k, n, p) to
find probablity of number of counts for a neutron hit at m(x,y)

def binomp(x, y):

     return binom.pmf(c, n([x,y]), self.pde)

a = lambda x,y : numpy.prod(binomp(x,y))

# define normalization factor

#norm = integrate.dblquad(a, xlim[0], xlim[1], lambda y: ylim[0],
        lambda y: ylim[1])
norm=integrate_grid(a, m[0], m[1])

# define bayes inversion function P(x,y | c)

bayesinv = lambda x,y: a(x,y)/ norm

expfun_x = lambda x,y : bayesinv(x,y)* x
expfun_y = lambda x,y : bayesinv(x,y)* y

exppos_x=integrate_grid(expfun_x, m[0], m[1])
exppos_y=integrate_grid(expfun_y, m[0], m[1])

return numpy.array([exppos_x, exppos_y])
```

Band / Volume 221
High spatial resolution and three-dimensional measurement of charge density and electric field in nanoscale materials using off-axis electron holography
F. Zheng (2020), xix, 182 pp
ISBN: 978-3-95806-476-8

Band / Volume 222
Tools and Workflows for Data & Metadata Management of Complex Experiments
Building a Foundation for Reproducible & Collaborative Analysis in the Neurosciences
J. Sprenger (2020), X, 168 pp
ISBN: 978-3-95806-478-2

Band / Volume 223
Engineering of *Corynebacterium glutamicum* towards increased malonyl-CoA availability for polyketide synthesis
L. Milke (2020), IX, 117 pp
ISBN: 978-3-95806-480-5

Band / Volume 224
Morphology and electronic structure of graphene supported by metallic thin films
M. Jugovac (2020), xi, 151 pp
ISBN: 978-3-95806-498-0

Band / Volume 225
Single-Molecule Characterization of FRET-based Biosensors and Development of Two-Color Coincidence Detection
H. Höfig (2020), XVIII, 160 pp
ISBN: 978-3-95806-502-4

Band / Volume 226
Development of a transcriptional biosensor and reengineering of its ligand specificity using fluorescence-activated cell sorting
L. K. Flachbart (2020), VIII, 102 pp
ISBN: 978-3-95806-515-4

Band / Volume 227
Strain and Tool Development for the Production of Industrially Relevant Compounds with *Corynebacterium glutamicum*
M. Kortmann (2021), II, 138 pp
ISBN: 978-3-95806-522-2

Band / Volume 228
Complex magnetism of nanostructures on surfaces: from orbital magnetism to spin excitations
S. Brinker (2021), III, 208 pp
ISBN: 978-3-95806-525-3

Band / Volume 229
High-throughput All-Electron Density Functional Theory Simulations for a Data-driven Chemical Interpretation of X-ray Photoelectron Spectra
J. Bröder (2021), viii, 169, XL pp
ISBN: 978-3-95806-526-0

Band / Volume 230
Molecular tools for genome engineering of *Corynebacterium glutamicum*
C. K. Sonntag (2021), VIII, 111 pp
ISBN: 978-3-95806-532-1

Band / Volume 231
Interface Functionalization of Magnetic Oxide Fe_3O_4/$SrTiO_3$ Heterostructures
M. H. A. Hamed (2021), xvii, 151 pp
ISBN: 978-3-95806-535-2

Band / Volume 232
Optically induced magnetization reversal in Co/Pt multilayers
Role of domain wall dynamics
U. Parlak (2021), ix, 162, XII pp
ISBN: 978-3-95806-536-9

Band / Volume 233
Application of Silicon Photomultipliers in Neutron Detectors
S. Kumar (2021), xxvi, 157 pp
ISBN: 978-3-95806-537-6

Weitere ***Schriften des Verlags im Forschungszentrum Jülich*** unter
http://wwwzb1.fz-juelich.de/verlagextern1/index.asp

Schlüsseltechnologien / Key Technologies
Band / Volume 233
ISBN 978-3-95806-537-6

JÜLICH
Forschungszentrum